Title
Cryo-EM Structures and Biological Study of Pathogenic Alpha-Synuclein Fibrils

Author
Li, Binsen

Publication Date
2020

Peer reviewed|Thesis/dissertation

UNIVERSITY OF CALIFORNIA

Los Angeles

Cryo-EM Structures and Biological Study of Pathogenic Alpha-Synuclein Fibrils

A dissertation submitted in partial satisfaction of the

requirements for the degree Doctor of Philosophy

in Biochemistry, Molecular and Structural Biology

by

Binsen Li

2020

ABSTRACT OF THE DISSERTATION

Cryo-EM Structures and Biological Study of Pathogenic Alpha-Synuclein Fibrils

by

Binsen Li

Doctor of Philosophy in Biochemistry, Molecular and Structural Biology

University of California, Los Angeles, 2020

Professor David S. Eisenberg, Co-Chair

Professor Lin Jiang, Co-Chair

Multiple neurodegenerative diseases, including Parkinson's disease (PD), dementia with Lewy bodies (DLB), and multiple system atrophy (MSA) have been associated with the pathological aggregation of amyloid protein α-synuclein (αSyn). Similar to tau strains from different tauopathies, strains of αSyn have been demonstrated distinct cell-to-cell spreading. The distinct biological activity from each strain is encoded by the specific conserved conformation. However, we knew little about the atomic structures of αSyn fibril polymorphs. Our works revealed cryo-EM structures of αSyn wild-type fibril polymorphs and αSyn fibril polymorphs with hereditary mutation (E46K and H50Q). We showed two types of kernel that can be found in all αSyn polymorphs, which is validated by the fibrils from MSA patients. We also found αSyn fibril polymorphs are differed by varying 1) folding of protofilament 2) number of protofilament 3)

binding interface between protofilaments, thus leads to distinct cellular toxicity, aggregation rate and seeding capacity. Furthermore, we extracted and characterized fibrils from patients with Parkinson's disease, which formed a different polymorph. The study provides near-atomic insights about αSyn aggregation and enables future development of therapeutics.

The dissertation of Binsen Li is approved.

Jose A. Rodriguez

Joseph A. Loo

David S. Eisenberg, Committee Co-Chair

Lin Jiang, Committee Co-Chair

University of California, Los Angeles

2020

Dedicated to my parents and my girlfriend Yibing.

TABLE OF CONTENTS

LIST OF FIGURES

Chapter 1

Chapter 2 (Reprint)

Chapter 3 (Reprint)

Chapter 4 (Reprint)

Chapter 5

LIST OF TABLES

ACKNOWLEDGEMENTS

My mentor Professor Lin Jiang is the foremost person that made this dissertation possible. He provided encouragement, intellectual ideas, resources and endless patience at every moment I am in need. I want to thank my committee members: David Eisenberg, Joseph Loo and Jose Rodríguez for their invaluable inputs along the oral exam, mid-stream presentation, fourth-year meeting and the dissertation seminar. I collaborated and learned from members in David Eisenberg Group, Gal Bitan Group, Varghese John Group, Jose Rodríguez Group, David Teplow Group and Hong Zhou Group. I would like to acknowledge the staff scientists: Dan Anderson, Duilio Cascio, Ivo Atanasov, Alex Lisker and Michael Collazo and Electron Imaging Center for Nanomachines. I also appreciate people who participated in the structural group meeting for the critiques and discussion. This dissertation is truly a collective effort that comes from brilliant minds including but not limited to the list below:

In chapter 1, Peng Ge collected the cryo-EM data and calculated the maps. Kevin Murray and Michael Sawaya refined the models, simulated fiber diffraction and calculated the free energy. David Boyer assisted the data processing. Peng Ge, Shulin Ye, Kevin Murray and Michael Sawaya built the atomic models. Phorum Sheth and Meng Zhang optimized the fibril growth. Gayatri Nair and Woo Shik Shin helped with seeding and toxicity experiments. Kevin Murray, Peng Ge, David Eisenberg, Hong Zhou and Lin jiang involved in manuscript writing.

In chapter 2, Asa Hatami conducted the mouse experiments and analysis. Woo Shik Shin and Chuanqi Sun involved in the seeding and toxicity experiments. Kevin Murray and Michael Sawaya built the atomic models and simulated fiber diffraction. Chunni Zhu, Chris Elias and Mia Broad performed immunostaining. Lin Jiang and Varghese John supervised the research. Asa Hatami, Kevin Murray and Lin Jiang wrote the manuscript.

In chapter 3, Chuanqi Sun expressed and purified the protein, David Boyer collected and processed the cryo-EM data, and built the atomic models. Weijia Fan selected the filaments from micrographs. Michael Sawaya for writing the energy calculation software. David Boyer wrote the manuscript. Lin Jiang and David Eisenberg supervised the project.

In chapter 4, Chuanqi Sun purified the protein. David Boyer, Kang Zhou collected the cryo-EM data. Weijia Fan selected the filaments from micrographs. David Boyer, Michael Hughes and Michael Sawaya contributed to the data analysis. David Boyer, Lin Jiang and Daivd Eisenberg wrote the manuscript.

In chapter 5, Chao Peng (Lee Lab) performed fibril seeding and brain extraction. David Boyer and Kang Zhou collected and processed the data. Lin Jiang and David Eisenberg supervised the project.

VITA

2009-2013	B.A., Biological Sciences
	Connecticut College, New London, CT
2009-2013	Undergraduate Research Fellow, Zimmer Group
	Connecticut College, New London, CT
2013-2015	Research Assistant, Yellen Group, Neuroscience Dept
	Harvard Medical School, Boston, MA
2015-2020	Graduate Research Fellow, Jiang Group, Neurology Dept
	University of California, Los Angeles, CA
2015-2019	Teaching Assistant, Chemistry Dept
	University of California, Los Angeles, CA

2010	Keck Undergraduate Research Fund
2011	Ruth and William Silen, M.D. Award Winner, New England Science Symposium
2016	Venture Team Competition Winner, Business of Science Center, UCLA
2019	Dissertation Year Fellowship, UCLA

PUBLICATIONS

Boyer, D., **Li, B.**, Sun, C., Fan, W., Zhou, K., Hughes, M., Sawaya, M.R., Jiang, L and Eisenberg, D.S. (2020). The α-synuclein hereditary mutation E46K unlocks a more stable, pathogenic fibril structure. Proc Natl Acad Sci USA, 201917914.

Boyer, D., **Li, B.**, Sun, C., Fan, W., Sawaya, M.R., Jiang, L and Eisenberg, D.S. (2019). Structures of fibrils formed by α-synuclein hereditary disease mutant H50Q reveal new polymorphs. Nat Struct Mol Biol, 26, 1044-1052.

Shin, W.S., Di, J., Murray, K.A., Sun, C., **Li, B.**, Bitan, G and Jiang, L. (2019). Different Amyloid-β Self-Assemblies Have Distinct Effects on Intracellular Tau Aggregation. Front Mol Neurosci, 12, 268.

Shin, W.S., Di, J., Cao, Q., **Li, B.**, Seidler, P.M., Murray, K.A., Bitan, G. & Jiang, L. (2019). Amyloid β-protein oligomers promote the uptake of tau fibril seeds potentiating intracellular tau aggregation. Alzheimer's Res & Ther, 11, 86.

Díaz-García, C.M., Lahmann, C., **Li, B.**, Nathawani, N., Keller, J.P., Looger, L.L. & Yellen, G. (2019). Quantitative in vivo imaging of neuronal glucose concentrations with a genetically encoded fluorescence lifetime sensor. J Neurosci Res, 97, 946– 960.

Li,B., Ge, P., Murray, K.A., Sheth, P., Zhang, M., Nair, G., Sawaya, M.R., Shin, W.S., Boyer, D., Ye, S., Eisenberg, D.S., Zhou, Z.H. & Jiang, L. (2018). Cryo-EM of full-length α-synuclein reveal fibril polymorphs with a common structural kernel. Nat Commun, 9, 3609

Cao, Q., Shin, W.S., Chan, H., Vuong, C.K., Dubois, B., **Li, B.**, Murray, K.A., Sawaya, M.R., Feigon, J., Black, D.L., Eisenberg, D.S. & Jiang, L. (2018). Inhibiting amyloid-β cytotoxicity through its interaction with the cell surface receptor LilrB2 by structure-based design. Nat Chem, 10, 1213-1221.

Zimmer, MH., **Li, B.**, Shahid, RS., Peshkepija, P. and Zimmer, M. (2014). Structural Consequences of Chromophore Formation and Exploration of Conserved Lid Residues amongst Naturally Occurring Fluorescent Proteins. Chem Phys, 429, 5-10.

Li, B., (2013). Exploration of hinge residues among GFP-like proteins, Honors Papers, 14.

Li, B., Shahid, R., Peshkepija, P. and Zimmer, M. (2012). Water Diffusion in and out of the β-Barrel of Fast Maturing Fluorescent Proteins, Chem Phys, 392, 143-148

OVERVIEW

In 1912, Frederic Henry Lewey discovered Lewy bodies (LB) and Lewy neurites (LN) in substantia nigra of patients with Parkinson's disease (PD)[1]. Later, filamentous alpha-synuclein (αSyn) came into the spotlight as the major constituent of LB from patients with PD or dementia with Lewy bodies (DLB) by immunochemistry[2]. The etiology linkage between αSyn and Lewy body diseases was further strengthened by the disease causal hereditary mutations[3–9], duplication[10] and triplication[11] of SNCA, the gene encoded for αSyn.

The prion concept was introduced by Stanley Prusiner as proteinaceous infectious particles and linked to amyloid and neurodegenerative disease[12,13]. Since then, there has been accumulated evidence on how the αSyn aggregates spread from cell-to-cell in a prion-like manner. Braak et al. examined brains from PD patients with varied severity of symptoms and found the correlation between neuropathological damage and αSyn pathology along a predetermined sequence: from the lower brain stem spreading upwards to the neocortex[14,15]. Additionally, the grafted neurons placed into PD patients obtained LB over the years, indicating the αSyn pathology was transmitted from the neurons[16,17]. Another recent study on 47 multiple system atrophy (MSA) patients found out the glial cytoplasmic inclusions (GCIs) α-syn aggregation and the associated neuronal dysfunction spread in a different pattern[18]. This transmission was recapitulated in mouse: after injection of recombinantly expressed α-syn pre-formed fibrils into striatum, LB formed, spread across interconnected regions and reached substantia nigra pars compacta[19,20].

The prion-like strain properties have been characterized in tau and related neurodegenerative tauopathies, including Alzheimer's disease (AD), corticobasal degeneration (CBD), Chronic traumatic encephalopathy (CTE) and Pick's disease (PiD)[21]. Different tau strains,

derived from each tauopathy, can induce distinct endogenous tau propagation[22–24]. The strain-specific property is believed to come from the distinct structural conformation of tau aggregation, and this is not confirmed until recent publications of high-resolution cryo-electron microscopy structures. Structures of tau filaments extracted from AD[25], PiD[26], CTE[27] and CBD[28] are all distinct from each other, and the filaments are identical between cases in either CTE or CBD. Similarly, αSyn strains from LB and GCI exhibited distinct characteristics. Peng et al. demonstrated the GCI-αSyn is 1000 times more potent in seeding than LB-αSyn and the oligodendrocytes can transform a misfolded αSyn into the GCI-like strain[29]. Recently, LB and MSA strains after amplification were differentiated by a dye-binding assay with 95% sensitivity, which supports that αSyn derived from LB and MSA strains correspond to different conformations[30]

The structural study of αSyn is crucial for understanding the aggregation and template seeding. Various studies have been conducted using nuclear magnetic resonance (NMR), micro-electron diffraction (micro-ED) and cryo-electron microscopy (cryo-EM). Vilar et al. identified multiple β-strands within residues 35–96 forming the aggregation fibril core using quenched hydrogen/deuterium exchange NMR[31]. Non-amyloid-beta component (NAC) region covers residues 61-95 was responsible for fibril aggregation[32]. From the peptide structures solved by micro-electron diffraction, Jose et al. found out not only a segment within NAC region (NACore residues 68-78), but also another segment preceding NAC region (preNAC residues 47-56) is crucial forming steric zipper responsible for the aggregation[33]. The preNAC segment associates with most of the reported hereditary single-point mutations of synucleinopathies, such as E46K[5], H50Q[4], G51D[34], A53E[8], A53V[7] and A53T[35]. Around the same time, the first full-length αSyn PFF structure was solved by solid state NMR[36]. The structure reveals a hydrophobic core in a Greek-key motif formed by single protofilament assembly. Later, we used cryo-EM and discovered two

double-protofilament polymorphs using the same fibril core (Chapter 1)[37]. One of the polymorphs was confirmed by two other studies[38,39]. To link the structures with the disease, we found new polymorph structures of αSyn fibril due to hereditary mutation H50Q (Chapter 3)[40] and E46K (Chapter 4)[41]. Not until most recently, the cryo-EM structure of αSyn fibril from MSA was solved by Schweighauser et al[42]. The new double-protofilament polymorphs showed resemblance to the fibril core of PFF structure.

My doctoral work encompassed in this dissertation studies on the structures and biological activities of pathogenic αSyn fibrils:

Chapter 1 is reprinted from an article published in Nature Communications[37]. In the work, we presented near-atomic structures of two distinct full-length recombinant αSyn fibril polymorphs solved by cryo-EM. The fibrils are physiologically relevant due to its toxicity and seeding capacity in cells. Both two polymorphs contain a pair of β-sheet protofilaments sharing a conserved kernel consisting of a bent β-arch motif. Different packings of the same protofilaments at steric homo-zipper cores of the preNAC and NACore lead to distinct fibril polymorphs. We examined six hereditary mutations (E46K, H50Q, G51D, A53E, A53T, and A53V) located at the preNAC region and the initial analysis suggested potential contributions of different polymorphs in the complex pathogenesis of synucleinopathies.

Chapter 2 is a draft of a manuscript in submission. We presented an additional polymorph termed striated ribbon based on previous structural information. This new polymorph showed different cytotoxicity, seeding capacity in cells and distinct spreading patterns in mouse brain comparing with the previous polymorphs. The results indicate a necessary consideration of all

concurrent fibril polymorphs in development of therapeutics targeting neurodegenerative disease with high structural polymorphism.

Chapter 3 is a reprint of an article published in Nature Structural & Molecular Biology[40]. We determined two cryo-EM structures of αSyn fibrils containing hereditary mutation H50Q. Two new polymorphs, narrow and wide fibrils, are formed from one or two protofilament respectively. Impacted by the point mutation, previous known interfaces observed in wild-type structure are abolished. While the fold of the mutant structures resembles the fold of the wild-type structures, new structural elements are observed. The unique features of H50Q polymorphs help elucidate the faster aggregation, higher cytotoxicity and seeding capacity comparing with wild-type polymorphs.

Chapter 4 is a reprint of a published article that revealed the structure of αSyn fibrils carrying the hereditary E46K mutation[41]. The fibril structure contains a pair of protofilament that adopts a vastly rearranged, lower energy comparing to wild-type fibril structures. Based on energy prediction, this is due to the abolished E46-K80 salt bridge, which serves as a kinetic trap that prevents wild-type fibrils from folding into a more stable and pathogenic E46K fibril structure.

Chapter 5 includes the results from the structural study of αSyn fibrils extracted from PD patients. Unlike the fibrils from MSA, they formed predominantly the non-twisting ribbon polymorph, which poses a challenge for current cryo-EM structural determination.

1. Goedert, M., Spillantini, M. G., Del Tredici, K. & Braak, H. 100 years of Lewy pathology. *Nature Reviews Neurology* (2013). doi:10.1038/nrneurol.2012.242

2. Spillantini, M. G., Crowther, R. A., Jakes, R., Hasegawa, M. & Goedert, M. alpha-Synuclein in filamentous inclusions of Lewy bodies from Parkinson's disease and dementia with lewy bodies. *Proc. Natl. Acad. Sci.* **95**, 6469–73 (1998).

3. Narhi, L. *et al.* Both familial Parkinson's disease mutations accelerate alpha-synuclein aggregation. *J. Biol. Chem.* **274**, 9843–9846 (1999).

4. Appel-Cresswell, S. *et al.* Alpha-synuclein p.H50Q, a novel pathogenic mutation for Parkinson's disease. *Mov. Disord.* **28**, 811–813 (2013).

5. Zarranz, J. J. *et al.* The New Mutation, E46K, of α-Synuclein Causes Parkinson and Lewy Body Dementia. *Ann. Neurol.* **55**, 164–173 (2004).

6. Fares, M. B. *et al.* The novel Parkinson's disease linked mutation G51D attenuates in vitro aggregation and membrane binding of α-synuclein, and enhances its secretion and nuclear localization in cells. *Hum. Mol. Genet.* **23**, 4491–4509 (2014).

7. Yoshino, H. *et al.* Homozygous alpha-synuclein p.A53V in familial Parkinson's disease. *Neurobiol. Aging* **57**, 248.e7-248.e12 (2017).

8. Pasanen, P. *et al.* A novel α-synuclein mutation A53E associated with atypical multiple system atrophy and Parkinson's disease-type pathology. *Neurobiol. Aging* **35**, (2014).

9. Li, J., Uversky, V. N. & Fink, A. L. Effect of familial Parkinson's disease point mutations A30P and A53T on the structural properties, aggregation, and fibrillation of human α-synuclein. *Biochemistry* **40**, 11604–11613 (2001).

10. Chartier-Harlin, M. C. *et al.* α-synuclein locus duplication as a cause of familial Parkinson's disease. *Lancet* (2004). doi:10.1016/S0140-6736(04)17103-1

11. Singleton, A. B. *et al.* α-Synuclein Locus Triplication Causes Parkinson's Disease. *Science (80-.).* (2003). doi:10.1126/science.1090278

12. Prusiner, S. B. Novel proteinaceous infectious particles cause scrapie. *Science (80-.).* **216**, 136–144 (1982).

13. Prusiner, S. B. Some Speculations about Prions, Amyloid, and Alzheimer's Disease. *New England Journal of Medicine* **310**, 661–663 (1984).

14. Braak, H. *et al.* Staging of brain pathology related to sporadic Parkinson's disease. *Neurobiol. Aging* (2003). doi:10.1016/S0197-4580(02)00065-9

15. Braak, H. *et al.* Staging of the intracerebral inclusion body pathology associated with idiopathic Parkinson's disease (preclinical and clinical stages). *J. Neurol. Suppl.* (2002). doi:10.1007/s00415-002-1301-4

16. Li, J. Y. *et al.* Lewy bodies in grafted neurons in subjects with Parkinson's disease suggest host-to-graft disease propagation. *Nat. Med.* (2008). doi:10.1038/nm1746

17. Kordower, J. H., Chu, Y., Hauser, R. A., Freeman, T. B. & Olanow, C. W. Lewy body-like pathology in long-term embryonic nigral transplants in Parkinson's disease. *Nat. Med.* (2008). doi:10.1038/nm1747

18. Brettschneider, J. *et al.* Converging patterns of α-synuclein pathology in multiple system atrophy. *J. Neuropathol. Exp. Neurol.* (2018). doi:10.1093/jnen/nly080

19. Masuda-Suzukake, M. *et al.* Prion-like spreading of pathological α-synuclein in brain. *Brain* (2013). doi:10.1093/brain/awt037

20. Luk, K. C. *et al.* Pathological α-synuclein transmission initiates Parkinson-like neurodegeneration in nontransgenic mice. *Science (80-.).* **338**, 949–953 (2012).

21. Lee, V. M.-Y., Goedert, M. & Trojanowski, J. Q. Neurodegenerative Tauopathies. *Annu.*

Rev. Neurosci. (2001). doi:10.1146/annurev.neuro.24.1.1121

22. Sanders, D. W. *et al.* Distinct tau prion strains propagate in cells and mice and define different tauopathies. *Neuron* **82**, 1271–1288 (2014).

23. Gerson, J. E., Mudher, A. & Kayed, R. Potential mechanisms and implications for the formation of tau oligomeric strains. *Critical Reviews in Biochemistry and Molecular Biology* (2016). doi:10.1080/10409238.2016.1226251

24. Clavaguera, F. *et al.* Brain homogenates from human tauopathies induce tau inclusions in mouse brain. *Proc. Natl. Acad. Sci. U. S. A.* (2013). doi:10.1073/pnas.1301175110

25. Fitzpatrick, A. W. P. *et al.* Cryo-EM structures of tau filaments from Alzheimer's disease. *Nature* **547**, 185–190 (2017).

26. Falcon, B. *et al.* Structures of filaments from Pick's disease reveal a novel tau protein fold. *Nature* (2018). doi:10.1038/s41586-018-0454-y

27. Falcon, B. *et al.* Novel tau filament fold in chronic traumatic encephalopathy encloses hydrophobic molecules. *Nature* (2019). doi:10.1038/s41586-019-1026-5

28. Zhang, W. *et al.* Novel tau filament fold in corticobasal degeneration. *Nature* (2020). doi:10.1038/s41586-020-2043-0

29. Peng, C. *et al.* Cellular milieu imparts distinct pathological α-synuclein strains in α-synucleinopathies. *Nature* **557**, 558–563 (2018).

30. Shahnawaz, M. *et al.* Discriminating α-synuclein strains in Parkinson's disease and multiple system atrophy. *Nature* (2020). doi:10.1038/s41586-020-1984-7

31. Vilar, M. *et al.* The fold of alpha-synuclein fibrils. *Proc. Natl. Acad. Sci.* **105**, 8637–42 (2008).

32. Li, H. T., Du, H. N., Tang, L., Hu, J. & Hu, H. Y. Structural transformation and

aggregation of human α-synuclein in trifluoroethanol: Non-amyloid component sequence is essential and β-sheet formation is prerequisite to aggregation. *Biopolymers* (2002). doi:10.1002/bip.10179

33. Rodriguez, J. A. *et al.* Structure of the toxic core of α-synuclein from invisible crystals. *Nature* **525**, 486–490 (2015).

34. Lesage, S. *et al.* G51D α-synuclein mutation causes a novel Parkinsonian-pyramidal syndrome. *Ann. Neurol.* **73**, 459–471 (2013).

35. Lee, M. K. *et al.* Human α-synuclein-harboring familial Parkinson's disease-linked Ala-53 → Thr mutation causes neurodegenerative disease with α-synuclein aggregation in transgenic mice. *Proc. Natl. Acad. Sci.* **99**, 8968–8973 (2002).

36. Tuttle, M. D. *et al.* Solid-state NMR structure of a pathogenic fibril of full-length human α-synuclein. *Nat. Struct. Mol. Biol.* **23**, 409–415 (2016).

37. Li, B. *et al.* Cryo-EM of full-length α-synuclein reveals fibril polymorphs with a common structural kernel. *Nat. Commun.* **9**, 3609 (2018).

38. Guerrero-Ferreira, R. *et al.* Cryo-EM structure of alpha-synuclein fibrils. *Elife* **7**, (2018).

39. Li, Y. *et al.* Amyloid fibril structure of α-synuclein determined by cryo-electron microscopy. *Cell Res.* **28**, 897–903 (2018).

40. Boyer, D. R. *et al.* Structures of fibrils formed by α-synuclein hereditary disease mutant H50Q reveal new polymorphs. *Nat. Struct. Mol. Biol.* **26**, 1044–1052 (2019).

41. Boyer, D. R. *et al.* The α-synuclein hereditary mutation E46K unlocks a more stable, pathogenic fibril structure. *Proc. Natl. Acad. Sci. U. S. A.* (2020). doi:10.1073/pnas.1917914117

42. Schweighauser, M. *et al.* Structures of α-synuclein filaments from multiple system

atrophy . *bioRxiv* 2020.02.05.935619 (2020). doi:10.1101/2020.02.05.935619

43. Seuring, C. *et al.* Amyloid Fibril Polymorphism: Almost Identical on the Atomic Level, Mesoscopically Very Different. *J. Phys. Chem. B* (2017). doi:10.1021/acs.jpcb.6b10624

44. Guo, Q. *et al.* In Situ Structure of Neuronal C9orf72 Poly-GA Aggregates Reveals Proteasome Recruitment. *Cell* (2018). doi:10.1016/j.cell.2017.12.030

CHAPTER 1

nature COMMUNICATIONS

ARTICLE

DOI: 10.1038/s41467-018-05971-2 OPEN

Cryo-EM of full-length α-synuclein reveals fibril polymorphs with a common structural kernel

Binsen Li[1], Peng Ge[2], Kevin A. Murray[3], Phorum Sheth[1], Meng Zhang[3], Gayatri Nair[1], Michael R. Sawaya[3], Woo Shik Shin[1], David R. Boyer[3], Shulin Ye[2], David S. Eisenberg[3], Z. Hong Zhou[2,4] & Lin Jiang[1]

α-Synuclein (aSyn) fibrillar polymorphs have distinct in vitro and in vivo seeding activities, contributing differently to synucleinopathies. Despite numerous prior attempts, how polymorphic aSyn fibrils differ in atomic structure remains elusive. Here, we present fibril polymorphs from the full-length recombinant human aSyn and their seeding capacity and cytotoxicity in vitro. By cryo-electron microscopy helical reconstruction, we determine the structures of the two predominant species, a rod and a twister, both at 3.7 Å resolution. Our atomic models reveal that both polymorphs share a kernel structure of a bent β-arch, but differ in their inter-protofilament interfaces. Thus, different packing of the same kernel structure gives rise to distinct fibril polymorphs. Analyses of disease-related familial mutations suggest their potential contribution to the pathogenesis of synucleinopathies by altering population distribution of the fibril polymorphs. Drug design targeting amyloid fibrils in neurodegenerative diseases should consider the formation and distribution of concurrent fibril polymorphs.

[1] Department of Neurology, David Geffen School of Medicine, UCLA, Los Angeles, CA 90095, USA. [2] California Nano Systems Institute, UCLA, Los Angeles, CA 90095, USA. [3] Departments of Biological Chemistry and Chemistry and Biochemistry, Howard Hughes Medical Institute, UCLA-DOE Institute, UCLA, Los Angeles, CA 90095, USA. [4] Department of Microbiology, Immunology and Molecular Genetics, UCLA, Los Angeles, CA 90095, USA. These authors contributed equally: Binsen Li, Peng Ge, Kevin A. Murray. Correspondence and requests for materials should be addressed to D.S.E. (email: david@mbi.ucla.edu) or to Z.H.Z. (email: hong.zhou@ucla.edu) or to L.J. (email: jianglin@ucla.edu)

α-Synuclein (aSyn) is an intrinsically disordered protein, which can aggregate into different fibril forms, termed polymorphs. Polymorphic aSyn fibrils can recruit and convert native aSyn monomers into the fibril state, a process known as seeding[1]. Seeding of aSyn is associated with its pathological spread in the brain, contributing to multiple neurodegenerative diseases known as synucleinopathies, including Parkinson's disease (PD), dementia with Lewy bodies, and multiple system atrophy (MSA)[2,3].

Different aSyn fibril polymorphs have shown distinct seeding capacities in vitro and in vivo. Negative-stain electron microscopy (EM) images of aSyn fibrils extracted from PD and MSA patient brain tissues revealed fibril polymorphs with different widths: a major population of 10-nm-wide straight or twisted filaments and a minor population of 5-nm-wide straight filaments[2,3]. An additional EM study of recombinant aSyn fibrils confirmed the presence of similar fibril polymorphs, where each of the ~10-nm-wide filaments was composed of a bundle of two aSyn filaments[4]. More recently, two in vitro generated polymorphic fibrils (named ribbons and fibrils) exhibit different toxicity and in vitro[5] and in vivo[6] seeding properties. Peng et al.[7] demonstrated that brain-derived aSyn fibrils from different synucleinopathies are distinct in seeding potencies, which is consistent with the progression rate of each disease. In order to better understand the molecular basis for toxicity and seeding efficiency of aSyn aggregation in vitro and in vivo, atomic resolution structures of aSyn fibril polymorphs are crucially needed.

Previous studies have defined some structural details of aSyn fibrils. By micro-electron diffraction (microED)[8], structures of the preNAC region ($_{47}$GVVHGVTTVA$_{56}$) and NACore regions (non-amyloid-β component core, $_{68}$GAVVTGVTAVA$_{78}$), amyloidogenic segments critical for cytotoxicity and fibril formation, each revealed a pair of tightly mated in-register β-sheets forming a steric zipper. Moreover, a solid-state nuclear magnetic resonance (ssNMR) structure of recombinant aSyn revealed a Greek-key β-sheet motif in the hydrophobic core of a single fibril filament[9], where salt bridges (E46-K80), a glutamine ladder (Q79), and hydrophobic packing of aromatic residues (F94) contribute to the stability of the in-register β-sheet. These previous structural studies offer atomic insights into aSyn fibril architecture; however, additional structures are needed to elucidate the differences between aSyn fibril polymorphs. This information is necessary for the development of drugs targeting aSyn aggregation and seeding.

We set out to determine the structures of aSyn fibril species, and characterized one preparation of recombinant full-length aSyn containing various filamentous fibrils. The in vitro generated aSyn fibrils demonstrated a dose-dependent cytotoxicity and in vitro seeding in cells. Our cryo-EM study of the aSyn fibrils revealed two major polymorphs, termed rod and twister. Near-atomic structures (at a resolution of 3.7 Å) of both polymorphs showed a pair of β-sheet protofilaments sharing a conserved kernel consisting of a bent β-arch motif. However, the protofilaments of the structures contact with each other at different residue ranges, one at the NACore and the other at the preNAC region, forming different fibril cores. The involvement of NACore and preNAC steric zippers in the fibril cores of aSyn fibrils is supported by X-ray fiber diffraction experiments. In the rod and twister polymorphs, interface packing differences between the protofilaments lead to different fibril morphologies with distinct helical twists along the fibril axis. Structural analysis of disease-related mutations in the rod and twister structures suggests that aSyn fibril polymorphs may play different roles in aSyn aggregation and seeding.

Results

Seeding capacity and cytotoxicity of full-length human aSyn fibrils. In order to produce a wide range of aSyn fibril polymorphs, we screened fibril growth conditions of full-length recombinant human aSyn (1–140) by varying pH, salt, and additives. All samples were incubated in quiescent conditions for 14–30 days, in order to best mimic the physiological conditions of in vivo fibril growth. Fibril growth was monitored using thioflavin T (ThT) aggregation kinetics. We confirmed the presence of a wide range of fibril morphologies using negative-stain EM (see Methods and Supplementary Fig. 1). One fibril preparation stood out with well-separated single filaments with or without an apparent twist (Fig. 1a and Supplementary Fig. 2) in the presence of tetrabutylphosphonium bromide (an ionic liquid additive used in protein crystallization) at room temperature. Two major populations in this fibril preparation, the straight and twisted filaments, were around 10 nm wide (Fig. 1b), which is consistent with the previously reported aSyn fibrils either generated in vitro or extracted from patient brains[4,10].

We performed biological experiments to assess the pathological relevance of the aSyn fibrils preparation. In vitro seeding of the fibrils was monitored using a biosensor cell assay. Human embryonc kidney 293T (HEK293T) cells endogenously express disease-associated aSyn A53T mutant fused with cyan fluorescent protein (CFP) or yellow fluorescent protein (YFP) as a fluorescence resonance energy transfer (FRET) pair[11]. The aSyn fibril seeds were transduced into cells and induced intracellular aSyn aggregation or inclusions that was quantified by flow cytometry-based FRET analysis[11] (see Methods and Supplementary Fig. 3). At a concentration of aSyn fibril seeds as low as 10 nM, we observed aSyn inclusions as fluorescent puncta in cells (white arrows in Fig. 1c). The quantified FRET signal indicated the level of cellular aggregation seeded by the aSyn fibrils followed a dose-dependent manner (Fig. 1d). We also characterized the cytotoxicity of these aSyn fibrils in differentiated PC12 cells. The aSyn fibrils used in in vitro seeding experiment showed a significant cytotoxicity at 500 nM (Fig. 1e). Thus, the aSyn fibrils used in this study were able to act as seeds and trigger intracellular amyloid aggregation and subsequent cytotoxicity.

Cryo-EM structures of two aSyn fibril polymorphs. We performed cryo-EM studies to further elucidate the structures of fibril polymorphs. Two-dimensional (2D) classification of the cryo-EM images revealed that the fibril preparation consisted of two major populations, as well as several minor ones (Supplementary Fig. 4). The two major populations were composed of two fibril polymorphs, herein referred to as "twister," which has a twist in its projection views, and "rod," which lacks an apparent twist. We determined the three-dimensional (3D) structures for both polymorphs to a resolution of 3.7 Å (Table 1, Fig. 2, and Supplementary Figs. 5, 6). Both structures consisted of two intertwined protofilaments related by an approximate 2_1 screw axis of symmetry with a helical rise of 2.4 Å, which is consistent with the 2.4 Å reflection observed in the fiber diffraction patterns (Fig. 3e). The rod polymorph has a pitch of 920 Å and a right-handed helical twist of 179.5°; the twister polymorph has a shorter (460 Å) pitch and a right-handed helical twist of 179.1° (Fig. 2a).

We were able to build atomic models for both the rod and twister polymorphs, guided by side chain densities revealing distinct landmarks (Supplementary Figs. 7, 8). Both structures are composed of two protofilaments, each consisting of predominantly β-sheets. Out of the 140 amino acids in aSyn, 60 residues (L38-K97) are sufficiently ordered to be visible in the rod polymorph. As shown in the left panel of Fig. 2a, the polypeptide

chains stack into a Greek-key-like core with two turns, similar to the previous ssNMR-derived protofilament structure[9]. At both ends of the chain are lower-resolution densities that cannot be reliably modeled. In contrast, only 41 amino acids (K43-E83) are ordered in the twister polymorph, forming a bent β-arch (Fig. 2a, right panel). The more disordered chains at both termini project radially outward; they may account for the larger maximal width of the twister polymorph, as the ordered regions in both polymorphs have similar diameters.

Unique inter-protofilament interfaces of the two polymorphs. Comparison of the cryo-EM structures of the rod and twister polymorphs demonstrated the presence of a common protofilament kernel (root-mean-square deviation (RMSD) of residues H50-V77 = 2.2 Å for only Cα atoms, 2.5 Å for all atoms) (Fig. 3c, d). The twister polymorph has a well-ordered bent β-arch motif, while the rod polymorph also has a bent β-arch but uses additional ordered residues to form a Greek-key-like fold. A large fraction of branched amino acid residues (Thr, Val) is involved in the mainly hydrophobic core of the bent β-arch (Fig. 3a, b). Major turns or bends in the backbones of the two structures coincide with the presence of glycines (G67, G84), stabilizing hydrogen bonds (N65 and G68, Q79 and G86), and solvent exposed charged residues (E57, K58) (Fig. 3a, b). A hydrophilic channel, lined by residues T54, T59, E61, T72, and T75 (Supplementary Fig. 9), is adjacent to the hydrophobic core in the center of both structures. The bent β-arch conformation represents a common protofilament kernel between the rod and twister polymorphs. Interestingly, the single protofilament structure in the ssNMR study[9] shows some similarities to the common protofilament kernel in cryo-EM structures, with an Cα RMSD of 3.4 Å (rod)

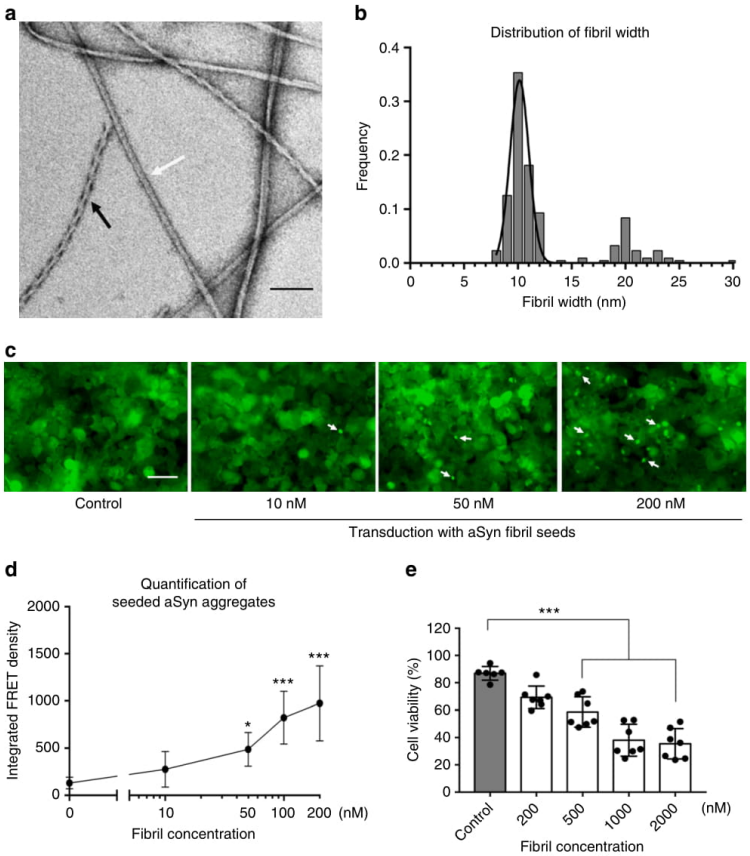

Fig. 1 aSyn fibrils with distinct polymorphs have in vitro seeding and toxicity in cells. **a**, **b** Negative-stain EM (**a**) of full-length aSyn fibrils showing two distinct polymorphs—rod (non-twisted filaments, white arrow) and twister (twisted filaments, black arrow)—and a fibril width around 10 nm (**b**). **c**, **d** Direct visualization (**c**) and FRET-based quantification (**d**) of seeded intracellular aSyn aggregates. Fluorescent images obtained using the FITC channel (ex. 488 nm, em. 525 nm) showed aSyn aggregates as indicated by bright fluorescent puncta (white arrows in **c**). The diffuse background fluorescence came from endogenously expressed soluble, non-aggregated YFP-aSyn in the cells. Transduction of sonicated aSyn fibril seeds into the cells induced intracellular aSyn aggregation, which was also quantified using FRET analysis (**d** and Supplementary Fig. 3). **e** Cytotoxicity of aSyn fibrils evaluated by MTT-based cell viability assay of differentiated PC12, neuron-like cells. The aSyn fibrils used in the seeding experiment (**c**, **d**) have significant cytotoxicity ($p < 0.0001$) at 500 nM. Data are presented as mean ± standard error. Results are from multiple independent biological experiments with $n = 3$–5 per experiment. $^*p \le 0.01$, $^{***}p \le 0.0001$ vs. control (buffer used to produce the aSyn fibrils). Scale bar: (a) 100 nm (c) 50 μm

Table 1 Cryo-EM data collection, refinement, and validation statistics

	Rod polymorph EMD-7618 PDB:6CU7	Twister polymorph EMD-7619 PDB:6CU8
Data collection		
Magnification	×130,000	×130,000
Defocus range (μm)	1.5–4	1.5–4
Voltage (kV)	300	300
Microscope	Titan Krios	Titan Krios
Camera	Gatan K2 Summit (GIF)	Gatan K2 Summit (GIF)
Frame exposure time (s)	0.2	0.2
No. of movie frames	50	50
Total electron dose (e^{-}/Å^{-2})	80	80
Pixel size (Å)	1.07	1.07
Reconstruction		
Box size (pixel)	432	432
Inter-box distance (Å)	36	36
No. of segments extracted	182,253	182,253
No. of segments after Class2D	23,830	61,698
No. of segments after Class3D	N/A[a]	34,091
Resolution	3.7	3.7
Map sharpening *B*-factor (Å^2)	100	100
Helical rise (Å)	2.40	2.40
Helical twist (°)	179.53	179.06
Atomic model		
No. of protein residues	60	41
Ramachandran plot values		
Most favored (%)	87.9	97.4
Allowed (%)	10.3	2.6
Disallowed (%)	1.72	0.0
Rotamer outliers	0.0	0.0
RMS deviations		
Bond lengths (Å)	0.01	0.01
Bond angles (°)	0.89	0.87
Clashscore	25.67	22.39
Map CC (whole unit cell)	0.356	0.375
Map CC (around atoms)	0.754	0.727

N/A not applicable
Particles from Class2D are used in the refinement

and 3.4 Å (twister), respectively, for the 28 matched residues (Supplementary Fig. 10).

While a pair of identical protofilaments is intertwined in both structures, different steric zipper interfaces are present between the protofilaments. The highly complementary inter-protofilament interface in the rod polymorph, with a calculated shape complementary score[12] of 0.77, consists of a steric homo-zipper of the preNAC ($_{47}$GVVHGVTTVA$_{56}$) (Fig. 3c). The preNAC steric zipper in the rod structure is associated with six PD familial mutation sites (E46K, H50Q, G51D, A53E, A53T, and A53V; Fig. 4a)[13–18], with the potential to disrupt the preNAC zipper of fibril core in the rod structure (Fig. 3f). Based on the structural analysis (Supplementary Figs. 11 and 12), the mutation H50Q would interfere with the potential salt bridge E57-H50. The negative charge in the mutation G51D and A53E would likely disrupt the steric zipper interaction between the two protofilaments, while A53T and A53V would weaken the hydrophobic packing of the zipper.

In the twister structure, the interface between the two protofilaments (SC = 0.71) is a steric homo-zipper of the NACore ($_{68}$GAVVTGVTAVA$_{78}$) (Fig. 4c). The β-strands of the NACore interdigitate with each other and form the hydrophobic core, consisting of small apolar residues (A69, V71, V74). In the structure, the preNAC residues are located at the peripheral region away from the fibril core. Therefore, the six familial mutations of the preNAC region which potentially disrupt the rod structure may have little effect on the stability of the twister structure (Fig. 3g and Supplementary Fig. 11). We find generally good agreement between our energy calculations and the hypothesized effects each familial mutation may have on each polymorphic structure (Supplementary Fig. 12). An exception to this agreement is the H50Q mutation, where the prediction method fails to capture the complex H-bond networks of multiple residues H50, E47, and K45.

Relevance of full-length aSyn fibrils with peptide zippers. X-ray fiber powder diffraction of the full-length aSyn fibril polymorphs revealed cross-β fibril structures consistent with those of NACore and preNAC peptide fibrils (Fig. 3e). All fibril diffraction patterns contain a strong 4.7 Å reflection, characteristic of the stacking of β-strands along the fiber axis, and reflections near 8.0 and 11.5 Å, likely stemming from the staggering between adjacent β-sheets in the structure, either within a protofilament or between two protofilaments. All fibrils also have the reflection at 2.4 Å in their diffraction patterns. Observed in both cryo-EM structures, a helical rise of 2.4 Å, half the 4.8 Å spacing between β-strands, permits the two sheets to interdigitate tightly together. Similar 2.4 Å helical rises are observed in the microED structures of preNAC and NACore peptide fibrils[8]. This 2.4 Å reflection confirmed that the structures of aSyn fibrils and the peptide fibrils are all defined by an approximate 2_1 screw axis of symmetry. The resemblance of all of these fibril diffraction patterns suggested that the aSyn fibrils may share a fibril core in which NACore and preNAC are involved.

In the aSyn fibril preparation, the protofilaments in both the rod and twister structures share a conserved fibril kernel and contact with adjacent protofilaments at either preNAC or NACore regions. The rod polymorph has a longer pitch, while the twister polymorph has a pitch shorter by half. Distinct fibril morphologies indicated by fibril pitch thus arise from differences in packing, which are revealed in our near-atomic structures. Structural analysis of familial mutations in the rod and twister structures suggests that aSyn fibril polymorphs may play different roles in aSyn fibril formation in synucleinopathies.

Discussion

Protofilaments in aSyn fibrils are composed of single chains arranged in parallel in-register β-sheets. Fibril protofilaments can assemble in different arrangements to form several possible polymorphic structures. α-Synuclein fibrils isolated from PD patient brains have been shown to have polymorphic structures, with fibril widths of ~5 and ~10 nm[10]. Our cryo-EM structures of two polymorphs, each with a pair of protofilaments, are ~10 nm in width (99 Å for the rod structure and 96 Å for the twister structures, Fig. 2a). The single protofilament structure revealed in the ssNMR study was ~5 nm in width[9] and resembles the common protofilament kernel in cryo-EM structures of both rod and twister polymorphs, with an RMSD of 3.5 and 3.8 Å, respectively for the 38 matched residues (Supplementary Fig. 9). The recently published cryo-EM structure of a truncated aSyn (residues 1–121) fibril[19] has a structure similar to the rod polymorph of the full-length protein reported here (with an RMSD of 2.1 Å). Thus, different aSyn fibril polymorphs could arise from alternative arrangements of the same protofilament kernel. Similar phenomena have been observed in other amyloid proteins, including tau and β-amyloid, where different packing arrangements of the same protofilament kernel lead to polymorphic structures[20,21]. These observations suggest a generic mode of fibril architecture by the concurrent assembly of identical protofilaments (Fig. 4b).

Our structural studies reveal that the rod and the twister protofilaments assemble symmetrically about a homo-zipper of the preNAC segment or of the NACore segment, respectively.

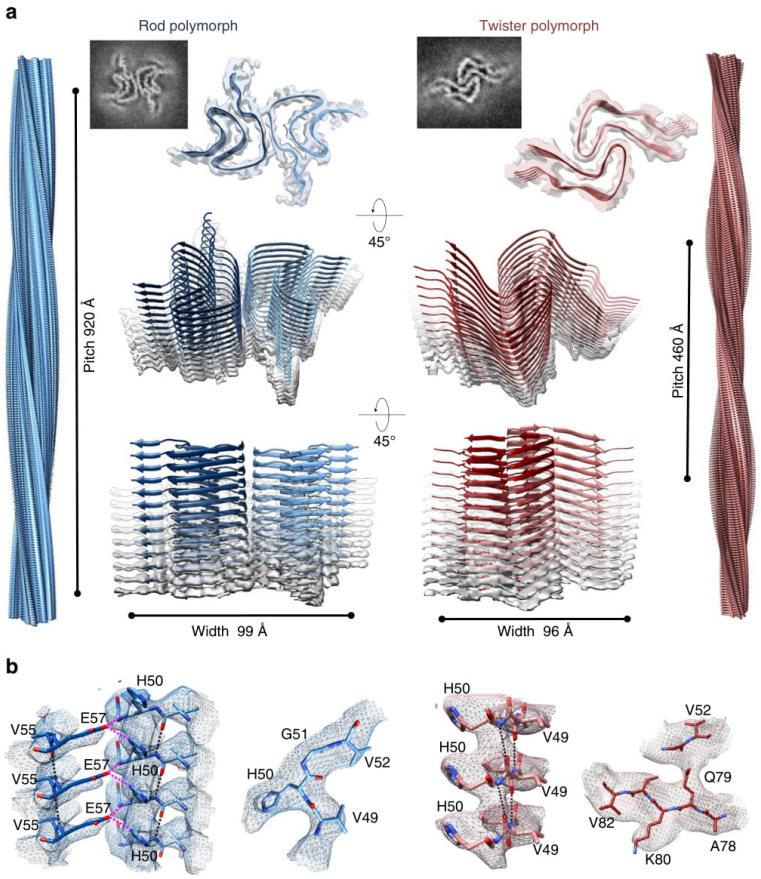

Fig. 2 Cryo-EM structures and atomic models of the aSyn rod and twister polymorphs. **a** The cryo-EM structures of the rod (left) and twister (right) polymorphs of the full-length aSyn fibrils shown as density slices (top inlet), as semitransparent surfaces overlaid with their atomic models viewed from two different angles (lower panels). The rod (blue) and twister (red) polymorphs contain two protofilaments composed of stacked β-sheets and packed by an approximate 2_1 screw axis of symmetry. Shown on the left and right sides are the 3D model of the rod and twister fibril polymorphs, respectively, with their distinctively different helical pitches depicted. **b** Model validation. Representative regions of density maps of both polymorphs are superimposed with their models showing match of side chain with cryo-EM densities. Intra-protofilament hydrogen bonds are shown in black dashed lines, and inter-protofilament hydrogen bonds are shown in magenta dashed lines. See details in Supplementary Figures 7 and 8

Since the twister and rod fibrils have structurally conserved kernels but contact at either the preNAC or NACore segments, the fibril polymorph is determined by the location of the protofilament packing interface instead of the kernel structures. The two structures of aSyn polymorphs revealed the steric homo-zipper core of the preNAC and NACore between the protofilaments. Together with the crucial contribution of the preNAC and NACore segments to the formation of aSyn fibrils, our structures present these unique protofilament interfaces as therapeutic targets to halt the fibrillization of aSyn. Atomic details of the preNAC and NACore zippers from our aSyn polymorphic structures provide insights in the structural-based designs of aSyn aggregation inhibitors in synucleinopathies.

Different aSyn fibril preparations, whether obtained from brain tissue or produced in vitro, may have different compositions of polymorphs. Each polymorph is distinguished by packing differences between protofilament kernels and makes distinct contributions to the biological activities of seeding and toxicity. The aSyn fibril preparation containing fibril polymorphs with different compositions thus could have discrete seeding efficiency and cytotoxicity profiles. Therefore, it is essential to characterize the biological function of each individual polymorph in order to understand the pathological role of the complex polymorphic fibrils.

The cryo-EM structure of the rod polymorph constructed around the fibril core of the preNAC region, and five PD familial mutations (E46K, H50Q, G51D, A53E, A53T, and A53V) are located at and associated to the preNAC region (Fig. 4a). Our structural analysis suggests that all these mutations would disfavor the fibril core of the rod structure without affecting the twister structure constructed around a different fibril core. Therefore, those point mutations would result in a different composition of polymorphic aSyn fibrils, by decreasing or eliminating the population of the rod polymorph while potentially

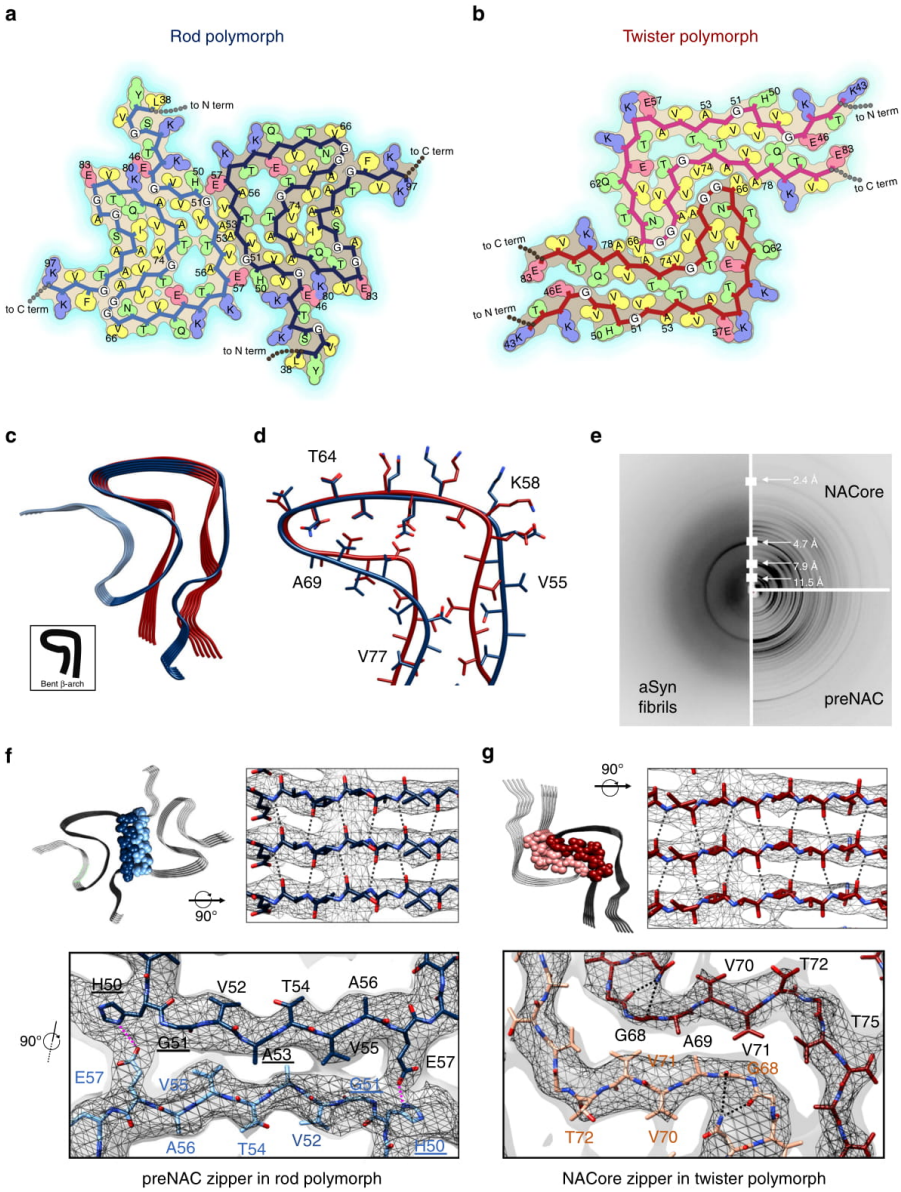

Fig. 3 Distinct zipper interfaces between protofilament kernels in the two aSyn polymorphs. **a**, **b** Residue interactions of two asymmetric units in two opposing protofilaments elucidate packing between and within these two protofilaments in the rod (**a**) and twister (**b**) polymorphs (viewed down fibril axis). Residues are colored by hydrophobicity (yellow: hydrophobic; green: polar; red: negative charge; blue: positive charge). **c**, **d** An overlay of protofilaments of the rod (blue) and twister (red) polymorphs reveals a conserved kernel of a bent β-arch. **e** Diffraction patterns of the full-length aSyn fibrils agree with those of NACore and preNAC peptide fibrils. **f**, **g** The two protofilaments in the rod (**f**) and twister (**g**) polymorphs contact by different residues (space-filled) and have distinct fibril core of tightly packed steric zippers of preNAC (blue) and NACore (red), as previously observed in those peptide fibril structures. PD familial mutation residues are labeled with underlines. The cryo-EM density maps are shown as gray mesh surfaces. Intra-protofilament hydrogen bonds are shown in black dashed lines, and inter-protofilament hydrogen bonds are in magenta

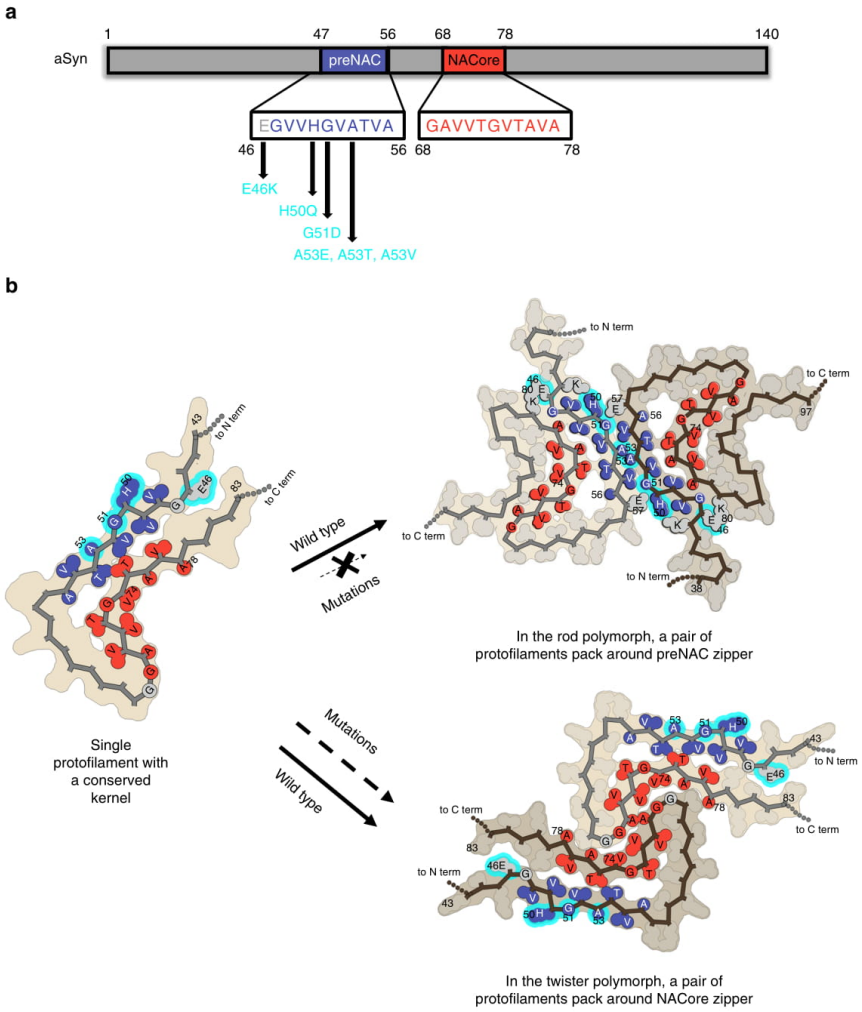

Fig. 4 Morphogenesis of aSyn fibril polymorphs arising from inter-protofilament packing. **a** Primary sequence of preNAC (blue) and NACore (red) critical for the aggregation of aSyn 1–140 and six PD familial mutations (cyan) located near the preNAC region. **b** Protofilaments sharing a kernel structure of a bent β-arch assemble into the rod and twister fibril polymorphs by packing at preNAC and NACore zipper interfaces, respectively. The PD familial mutations (cyan) likely disfavor the rod structure over the twister structures, and alter the polymorphic composition of aSyn fibrils

inducing the formation of another fibril polymorph (Fig. 4b). The resulting changes in the ensembles of fibril polymorphs may alter their biological activity and underlie the phenotypic differences in patients with PD due to familial point mutations, suggesting aSyn fibril polymorphs have pathogenic contributions to synucleinopathies.

In summary, we have determined the cryo-EM structures of two fibril polymorphs of full-length recombinant aSyn with distinct protofilament interfaces. The rod and twister polymorphs are composed of protofilaments with highly conserved kernel structure assembled around different steric zipper interfaces, giving rise to polymorphism in aSyn fibrils. The two structures of fibril polymorphs elucidate atomic interactions of the steric zippers within the fibril cores, potentially guiding the future drug design of aSyn aggregation inhibitors. These structural and functional studies thus establish the need to consider the contributions of all polymorphs and their relevance to overall pathogenesis when performing future rational design of therapeutic agents based on fibril structures.

Methods

Expression and purification of recombinant aSyn (1–140). Full-length aSyn protein was expressed in *Escherichia coli* (BL21-DE3 Gold strain, Agilent Technologies, Santa Clara, CA, USA) and purified according to a published protocol[8]. The bacterial induction started at an OD_{600} of ~0.6 with 1 mM isopropyl β-D-1-thiogalactopyranoside for 6 h at 30 °C. The harvested bacteria were lysed with a probe sonicator for 10 min in an iced water bath. After centrifugation, the soluble fraction was heated in boiling water for 10 min and then titrated with HCl to pH 4.5 to remove the unwanted precipitants. After adjusting to neutral pH, the protein

was dialyzed overnight against Q Column loading buffer (20 mM Tris-HCl, pH 8.0). The next day, the protein was loaded onto a HiPrep Q 16/10 column and eluted using elution buffer (20 mM Tris-HCl, 1 M NaCl, pH 8.0). The eluent was concentrated using Amicon Ultra-15 centrifugal filters (Millipore Sigma) to ~5 mL. The concentrated sample was further purified with size-exclusion chromatography through a HiPrep Sephacryl S-75 HR column in 20 mM Tris, pH 8.0. The purified protein was dialyzed against water, concentrated to 3 mg/mL, and stored at 4°C. The concentration of the protein was determined using the Pierce™ BCA Protein Assay Kit (cat. no. 23225, Thermo Fisher Scientific).

Fibril preparation monitored using ThT assay. The fibril growth conditions were screened in the 96-well plate format in various pH, salts, and additives. Specifically, purified aSyn (100, 200, or 300 μM) was diluted in phosphate-buffered saline (PBS), 50 mM Tris buffer, or 5 mM Tris buffer at various pH (5.5, 6.5, 7.5, or 8.5) in the presence or absence of 24 commercially available crystal screening additives in the Ionic Liquid Screen (Hampton Research, Aliso Viejo, CA, USA). The samples were adequately mixed with 20 μM ThT and added into each well. The 96-well plates were incubated at either room temperature or 37 °C for 14–30 days. The ThT signal was monitored using the FLUOstar Omega Microplate Reader (BMG Labtech, Cary, NC, USA) at an excitation wavelength of 440 nm and an emission wavelength of 490 nm. Selected fibrils conditions from the ThT assay were used to grow the fibrils in the absence of ThT to be further characterized in the negative-stain EM. Out of hundreds of fibril growth conditions screened, one fibril growth condition (300 μM aSyn, 15 mM tetrabutylphosphonium bromide, room temperature) was selected for the rest of our study.

Transmission electron microscopy. The fibril sample (3 μL) was spotted onto a freshly glow-discharged carbon-coated electron microscopy grid. After 1 min, 6 μL uranyl acetate (2% in aqueous solution) was applied to the grid for 2 min. The excessive stain was removed by a filter paper. The samples were imaged using an FEI T12 electron microscope.

Cryo-EM reconstruction and atomic modeling. A 2.5-μL aliquot of the narrow fibrils sample was applied to each "baked" Quantifoil 1.2/1.3 μm, 200 mesh grid. The grid was then blotted and plunged into liquid nitrogen-cooled liquid ethane in a Vitrobot Mark IV (FEI, Hillsboro, OR, USA) machine[22]. Cryo-EM data were acquired in a Titan Krios microscope (FEI, operated at 300 kV high tension and ×130,000 nominal magnification) equipped with a Quantum LS Imaging System (Gatan, Pleasanton, CA, USA; energy filter slit width was set at 20 eV and K2 camera at counting mode; calibrated pixel size is 1.07 Å). The microscope was aligned as previously described[23]. Data collection was automated by Leginon software package[24]. The defocus value target was set to a single value of 2.7 μm. Dose-fractionation movies were recorded at a frame rate of 5 Hz for a total duration of 10 s. The dosage rate was targeted at 6 electrons (e)/(Å^2 s), as initially measured by Digital Micrograph (Gatan) software, though fluctuations (within ±10%) in dosage potentially due to electron source instability were subsequently noticed during the imaging session of about 2 days.

Frames in each movie were aligned and summed to generate a micrograph as previously described[25]. Micrographs generated by summing all frames were used to determine defocus values and particle locations by CTFFIND4 (ref.[26]) and manual picking, respectively. We used the micrographs generated by summing the 3rd (5 e/Å^2) through the 20th frames (accumulated dose 30 e/Å^2) for data processing. Micrographs with severe astigmatism (>9%), obvious drift, or measured underfocus values outside the allowed range (1.5–4 μm) were discarded.

We manually picked filaments indiscriminately in EMAN[27] helixboxer (see statistics in Table 1). The 2D classification revealed two major populations (rod and twister polymorphs) and several minor populations. The other minor populations were too poorly defined to be further characterized, and thus omitted in the analysis. Of the classes suitable for analysis, the relative percentages of the rod and twister polymorphs are ~30 and ~70%, respectively. The number is calculated from the accepted classes using Class2D.

We performed 2D and 3D classifications in GPU-accelerated Relion 2.0 (ref.[28]) to separate the particles belonging to the rod and twister polymorphs into subsets as reported previously[25]. We also performed 2D classification of segments extracted with a very large (1024 pixels) box size to determine the pitches of the two polymorphs. Helical parameters were deduced from these pitches with the assumption that each helix had a twisted twofold screw axis. The initial models for the 3D classifications and reconstructions were generated by running Class3D with 1 class, an elongated Gaussian blob as the starting reference, and a fixed helicity based on the above-mentioned assumption. Specifically, the rod class was separated with solely Class2D, and the twister class was separated with Class2D followed by Class3D similar to previously described[25].

We further refined the 3D reconstructions of the rod and twister filaments using Class3D in Relion as previously described[25], except that we now used version 2.0 of Relion with built-in real-space helical reconstruction. Briefly, we started a run of Class3D with one class, with low initial *T* factor (i.e., "--tau-fudge") and larger (7.5°) angular interval. We gradually increased the *T* factor and reduced the angular interval with close manual monitoring. We eventually reached a *T* factor of 256 and an angular interval of 0.975° (healpix order 6) for the final map.

We tested the resolutions of the two resulting maps as previously reported[25]. Two types of Fourier shell correlation (FSC) was calculated: one between the map and atomic model and the other between the 3D reconstructions from two-half datasets (Supplementary Fig. 5). The former, map-model FSC evaluation indicates that the resolutions for both the rod and twister maps are 3.7 Å based on the FSC = 0.5 criterion[29]. For the latter, we divided the helical particles by even and odd micrographs (to prevent particles from the same fiber contributing to two different reconstructions), and then calculated a 3D reconstruction from each half dataset using the fully refined center and orientations parameters and performed the FSC calculation. (This FSC is thus not gold standard, as the dataset was not divided in the beginning and was refined in its totality.) Therefore, we used the FSC = 0.5 criterion[28] to evaluate the resolution. We did not apply any density-based or model-based mask for the FSC tests, but a spherical mask of a 170-pixel diameter and 10-pixel apodization, after clipping the density map into 192 × 192 × 192 box. This evaluation indicates that the resolutions for the rod and twister maps are 3.5 and 3.6 Å at FSC = 0.5, respectively.

We built atomic models for the two maps and refined them in central nervous system[30,31] and Phenix *phenix*.real_space_refine[32] with the final Relion refined helical parameters as NCS restraints, as previously described[25]. The statistics are summarized in Table 1.

Structural analysis and energy calculations. Based on the two cryo-EM structures of aSyn fibrils, energies for the wild-type and familial mutants were calculated with Rosetta[33]. During the energy evaluation, we omitted the contributions from the statistical terms in the Rosetta scoring function which are derived from monomeric proteins. The total score of each structure was calculated by the sum of the physically meaningful energy components (Lennard–Jones interactions, solvation, hydrogen bonding, and electrostatics). Using either rod or twister structure, the contribution of each mutant was evaluated by the score difference between the mutant and the WT.

Fiber diffraction. The procedure followed the protocol described by Rodriguez et al.[8]. To replace the solvent with water, the fibril sample (50 μL) were pelleted by centrifugation at 8000 × *g* for 5 min and washed with deionized H_2O for three times. The fibrils were resuspended in 10 μL of H_2O, placed between two capillary glass rods, and allowed to air dry. The next day, the glass rods with fibrils aligned in between were mounted on a brass pin for x-ray diffraction. Each pattern was collected using 1.54 Å x-rays produced by a Rigaku FRE + rotating anode generator equipped with an HTC imaging plate at a distance of 150 mm for 5° rotation width. The results were analyzed using the Adxv software[34].

Cellular toxicity assay. The protocol was adapted from the Provost and Wallert laboratories[35]. Thiazolyl blue tetrazolium bromide for the 3-(4,5-dimethylthiazol-2-yl)-2,5-diphenyltetrazolium bromide (MTT) cell toxicity assay was purchased from Millipore Sigma (M2128-1G; Burlington, MA, USA). PC12 cells were plated in 96-well plates at 10,000 cells per well in Dulbecco's modification of Eagle's medium (DMEM), 5% fetal bovine serum (FBS), 5% heat-inactivated horse serum, 1% penicillin/streptomycin, and 150 ng/mL nerve growth factor 2.5S (Thermo Fisher Scientific). The cells were incubated for 2 days in an incubator with 5% CO_2 at 37 °C. The cells were treated with different concentrations of aSyn fibrils (200, 500,1000, 2000 nM). The aSyn fibrils were sonicated in a water bath sonicator for 10 min before being added to the cells, the same as the fibrils tested in the in vitro seeding experiment. After 18 h of incubation, 20 μL of 5 mg/mL MTT was added to every well and the plate was returned to the incubator for 3.5 h. With the presence of MTT, the experiment was conducted in a laminar flow hood with the lights off and the plate was wrapped in aluminum foil. The media were then removed with an aspirator and the remained formazan crystals in each well were dissolved with 100 μL of 100% DMSO. Absorbance was measured at 570 nm to determine the MTT signal and at 630 nm to determine background. The data were normalized to those from cells treated with 1% sodium dodecyl sulfate (SDS) to obtain a value of 0%, and to those from cells treated with PBS to obtain a value of 100%.

Fibril seeding experiment in the aSyn biosensor cells. Based on a published protocol[36], FRET-based aSyn biosensor cells, HEK293T cells expressing disease-associated aSyn A53T mutant fused with CFP or YFP, were grown in DMEM (4mM L-glutamine and 25 mM D-glucose) supplemented with 10% FBS and 1% penicillin/streptomycin. Trypsin-treated HEK293T cells were harvested, seeded on flat 96-well plates at a concentration of 4×10^4 cells per well in 200 μL culture medium per well, and incubated in 5% CO_2 at 37 °C.

After 18 h, aSyn fibrils were prepared by diluting with Opti-MEM™ (Life Technologies, Carlsbad CA, USA) and sonicating in a water bath sonicator for 10 min. The fibril samples were then mixed with Lipofectamine™ 2000 (Thermo Fisher Scientific) and incubated for 15 min and then added to the cells. The actual volume of Lipofectamine™ 2000 was calculated based on the dose of 1 μL per well. After 48 h of transfection, the cells were trypsinized, transferred to a 96-well round-bottom plate, and resuspended in 200 μL

chilled flow cytometry buffer (Hank's balanced salt solution, 1% FBS, and 1 mM EDTA) containing 2% paraformaldehyde. The plate was sealed with parafilm and stored at 4 °C for flow cytometry.

No apparent toxicity is observed at the tested concentrations of aSyn fibrils used in the seeding assay (Supplementary Fig. 13), which rules out the contribution of cell death to aSyn seeding.

Flow cytometry-based FRET analysis. Intracellular aSyn aggregation or inclusions were quantified by the flow cytometry-based FRET analysis. The protocol was adapted from the Diamond laboratory[37]. The fluorescence signals of the cells were measured using the settings for CFP (ex. 405 nm, em. 405/50 nm filter), YFP (ex. 488 nm, em. 525/50 nm filter), and FRET (ex. 405 nm, em. 525/50 nm filter) with an LSRII Analytic Flow Cytometer (BD Biosciences). FRET signals were used to differentiate the aggregated aSyn from the non-aggregated aSyn. A bivariate plot of FRET vs. CFP was created to introduce a polygon gate to exclude all of the FRET-negative cells treated with only Lipofectamine and to include the FRET-positive cells treated with fibril seeds (Supplementary Fig. 3). The integrated FRET density, calculated by multiplying the percentage of FRET-positive cells by the mean fluorescence intensity of the FRET-positive cells, was reported in the results.

Statistical analysis. All statistical analyses were performed in SigmaPlot version 13.0 (Systat Software Inc., San Jose, CA, USA). The Grubbs' test was used to exclude outliers. One-way analysis of variances were used to assess differences between the fibril-treated and control-treated cells in the in vitro cytotoxicity assay. P values <0.01 were considered statistically significant.

Data availability

The cryo-EM density maps of the rod and twister polymorphs have been deposited in the Electron Microscopy Data Bank under accession number EMD-7618 and EMD-7619, respectively, with associated atomic coordinates deposited in the RCSB Protein Data Bank under accession number 6CU7 and 6CU8, respectively. Other data are available from the corresponding authors upon reasonable request.

Received: 19 June 2018 Accepted: 6 August 2018
Published online: 06 September 2018

References

1. Angot, E. Alpha-synuclein cell-to-cell transfer and seeding in grafted dopaminergic neurons in vivo. *PLoS ONE* **7**, e35671 (2012).
2. Grazia Spillantini, M. et al. Filamentous α-synuclein inclusions link multiple system atrophy with Parkinson's disease and dementia with Lewy bodies. *Neurosci. Lett.* **251**, 205–208 (1998).
3. Spillantini, M. G., Crowther, R. A., Jakes, R., Hasegawa, M. & Goedert, M. Alpha-Synuclein in filamentous inclusions of Lewy bodies from Parkinson's disease and dementia with lewy bodies. *Proc. Natl. Acad. Sci. USA* **95**, 6469–6473 (1998).
4. Vilar, M. et al. The fold of alpha-synuclein fibrils. *Proc. Natl Acad. Sci. USA* **105**, 8637–8642 (2008).
5. Bousset, L. et al. Structural and functional characterization of two alpha-synuclein strains. *Nat. Commun.* **4**, 2575 (2013).
6. Peelaerts, W. et al. α-Synuclein strains cause distinct synucleinopathies after local and systemic administration. *Nature* **522**, 340–344 (2015).
7. Peng, C. et al. Cellular milieu imparts distinct pathological α-synuclein strains in α-synucleinopathies. *Nature* **1**, https://doi.org/10.1038/s41586-018-0104-4 (2018).
8. Rodriguez, J. A. et al. Structure of the toxic core of α-synuclein from invisible crystals. *Nature* **525**, 486–490 (2015).
9. Tuttle, M. D. et al. Solid-state NMR structure of a pathogenic fibril of full-length human α-synuclein. *Nat. Struct. Mol. Biol.* **23**, 409–415 (2016).
10. Crowther, R. A., Daniel, S. E. & Goedert, M. Characterisation of isolated α-synuclein filaments from substantia nigra of Parkinson's disease brain. *Neurosci. Lett.* **292**, 128–130 (2000).
11. Prusiner, S. B. et al. Evidence for α-synuclein prions causing multiple system atrophy in humans with parkinsonism. *Proc. Natl Acad. Sci. USA* **112**, E5308–E5317 (2015).
12. Norel, R., Lin, S. L., Wolfson, H. J. & Nussinov, R. Shape complementarity at protein–protein interfaces. *Biopolymers* **34**, 933–940 (1994).
13. Zarranz, J. J. et al. The new mutation, E46K, of α-synuclein causes Parkinson and Lewy body dementia. *Ann. Neurol.* **55**, 164–173 (2004).
14. Appel-Cresswell, S. et al. Alpha-synuclein p.H50Q, a novel pathogenic mutation for Parkinson's disease. *Mov. Disord.* **28**, 811–813 (2013).
15. Lesage, S. et al. G51D α-synuclein mutation causes a novel Parkinsonian-pyramidal syndrome. *Ann. Neurol.* **73**, 459–471 (2013).
16. Pasanen, P. et al. A novel α-synuclein mutation A53E associated with atypical multiple system atrophy and Parkinson's disease-type pathology. *Neurobiol. Aging* **35**, 2180.e1–e5 (2014).
17. Lee, M. K. et al. Human alpha-synuclein-harboring familial Parkinson's disease-linked Ala-53 --> Thr mutation causes neurodegenerative disease with alpha-synuclein aggregation in transgenic mice. *Proc. Natl Acad. Sci. USA* **99**, 8968–8973 (2002).
18. Yoshino, H. et al. Homozygous alpha-synuclein p.A53V in familial Parkinson's disease. *Neurobiol. Aging* **57**, 248.e7–248.e12 (2017).
19. Guerrero-Ferreira, R. et al. Cryo-EM structure of alpha-synuclein fibrils. *Elife* **7**, e36402 (2018).
20. Fitzpatrick, A. W. P. et al. Cryo-EM structures of tau filaments from Alzheimer's disease. *Nature* **547**, 185–190 (2017).
21. Gremer, L. et al. Fibril structure of amyloid-β(1–42) by cryo-electron microscopy. *Science (80-.).* **358**, 116–119 (2017).
22. Miyazawa, A., Fujiyoshi, Y. & Unwin, N. Structure and gating mechanism of the acetylcholine receptor pore. *Nature* **423**, 949–955 (2003).
23. Zhang, X., Jin, L., Fang, Q., Hui, W. H. & Zhou, Z. H. 3.3 Å Cryo-EM structure of a nonenveloped virus reveals a priming mechanism for cell entry. *Cell* **141**, 472–482 (2010).
24. Suloway, C. et al. Automated molecular microscopy: the new Leginon system. *J. Struct. Biol.* **151**, 41–60 (2005).
25. Guenther, E. L. et al. Atomic-level evidence for packing and positional amyloid polymorphism by segment from TDP-43 RRM2. *Nat. Struct. Mol. Biol.* https://doi.org/10.1038/s41594-018-0045-5 (2018).
26. Rohou, A. & Grigorieff, N. CTFFIND4: fast and accurate defocus estimation from electron micrographs. *J. Struct. Biol.* **192**, 216–221 (2015).
27. Ludtke, S. J., Baldwin, P. R. & Chiu, W. EMAN: semiautomated software for high-resolution single-particle reconstructions. *J. Struct. Biol.* **128**, 82–97 (1999).
28. Scheres, S. H. W. RELION: implementation of a Bayesian approach to cryo-EM structure determination. *J. Struct. Biol.* **180**, 519–530 (2012).
29. Rosenthal, P. B. & Henderson, R. Optimal determination of particle orientation, absolute hand, and contrast loss in single-particle electron cryomicroscopy. *J. Mol. Biol.* **333**, 721–745 (2003).
30. Brunger, A. T. Version 1.2 of the crystallography and nmr system. *Nat. Protoc.* **2**, 2728–2733 (2007).
31. Ge, P. & Zhou, Z. H. Hydrogen-bonding networks and RNA bases revealed by cryo electron microscopy suggest a triggering mechanism for calcium switches. *Proc. Natl Acad. Sci. USA* **108**, 9637–9642 (2011).
32. Adams, P. D. et al. PHENIX: a comprehensive Python-based system for macromolecular structure solution. *Acta Crystallogr. Sect. D* **66**, 213–221 (2010).
33. Leaver-Fay, A. et al. Rosetta3: an object-oriented software suite for the simulation and design of macromolecules. *Methods Enzymol.* **487**, 545–574 (2011).
34. Arvai, A. A program to display X-ray diffraction images. http://www.scripps.edu/tainer/arvai/adxv.html (2015).
35. Notes, I. A. Proliferation assay MTT protocol. *Wallert Provast Lab*. https://doi.org/10.1007/978-1-61779-080-5_20, 1–2 (2007).
36. Holmes, B. B. et al. Proteopathic tau seeding predicts tauopathy in vivo. *Proc. Natl Acad. Sci. USA* **111**, E4376–E4385 (2014).
37. Furman, J. L., Holmes, B. B. & Diamond, M. I. Sensitive detection of proteopathic seeding activity with FRET flow cytometry. *J. Vis. Exp.* https://doi.org/10.3791/53205 (2015).

Acknowledgements

We thank Ivo Atanasov for technical assistance in cryo-EM. We acknowledge the use of instruments at the Electron Imaging Center for Nanomachines supported by UCLA and by instrumentation grants from NIH (1S10RR23057 and 1U24GM116792) and NSF (DBI-1338135 and DMR-1548924). We acknowledge computing resource support from XSEDE (MCB140140), which is supported by NSF (ACI-1053575). We also thank the Diamond Laboratory (UT Southwestern) for providing the aSyn biosensor cells. This work was supported by departmental recruitment funds to L.J. This research was also supported in part by National Institutes of Health (AG029430 to D.S. E., GM071940 and AI094386 to Z.H.Z.). K.A.M. is supported by the UCLA Medical Scientist Training Program (GM08042) and UCLA Chemistry-Biology Interface training grant (USPHS National Research Service Award 5T32GM008496). D.S.E. is supported by the Howard Hughes Medical Institute (HHMI).

Author contributions

L.J., Z.H.Z., and D.S.E. designed and supervised the research. B.L. characterized the αSyn fibrils, performed in vitro seeding and toxicity experiments, and analyzed data. P.G. performed the cryo-EM studies, processed data, and calculated the maps. K.A.M. and M.R.S. refined the models and simulated fiber powder diffraction. D.R.B. assisted in cryo-EM data processing. P.G., S.Y., K.A.M., and M.R.S. built atomic models. P.S., B.L., and M.Z. prepared αSyn and optimized fibril growing conditions.

G.N. and W.S.S. helped with in vitro seeding and toxicity experiments. B.L., K.A.M., P.G., D.S.E., Z.H.Z., and L.J. wrote the manuscript with the input from all authors.

Additional information

Supplementary Information accompanies this paper at https://doi.org/10.1038/s41467-018-05971-2.

Competing interests: D.S.E. is an advisor and equity shareholder in ADRx Inc. The other authors declare no competing interests.

Reprints and permission information is available online at http://npg.nature.com/reprintsandpermissions/

Publisher's note: Springer Nature remains neutral with regard to jurisdictional claims in published maps and institutional affiliations.

Supplementary Information

for

Cryo-EM of full-length α-synuclein reveals fibril polymorphs with a common structural kernel

B. Li, P. Ge & K. A. Murray. *et al*.

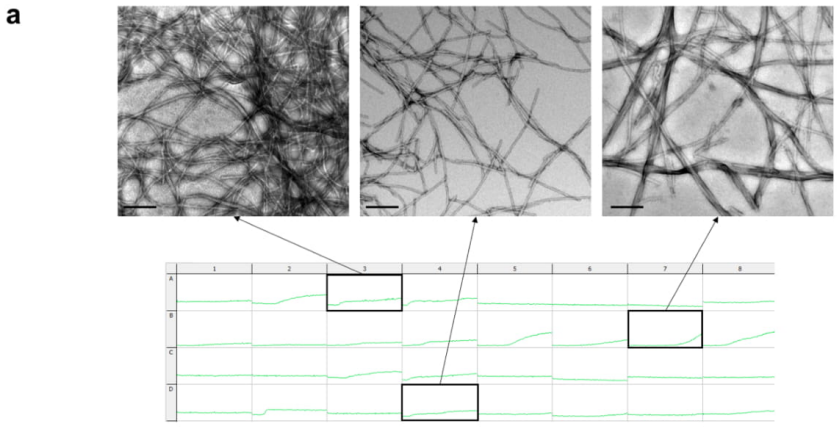

Supplementary Figure 1

Various fibril growth conditions yielded a range of human aSyn fibril polymorphs

The aggregation kinetics of the full-length human aSyn fibril growth were monitored by thioflavin T assay in various pH, salts, and additives in quiescent conditions for more than 14 days (fibril growth conditions described in Methods). The fibril morphology was subsequently characterized using negative-stain EM. Lower panels show example plots of ThT kinetics data. Upper panels show selected EM images from ThT-positive conditions, displaying a variety of fibril morphologies. Out of hundreds of fibril growth conditions screened, one fibril preparation (300 μM aSyn, 15mM tetrabutylphosphonium bromide, room temperature) with well-separated single filaments (Supplementary Fig. 2) was selected for further characterization. Scale bar: 200 nm.

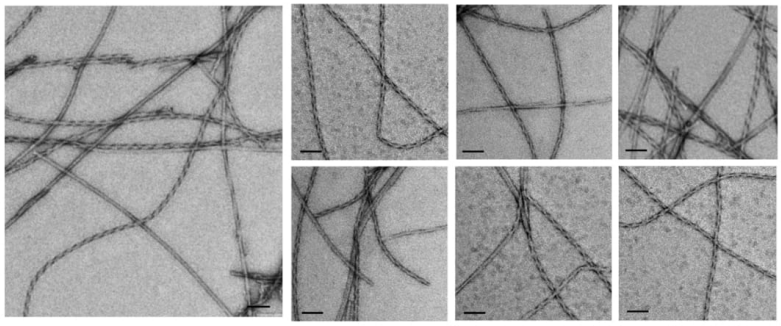

Supplementary Figure 2

Additional negative stain EM images of the aSyn fibril preparation selected for further characterization.

The fibril preparation (300 μM aSyn, 15mM tetrabutylphosphonium bromide, room temperature) was used for structural and biochemical characterization for the rest of our study. This fibril preparation displayed well-separated twisted or non-twisted filaments, where the rod and twister polymorphs are the two major populations. Scale bar: 100 nm.

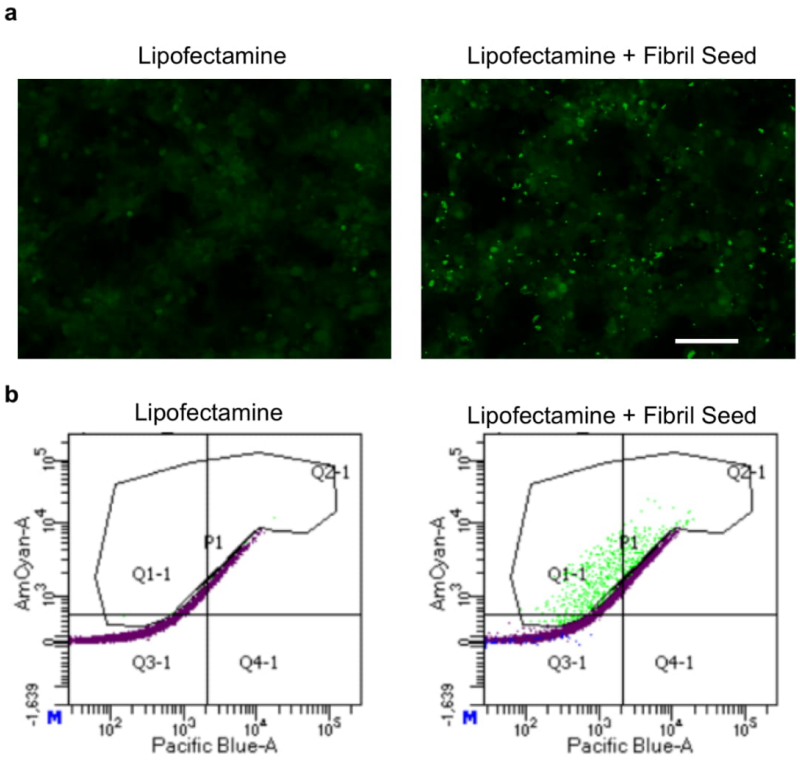

Supplementary Figure 3

Selection criteria for FRET analysis of seeded aSyn aggregation

(**a**) Transduction of 100 nM fibrils induced cellular aSyn aggregation as indicated by fluorescent puncta (right panel) in the aSyn biosensor cells[1]. Fluorescent images of aSyn Biosensor cells obtained 48 hours after treatment of Lipofectamine only (left) or with sonicated fibrils (right). Scale bar: 100 μm. (**b**) Gating used for flow cytometry-based FRET analysis to quantify intracellular aSyn aggregation. A polygon gate include the FRET-positive cells (green dots, aSyn aggregation or inclusions in cells) treated with fibril seeds and exclude the FRET-negative cells (purple dots, non-aggregated aSyn in cells) treated with only Lipofectamine.

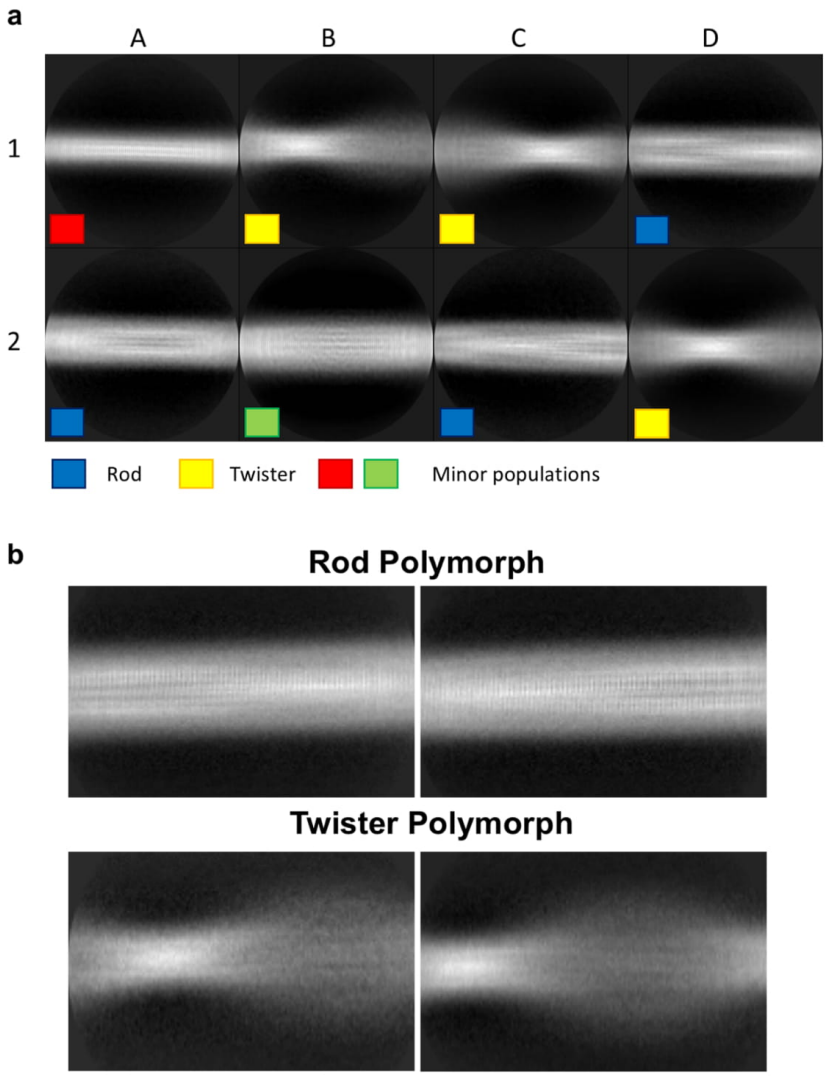

Supplementary Figure 4

2D class-averages for all extracted particles from cryo-EM images of the aSyn fibrils.

(**a**) Representatives of 2D class-averages for the two major (yellow and blue) and two minor (red and green) fibril populations. (**b**) Enlarged views of the rod and twister polymorphs to show details of the β-strand characteristic of a fibril.

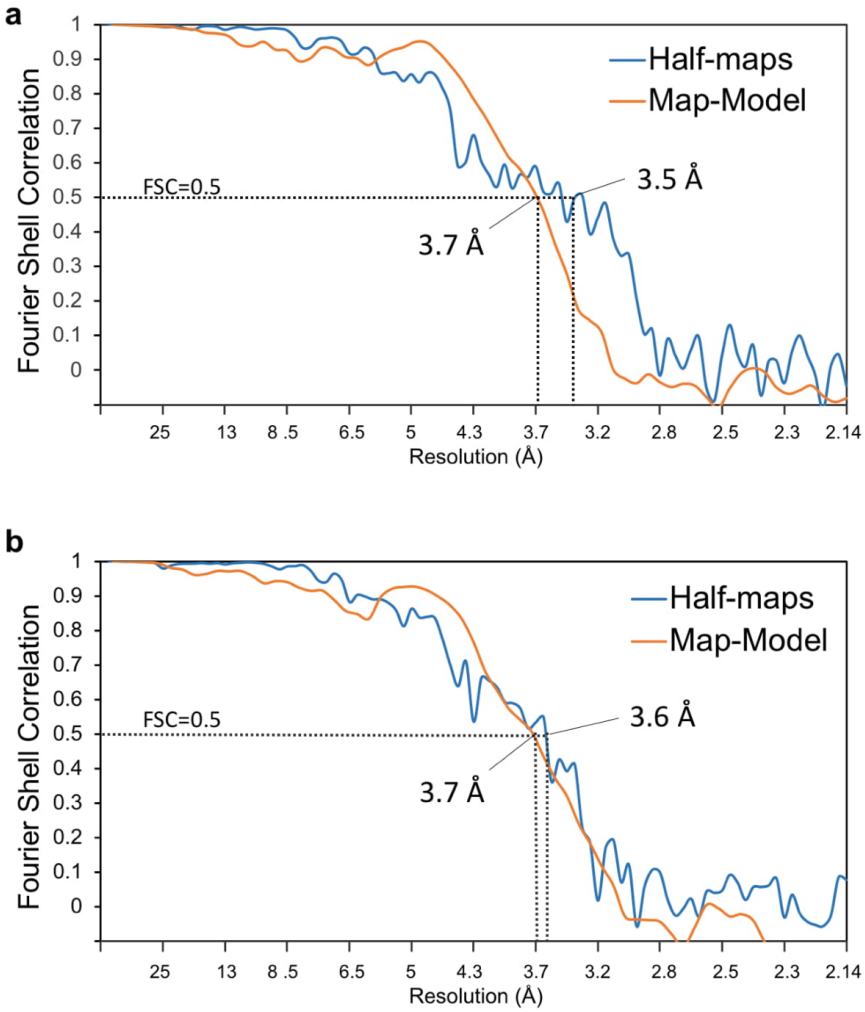

Supplementary Figure 5

Resolution estimation of the two cryo-EM maps by Fourier Shell Correlation (FSC)

An FSC cutoff value of 0.5 results in the resolutions of 3.5 Å for the half-maps and 3.7 Å for the map-model correlations for the rod polymorph (**a**) and 3.6 Å for the half-maps and 3.7 Å for the map-model correlations for the twister polymorph (**b**).

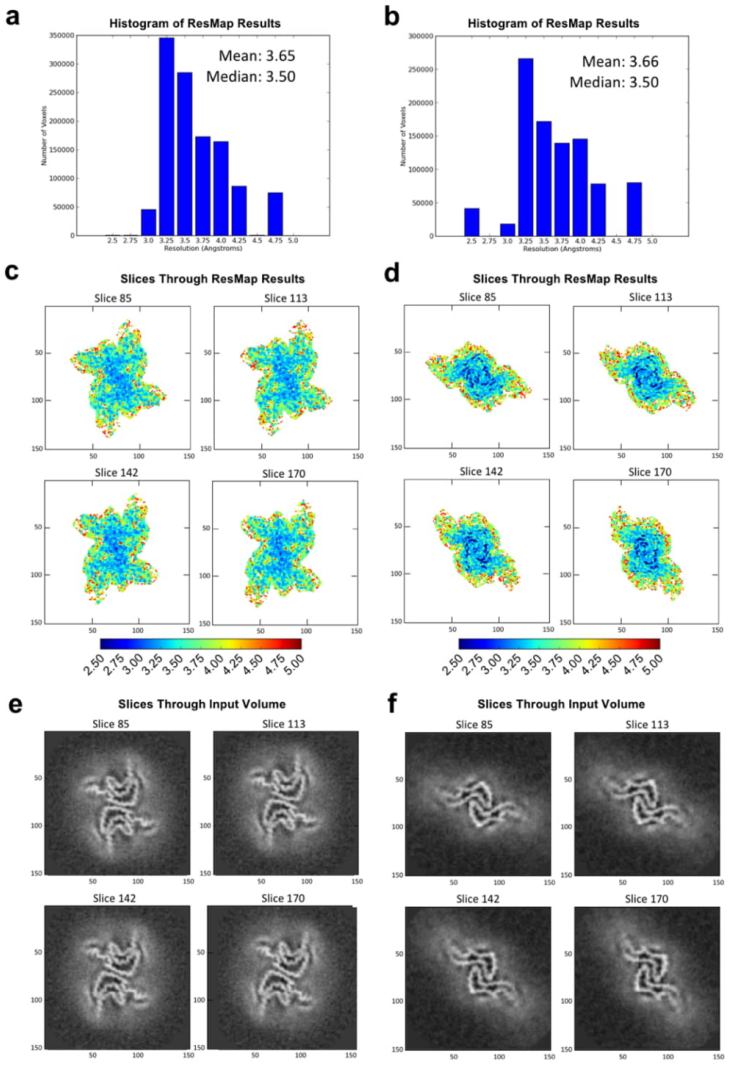

Supplementary Figure 6

Local resolution estimations for the rod (a, c and e) and twister (b, d and f) polymorphs showing good local resolution in the ordered fibril core region.

(a and **b)** Mean local resolutions for pixels within the mask for the rod polymorph is at 3.65 Å, and that for the twister polymorph is at 3.66 Å. (**c** and **d**) ResMap (Resolution Map) slices, perpendicular to the primary fibril axis, highlight good local resolutions (blue, 2.5 Å to 3.0 Å) at the central region of fibrils. (**e** and **f**) Density slices reveal a clear backbone for each fibril polymorph.

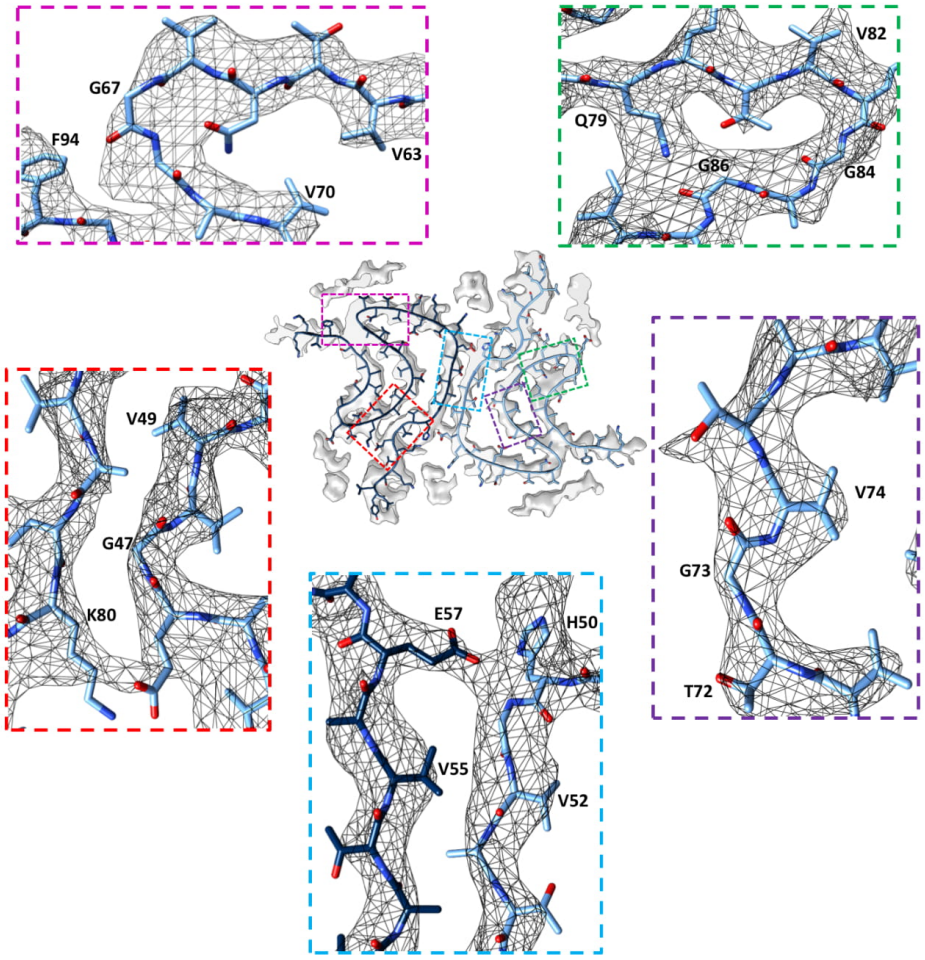

Supplementary Figure 7

Atomic model of aSyn rod polymorph structure matches well with its cryo-EM map

The atomic model shown in sticks was fit to the density map (shown in the gray chicken wire) using specific density landmarks. Large side chain densities were observed for aromatic residues (e.g. H50), and longer chain residues (e.g. E57, Q79). Areas showing reduced electron density for side chain were used to fit smaller residues (e.g. G47, G67, G73).

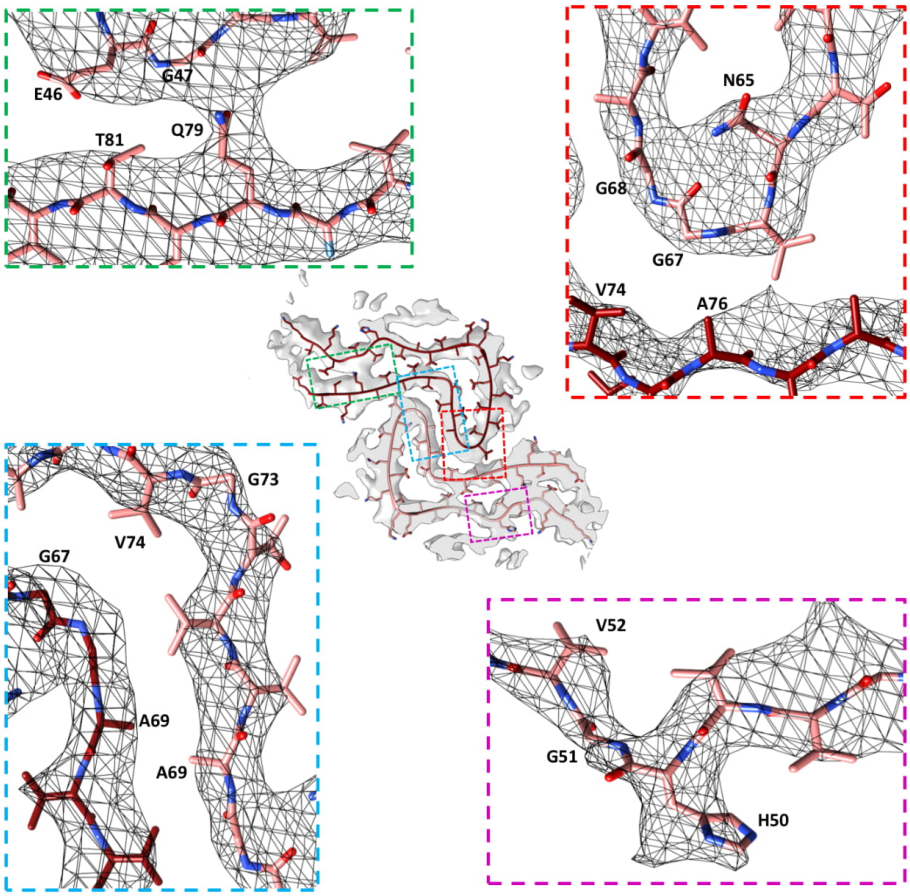

Supplementary Figure 8

Atomic model of aSyn Twister polymorph structure agrees well with its cryo-EM map

Key sidechain densities were used as landmarks and were utilized to determine the correct placement of the model. Aromatic (e.g. H50), and large charged residues (e.g. Q79) had large obvious densities branching from the backbone density.

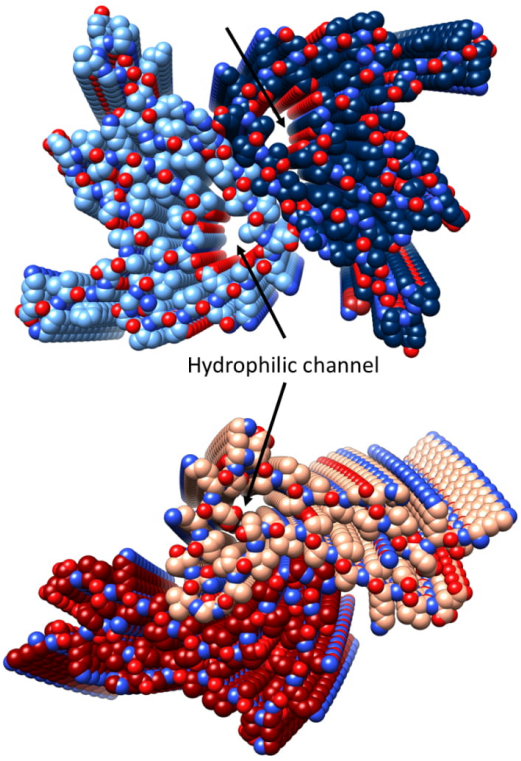

Supplementary Figure 9

Hydrophilic channels in the rod and twister structures

A hydrophilic channel, surrounded by residues T54, T59, E61, T72, and T75, locates next to the fibril core of either the rod (top) or twister (bottom) structure.

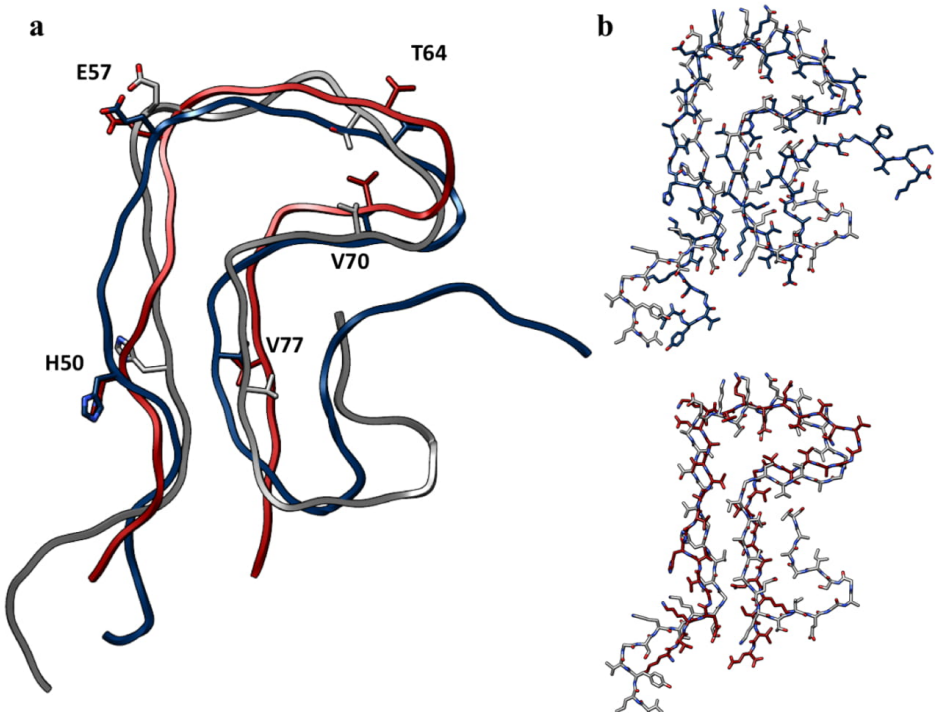

Supplementary Figure 10

Overlay of the rod and the twister protofilaments with the ssNMR protofilament

(**a**) Backbone overlay highlights resemblance in the structures between the ssNMR protofilament (gray) and the rod polymorph (blue) (Cα RMSD: 3.4 Å), ssNMR and the twister porlymorph (red) (Cα RMSD: 3.4 Å) in the 28 matched residues. (**b**) Full atomic models of the ssNMR compared with the rod polymorph (top) and the twister polymorph (bottom).

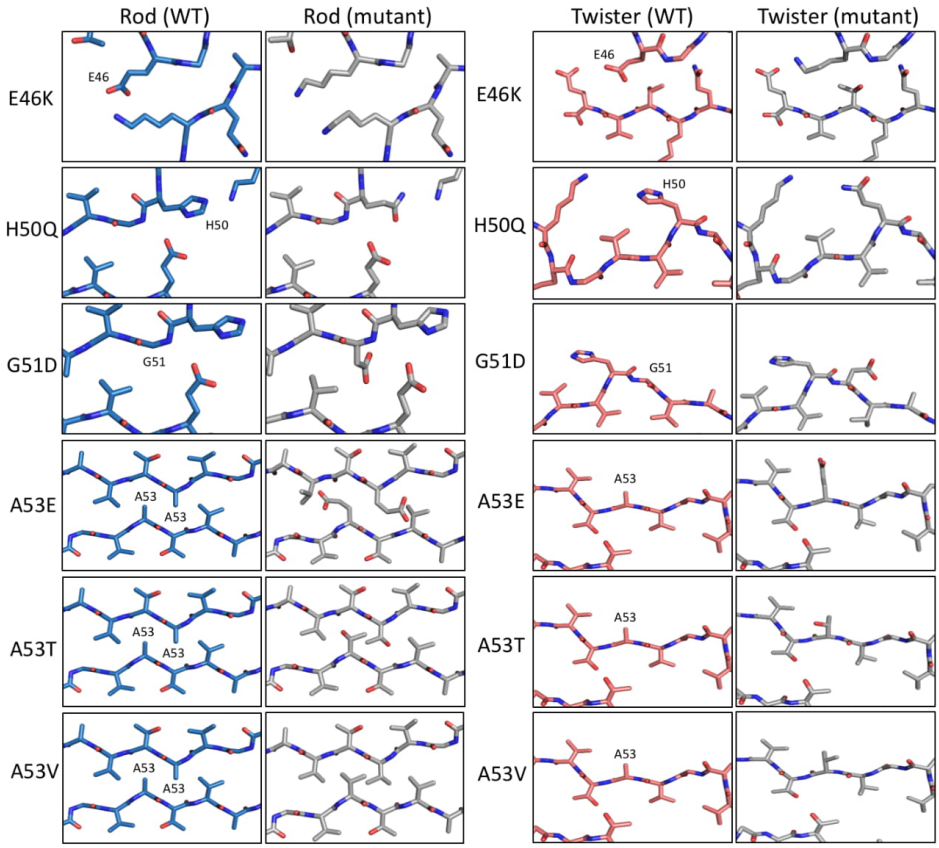

Supplementary Figure 11

Modeling of the familial mutations indicating the interruption of zipper interfaces in the rod structure

Viewed down the fibril axis, structural models of six PD familial mutations sites (E46K, H50Q, G51D, A53E, A53T and A53V) are compared with those of wild type residues in either rod (left) or twister (right) structures. The mutations are modeled upon the cryo-EM structures, and one strand from each protofilament is shown to highlight the modeled interactions. Those mutants are predicted to undermine stability in the preNAC steric zipper in the rod polymorph. On the contrary, the mutations sites in the twister structure located far from the fibril core which has little effect to the fibril core.

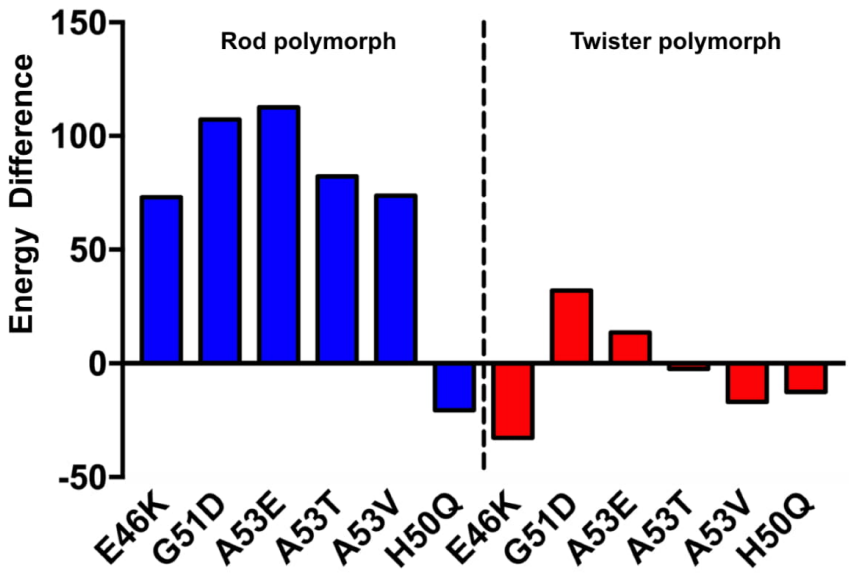

Supplementary Figure 12

Familial mutations (E46K, G51D, A53E, A53T and A53V) destabilize the rod structure (blue) while have minor impact in the twister structure (red).

Energies for the wild type and familial mutant were calculated using Rosetta[2]. The contribution of each mutant was evaluated by the score difference between the mutant and the WT. When comparing the energy evaluation in both rod and twister structures, familial mutations E46K, G51D, A53E, A53T and A53V have greater energy differences (>50 Rosetta energy units) in the rod structure, indicating most of mutants may disrupt the stability of the fibril core. Smaller energy difference (within ±30 Rosetta energy units) is observed in the twister structure.

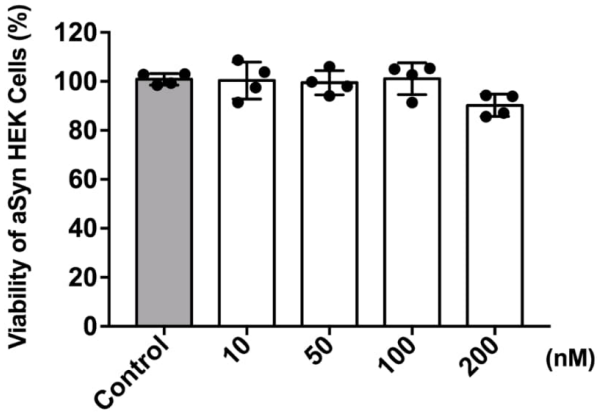

Supplementary Figure 13

Sonicated aSyn fibrils at different tested concentrations showed no significant toxicity in HEK biosensor cells

Cytotoxicity of aSyn fibrils is measured using MTT-based cell viability assay of aSyn biosensor HEK293T cells. The aSyn fibrils have shown no significant cytotoxicity at the tested concentrations up to 200 nM ($p \geq 0.05$ vs. control). Data are presented as mean ± standard error.

Supplementary References

1. Prusiner, S. B. *et al.* Evidence for α-synuclein prions causing multiple system atrophy in humans with parkinsonism. *Proc. Natl. Acad. Sci.* **112,** E5308–E5317 (2015).

2. Leaver-Fay, A. *et al.* Rosetta3: An object-oriented software suite for the simulation and design of macromolecules. *Methods in enzymology* **487,** 545–574 (2011).

CHAPTER 2

Alternative protofilamental packing arrangements of α-synuclein fibril polymorphs contribute to seeding differences in cells and in brain

Asa Hatami[1,a,**], Binsen Li[1,a], Kevin A. Murray[2], Woo Shik Shin[1], Chris J. Elias[1], Chunni Zhu[1], Mia Broad[1], Chuanqi Sun[1], Michael R. Sawaya[2], Varghese John[1,*], Lin Jiang[1,*]

1 Department of Neurology, David Geffen School of Medicine, UCLA, Los Angeles, CA 90095, USA

2 Departments of Biological Chemistry and Chemistry & Biochemistry, UCLA, Los Angeles, CA 90095, USA

[*]Correspondence to Varghese John, Drug Discovery Lab, Department of Neurology, David Geffen School of Medicine, UCLA, Los Angeles, CA 90095, USA; Email: VJohn@mednet.ucla.edu and Lin Jiang, Department of Neurology, David Geffen School of Medicine, UCLA, Los Angeles, CA 90095, USA; Email: jianglin@ucla.edu

[**]Current affiliation: Sangamo Therapeutics, Richmond, CA 94804

[a] These authors contributed equally to this paper

Asa Hatami(asahatami@gmail.com), Binsen Li(libinsen@gmail.com), Kevin A. Murray(kamurray@mednet.ucla.edu), Woo Shik Shin(austinshin7@gmail.com), Chris J. Elias(CJElias@mednet.ucla.ed0u), Chunni Zhu(ChunniZhu@mednet.ucla.edu), Mia Broad(miabroad1@gmail.com, Chuanqi Sun(sunchuanqiucla@gmail.com), Michael R. Sawaya(sawaya@mbi.ucla.edu), Varghese John(VJohn@mednet.ucla.edu), Lin Jiang(jianglin@ucla.edu)

Keywords: synucleinopathies; amyloid seeding; synuclein fibril polymorphs

Abstract

Different conformation of aggregated alpha-synuclein (aSyn) have been shown to have distinct in vitro and in vivo seeding activities, contributing to the pathogenesis of synucleinopathies. We characterized two fibrillar preparations of recombinant aSyn herein referred to as narrow and broad fibrils. The narrow fibril preparation contained two polymorphs consisting of two identical protofilaments constructed around different contact interfaces. We also identified a new polymorph of striated ribbon in the broad fibril preparation. Hypothesizing that fibril polymorphs stem from alternative packing of identical protofilament kernels, we suggested a hypothetical model for the striated ribbon polymorph, that is supported by fiber powder diffraction data. The narrow and broad fibrils showed different seeding efficiencies in cells and distinct spreading patterns in mouse brain, which may arise from structural differences in their proto-filamental packing. Drug design efforts targeting fibril formation in neurodegenerative diseases may therefore necessarily involve consideration of all concurrent fibril polymorphs.

Background

Parkinson's disease (PD), dementia with Lewy bodies (DLB), and multiple system atrophy (MSA) are three synucleinopathies characterized by pathological aggregation of aSyn in neurons and glial cells [1]. Lewy bodies (LB) and Lewy neurites are pathological hallmarks of PD and DLB, while glial cytoplasmic inclusions are found in brains of MSA patients [2,3]. Pathological aSyn aggregates can recruit and convert native aSyn monomers into an aggregated state, a process that is known as seeding. Seeding of aSyn correlates with its pathological spread in the brain, which contributes to disease progression. The spreading of α-synucleinopathy via anatomically related areas following stereotactic injections of preformed aSyn fibrils has been shown to recapitulate the progressive loss of dopaminergic neurons, a hallmark of PD [4–7]. Similarly, injection of brain homogenates from MSA patients into the brains of mice overexpressing wildtype or mutant aSyn, has been shown to lead to prion-like spread of pathology [8–10].

aSyn is an intrinsically disordered protein that can aggregate into different fibrillar polymorphs. aSyn fibril polymorphs with similar widths have been produced using recombinant aSyn and have been found in material extracted from patient brains [1,11,12]. Two *in vitro*-generated polymorphic aSyn fibrillar species (named "ribbons" and "fibrils") have been reported to have different physical characteristics and to exhibit differences in toxicity and *in vitro* [13] and *in vivo* [14] seeding properties. In a study of aSyn fibrils obtained from the brains of patients with LB disease and MSA, Peng et al. demonstrated that the two different disease-associated aSyn polymorphs had distinct conformations and seeding potencies [15]. It is thus evident that aSyn fibrillar polymorphs, either characterized based on morphology or obtained from brain tissue of patients with distinct pathologies, display differences in *in vitro* and *in vivo* seeding.

Previous structural studies on aSyn fibrils have provided us with information that helps us understand the mechanisms underlying the differential biological activities of fibrillar polymorphs. A solid-state nuclear magnetic resonance (ssNMR) structure of a single fibril filament of recombinant aSyn was characterized by a Greek-key β-sheet motif in the hydrophobic core [16]. In addition, micro-electron diffraction (microED) [17] experiments have led to the elucidation of the structures of the preNAC (residues 47-56) and NACore (Non Amyloid-β Component Core, residues 68-78) regions of aSyn, two amyloidogenic segments crucial for cytotoxicity and fibril formation (Fig. 1a). The crystal structures of the preNAC and NACore regions are characterized by a pair of interdigitated in-register beta-sheets forming a steric zipper. Despite advances in our structural understanding of different aSyn polymorphs, there is limited understanding of the relationship between the structures of aSyn fibril polymorphs and their biological effects, namely cytotoxicity and seeding. Understanding this structure-activity relationship is critical for the development of therapeutics targeting aSyn aggregation and seeding.

We set out to characterize two preparations of recombinant full-length aSyn called narrow and broad fibrils, and to study their structure-activity relationship in toxicity and seeding assays both *in vitro* and *in vivo*. Our recent cryo-EM study of the narrow aSyn fibril preparation revealed two polymorphs, rod and twister, whose atomic structures have been determined [18]. The structure of the rod polymorph is also

confirmed by cryo-EM studies from other groups [19,20]. Both polymorphs consist of two intertwined protofilaments. While these protofilaments share a conserved structure consisting of a bent beta-arch, they interact with each other via the NACore residues in the twister polymorph and via the PreNAC residues in the rod polymorph. A third polymorph called striated ribbon was identified in negative-stain EM studies of the broad fibril preparation. Resemblance between fiber powder diffraction data obtained from the narrow and broad fibril preparations led us to propose a structural model of the striated ribbon polymorph comprising alternating rod and twister polymorph subunits. Biological studies of the narrow and broad fibril preparations revealed differences in cytotoxicity, *in vitro* seeding efficiency, and region-specific seeding in mouse brain. The broad fibrils had lower toxicity than the narrow fibrils despite having enhanced seeding efficiency *in vitro.* We also observed distinct regional changes in aSyn immunoreactivity in brains of mice following intraparenchymal delivery of the two fibril preparations. Taken together, our data indicate that alternative packing arrangements among amyloid fibril polymorphs may underlie seeding differences.

Results

Identification of two distinct fibril preparations of full-length recombinant human aSyn (1-140)

In order to produce a wide range of aSyn fibril polymorphs, we screened fibril growing conditions for full-length recombinant human aSyn (1-140) by varying pH, salt, and additives. All samples were incubated under quiescent conditions for 14-30 days in order to best mimic physiological fibril growth. Fibril growth was monitored using thioflavin T (ThT) and a wide range of fibril morphologies were characterized using negative-stain transmission electron microscopy (TEM). Two of the fibril preparations exhibited distinct fibril widths. “Narrow” fibrils, a family of various well-separated single filaments with or without an apparent twist, grew in the presence of tetrabutylphosphonium bromide (an ionic liquid additive used in protein crystallization) at room temperature. The “rod” and “twister” filaments found in the narrow fibril preparation were ~10 nm wide, consistent with previously reported aSyn fibrils extracted from patient brains or generated *in vitro* [25]. “Broad” fibrils, a family of wide, striated fibrils that were sometimes curved

or rolled, grew in phosphate-buffered saline (PBS, pH 7.5) at 37°C (Fig. 1b and Additional file 1: Figure S1). The broad fibrils had a wider range of fibril widths from 20 nm to 80 nm, and appeared as lateral arrays of two to eight 10-nm-wide adjoining filaments resembling the striated ribbon polymorph previously observed for other amyloid proteins, including beta-amyloid (1-40) and amylin [26]. The individual filaments found in the broad fibril preparation were around 10 nm wide and thus similar in width to the "rod" and "twister" filaments found in the narrow fibril preparation.

The narrow and broad fibril preparations share similar fibril core structures

Fiber powder diffraction data obtained using aligned fibrils of both preparations revealed very similar cross-beta fibril structures (Fig. 1c,d). Diffraction patterns of both narrow and broad fibrils share a strong 4.7-Å reflection, which indicates that both narrow and broad fibrils result from the stacking of β-strands. The shared reflection near 8.0 Å likely arises from the distance between the adjacent pairs of β-sheets that make up the aSyn filaments, while another shared reflection near 11.5 Å likely stems from the staggering between adjacent β-sheets of the steric zipper. Both fibrils also have a reflection at 2.4 Å in their diffraction patterns. Based on the cryo-EM structures of the narrow fibrils, a helical rise of 2.4 Å defined by an approximate 2_1 screw axis of symmetry corresponds to one-half the 4.8-Å spacing between the β-strands, permitting the two sheets to interdigitate tightly. The 2.4-Å peak on the diffraction pattern of the broad fibrils thus represents the same 2_1 screw axis of symmetry with a helical rise of 2.4 Å. All the same principal peaks are also observed in the diffraction patterns of aligned NACore and preNAC peptide fibrils. The resemblances among the diffraction patterns of all of the fibril polymorphs suggest that the narrow and broad fibril preparations share similar fibril core structures involving the NACore and preNAC sequences.

The rod and twister structures together suggest a two-dimensional growth model for the striated ribbon polymorph

TEM images of the broad fibrils indicate that they are composed of adjoining filaments similar in dimensions to those found in the narrow fibril preparation (Additional file 1: Figure S1). The structural

relevance of the narrow fibrils to the broad fibrils is further established by the resemblance of their fiber diffraction patterns. Taken together, the above findings formed the basis for our model of the striated ribbon polymorph, which combines the protofilament interfaces of the rod and twister polymorphs found in the narrow fibril preparation (Fig. 1b). Instead of using one steric zipper as a contact interface between the protofilaments, as in the rod and twister fibrils, the striated fibril model is composed of alternating NACore and preNAC steric zipper interfaces extending laterally perpendicular to the primary fibril growth direction (Fig. 2a). Simulated fiber powder diffraction data calculated based on this model agree with the experimental diffraction pattern obtained using the broad fibrils (Fig. 2b). While fibril growth and extension from seeds occur mainly one-dimensionally along the primary fibril axis in the narrow fibrils, our model posits that the broad fibrils are capable of growth and seeding in both the lateral and primary fibril axis directions.

The broad and narrow aSyn fibril preparations had distinct *in vitro* seeding efficiency and cytotoxicity

The EM images and structures of the narrow and broad fibrils suggest that the fibrils in the two preparations have different modes of fibril growth, which may in turn lead to differences in seeding efficiency and cytotoxicity. To determine whether the narrow and broad fibrils differ in *in vitro* seeding efficiency, we exposed human embryonic kidney 293 T (HEK293T) cells expressing cyan fluorescent protein (CFP)- and yellow fluorescent protein (YFP)-tagged A53T aSyn (Biosensor cells) to the two different fibril preparations [9]. The broad fibrils led to a significant increase in aSyn inclusion formation as indicated by fluorescence resonance energy transfer (FRET) signal density at concentrations as low as 10 nM, while the narrow fibrils exhibited significantly lower seeding efficiency (Fig. 3a and 3b).

We characterized the cytotoxicity of both aSyn fibril preparations in differentiated PC12 cells using the 3-(4,5-dimethylthiazol-2-yl)-2,5-diphenyltetrazolium bromide (MTT) assay. The narrow fibrils led to significant cytotoxicity at concentrations as low as 500 nM, while the broad fibrils had negligible

cytotoxicity even at 2 μM (Fig. 3c). The fibril polymorphs found in the narrow fibril preparation may thus have higher toxicity than the striated ribbon polymorph comprising the broad fibril preparation.

The two aSyn fibril preparations led to differential brain region-specific changes in aSyn immunoreactivity in wild-type mice

The distinct *in vitro* seeding efficiencies of the narrow and broad fibrils encouraged us to perform an initial proof-of-concept study to investigate the seeded spread of aSyn in the basal ganglia of wild-type mice. The motor cortex is an integral part of the basal ganglia circuit and has reciprocal neuronal connections with the striatum [27], a key region of dysfunction in PD [28]. We stereotactically injected sonicated aSyn fibrils into the motor cortex of 6-month-old wild-type mice (Fig. 4a). Injecting into the motor cortex enabled us to focus on the seeded spread of the two aSyn fibril preparations in the nigrostriatal pathway while excluding potential local effects of the injected material in the striatum or substantia nigra (SN). The fibril injections led to no obvious health effect in the mice: there were no significant weight differences between the groups treated with fibrils and the vehicle-treated group (Additional file 1: Figure S4). Histological experiments performed 5 months after the injections revealed no loss of tyrosine hydroxylase (TH) immunoreactivity in the SN or striatum (Additional file 1: Figure S2 and S3), suggesting that neither fibril preparation led to gross toxicity to dopaminergic neurons. However, we observed region-specific alterations in aSyn immunoreactivity following injections of the fibrils.

We assessed changes in aSyn immunoreactivity in brain regions connected via basal ganglia pathways (cortex, striatum, and SN). We studied the cortex and striatum at three different levels (rostral, medial, and caudal). Injections of the narrow and broad fibril preparations into the motor cortex led to distinct brain region-specific changes in aSyn immunoreactivity (Fig. 4b). Immunofluorescence studies using two monoclonal aSyn antibodies (Clone 42 and Syn303) revealed that the narrow fibrils led to reductions in the pool of aSyn conformers displaying the epitope for the antibody Clone 42 in the medial striatum and cortex, while increasing the pool of Syn303-reactive aSyn in the rostral striatum. In contrast, the broad fibrils led to reduced Clone 42 and Syn303 staining in the SN as well as a decrease in Syn303 staining in the rostral

cortex, where we observed no significant changes following administration of the narrow fibrils (Fig. 4b,c). Unlike the narrow fibrils, the broad fibrils led to aSyn conformational changes in the SN, a brain area more distant from the site of injection than the striatum.

Discussion

Our recent cryo-EM structural studies [18] revealed that protofilaments of the rod and twister fibrils assemble symmetrically about homo-zippers of the preNAC and NACore segments, respectively. Since the twister and rod polymorphs have structurally conserved kernels that interact at either the preNAC or NACore segments, the polymorphism in these fibrils is determined by the location of the protofilament packing interface instead of the kernel structure. Alternating interactions at the preNAC and NACore zippers would enable lateral expansion of the protofilaments, as we propose occurs in the striated ribbon fibrils (Fig. 1b). The hypothetical model presented in Fig. 3 provides an example of what we have termed combinatorial polymorphism. If this combined model in fact represents the structure of the striated ribbon, we believe that it is the first observed example of combinatorial polymorphism in amyloid proteins.

The narrow fibrils displayed higher cytotoxicity than the broad fibrils despite having lower seeding efficiency. The different trends for cytotoxicity and seeding efficiency illustrate that seeding is not necessarily directly associated with cytotoxicity, as previously demonstrated for tau [29]. aSyn fibril preparations, whether obtained from brain tissue or produced *in vitro*, may have different compositions of polymorphs. Each polymorph is distinguished by packing differences between protofilament kernels and makes distinct contributions to the biological activities of seeding and cytotoxicity. The narrow and broad fibril preparations containing fibril polymorphs with different compositions thus have discrete seeding efficiency and cytotoxicity profiles, which may not be necessarily correlated. Therefore, it is essential to characterize the biological functions of each individual polymorph in the sample in order to understand the pathological roles of complex polymorphic fibril preparations.

Structural studies of the three polymorphs suggest a two-dimensional mode of growth in the striated ribbon fibril, rather than the primary, one-dimensional fiber growth in the rod and twister fibrils. Our *in vitro* experiments confirmed the enhanced seeding capability of the broad fibril preparation when compared to the narrow fibril preparation. In our *in vivo* experiments, the aSyn fibril preparations displayed seeded spreading to brain regions away from the injection site. Immunofluorescence experiments revealed that the broad fibrils caused changes in a brain region more distant from the injection site than that affected by the narrow fibrils, consistent with the enhanced seeding efficiency of the broad fibrils *in vitro*. Interestingly, the two fibril preparations caused distinct alterations in aSyn conformation in different brain regions (cortex, striatum, and SN), as indicated by changes in the pattern of aSyn immunoreactivity. The polymorphic structures in the broad and narrow fibrils underlie different modes of fibril growth and may underlie the observed differences in seeded spreading *in vivo*. Also worth noting is that the conformations of aSyn fibrils have been reported to be determined by both the nature of the fibril seeds and by the cellular milieu [15]. Thus, interplay of the polymorphic structures of the fibril preparations and the cellular environments of the different brain regions may further contribute to the distinct patterns of aSyn seeded spread.

This study was not adequately powered for the assessment of potential behavioral changes associated with the injection of the different aSyn fibrillar preparations. Nevertheless, we performed an exploratory open field test prior to euthanasia to determine whether administration of the aSyn fibrils led to any changes in motor behavior. Interestingly, preliminary data suggest that the different preparations led to distinct changes in motor behavior in the open field test, with a trend for increased activity following administration of the narrow fibrils and a trend for decreased activity associated with injection of the broad fibrils (data not shown). Future studies to thoroughly investigate behavioral alterations associated with the brain region-specific changes in aSyn expression in wild-type mice and transgenic models of PD and MSA following injection of the different fibril preparations will be important in further establishing the biological relevance of the aSyn polymorphs described here.

Conclusions

Here we identified a new combinatorial polymorphism for amyloid fibrils based on cryo-EM structures of the two fibril polymorphs found in the narrow fibrils and fiber diffraction data from the narrow and broad fibril preparations. Our *in vitro* and *in vivo* seeding studies confirmed that the two fibril preparations have distinct *in vitro* seeding and seeded spread in mouse brain that may be linked to behavioral changes. The structural and functional studies presented here establish the need to consider the contributions of all polymorphs and their relevance to overall pathogenesis when performing future rational design campaign for therapeutic agents based on amyloid fibril structure.

Abbreviations

aSyn, Alpha-synuclein; CFP, Cyan fluorescent protein; CTX, Cortex; DLB, Dementia with Lewy bodies; DMEM, Dulbecco's modification of Eagle's medium; EM, Electron microscopy; FBS, Fetal bovine serum; FRET, Fluorescence resonance energy transfer, IPTG: Isopropyl β- d-1-thiogalactopyranoside; HEK293T, Human embryonic kidney 293 T; LB, Lewy bodies; microED, Micro-electron diffraction; MSA, Multiple system atrophy; MTT, 3-(4,5-dimethylthiazol-2-yl)-2,5-diphenyltetrazolium bromide; NACore, Non Amyloid-β Component Core; PBS, Phosphate-buffered saline; SN, Substantia nigra; SNpc, Substantia nigra pars compact; SNr, Substantia nigra pars reticulata; STR, Striatum; ssNMR, Solid-state nuclear magnetic resonance; TEM, Transmission electron microscopy; TH, Tyrosine hydroxylase; ThT, Thioflavin T; YFP, Yellow fluorescent protein

Availability of supporting data

The datasets generated during and/or analyzed during the current study are available from the corresponding author on reasonable request.

Funding

This work was supported by National Institutes of Health grants (R01AG060149, R21AG052195 and R03NS111482).

Authors' contributions

L.J., and V.J. designed and supervised the research. A.H. performed mouse experiments and analyzed data. B.L. characterized the αSyn fibrils, performed *in vitro* seeding and toxicity experiments and analyzed data. W.S.S. and C.S. helped with *in vitro* seeding and toxicity experiments. K.A.M. and M.R.S. built atomic models and simulated fiber powder diffraction. C.Z., C.E.,and M.B. performed immunostaining and helped with the mouse experiments. A.H, B.L., K.A.M., and L.J. wrote the manuscript with input from all authors.

Acknowledgements

We thank Dr. Marie-Francoise Chesselet for her help and advice in initiating the *in vivo* study. We thank the Diamond Laboratory (UT Southwestern) for providing the aSyn biosensor cells.

References

(1) Spillantini, M. G.; Crowther, R. A.; Jakes, R.; Hasegawa, M.; Goedert, M. Alpha-Synuclein in Filamentous Inclusions of Lewy Bodies from Parkinson's Disease and Dementia with Lewy Bodies. *Proc. Natl. Acad. Sci.* **1998**, *95* (11), 6469–6473. https://doi.org/10.1073/pnas.95.11.6469.

(2) Spillantini, M. G.; Schmidt, M. L.; Lee, V. M.-Y.; Trojanowski, J. Q.; Jakes, R.; Goedert, M. Alpha-Synuclein in Lewy Bodies. *Nature* **1997**, *388* (6645), 839–840. https://doi.org/10.1038/42166.

(3) Tu, P. H.; Galvin, J. E.; Baba, M.; Giasson, B.; Tomita, T.; Leight, S.; Nakajo, S.; Iwatsubo, T.; Trojanowski, J. Q.; Lee, V. M. Y. Glial Cytoplasmic Inclusions in White Matter Oligodendrocytes of Multiple System Atrophy Brains Contain Insoluble α-Synuclein. *Ann. Neurol.* **1998**, *44* (3), 415–422. https://doi.org/10.1002/ana.410440324.

(4) Luk, K. C.; Kehm, V. M.; Zhang, B.; O'Brien, P.; Trojanowski, J. Q.; Lee, V. M. Y. Intracerebral Inoculation of Pathological α-Synuclein Initiates a Rapidly Progressive Neurodegenerative α-Synucleinopathy in Mice. *J. Exp. Med.* **2012**, *209* (5), 975–986. https://doi.org/10.1084/jem.20112457.

(5) Paumier, K. L.; Luk, K. C.; Manfredsson, F. P.; Kanaan, N. M.; Lipton, J. W.; Collier, T. J.; Steece-Collier, K.; Kemp, C. J.; Celano, S.; Schulz, E.; et al. Intrastriatal Injection of Pre-Formed Mouse α-Synuclein Fibrils into Rats Triggers α-Synuclein Pathology and Bilateral Nigrostriatal Degeneration. *Neurobiol. Dis.* **2015**, *82*, 185–199. https://doi.org/10.1016/j.nbd.2015.06.003.

(6) Abdelmotilib, H.; Maltbie, T.; Delic, V.; Liu, Z.; Hu, X.; Fraser, K. B.; Moehle, M. S.; Stoyka, L.; Anabtawi, N.; Krendelchtchikova, V.; et al. α-Synuclein Fibril-Induced Inclusion Spread in Rats and Mice Correlates with Dopaminergic Neurodegeneration. *Neurobiol. Dis.* **2017**, *105*, 84–98. https://doi.org/10.1016/j.nbd.2017.05.014.

(7) Kim, S.; Kwon, S.-H.; Kam, T.-I.; Panicker, N.; Karuppagounder, S. S.; Lee, S.; Lee, J. H.; Kim, W. R.; Kook, M.; Foss, C. A.; et al. Transneuronal Propagation of Pathologic α-Synuclein from the Gut to the Brain Models Parkinson's Disease. *Neuron* **2019**, *103* (4), 627–641. https://doi.org/10.1016/j.neuron.2019.05.035.

(8) Watts, J. C.; Giles, K.; Oehler, A.; Middleton, L.; Dexter, D. T.; Gentleman, S. M.; DeArmond, S. J.; Prusiner, S. B. Transmission of Multiple System Atrophy Prions to Transgenic Mice. *Proc. Natl. Acad. Sci. U. S. A.* **2013**, *110* (48), 19555–19560. https://doi.org/10.1073/pnas.1318268110.

(9) Prusiner, S. B.; Woerman, A. L.; Mordes, D. A.; Watts, J. C.; Rampersaud, R.; Berry, D. B.; Patel, S.; Oehler, A.; Lowe, J. K.; Kravitz, S. N.; et al. Evidence for α-Synuclein Prions Causing Multiple System Atrophy in Humans with Parkinsonism. *Proc. Natl. Acad. Sci.* **2015**, *112* (38), E5308–E5317. https://doi.org/10.1073/pnas.1514475112.

(10) Bernis, M. E.; Babila, J. T.; Breid, S.; Wüsten, K. A.; Wüllner, U.; Tamgüney, G. Prion-like Propagation of Human Brain-Derived Alpha-Synuclein in Transgenic Mice Expressing Human Wild-Type Alpha-Synuclein. *Acta Neuropathol. Commun.* **2015**. https://doi.org/10.1186/s40478-015-0254-7.

(11) Spillantini, M.; Anthony Crowther, R.; Jakes, R.; Cairns, N. J.; Lantos, P. L.; Goedert, M. Filamentous α-Synuclein Inclusions Link Multiple System Atrophy with Parkinson's Disease and Dementia with Lewy Bodies. *Neurosci. Lett.* **1998**, *251* (3), 205–208. https://doi.org/10.1016/S0304-3940(98)00504-7.

(12) Vilar, M.; Chou, H.-T.; Lührs, T.; Maji, S. K.; Riek-Loher, D.; Verel, R.; Manning, G.; Stahlberg,

H.; Riek, R. The Fold of Alpha-Synuclein Fibrils. *Proc. Natl. Acad. Sci.* **2008**, *105* (25), 8637–8642. https://doi.org/10.1073/pnas.0712179105.

(13) Bousset, L.; Pieri, L.; Ruiz-Arlandis, G.; Gath, J.; Jensen, P. H.; Habenstein, B.; Madiona, K.; Olieric, V.; Böckmann, A.; Meier, B. H.; et al. Structural and Functional Characterization of Two Alpha-Synuclein Strains. *Nat. Commun.* **2013**, *4*. https://doi.org/10.1038/ncomms3575.

(14) Peelaerts, W.; Bousset, L.; Van Der Perren, A.; Moskalyuk, A.; Pulizzi, R.; Giugliano, M.; Van Den Haute, C.; Melki, R.; Baekelandt, V. α-Synuclein Strains Cause Distinct Synucleinopathies after Local and Systemic Administration. *Nature* **2015**, *522* (7556), 340–344. https://doi.org/10.1038/nature14547.

(15) Peng, C.; Gathagan, R. J.; Covell, D. J.; Medellin, C.; Stieber, A.; Robinson, J. L.; Zhang, B.; Pitkin, R. M.; Olufemi, M. F.; Luk, K. C.; et al. Cellular Milieu Imparts Distinct Pathological α-Synuclein Strains in α-Synucleinopathies. *Nature* **2018**, *557*, 558–563.

(16) Tuttle, M. D.; Comellas, G.; Nieuwkoop, A. J.; Covell, D. J.; Berthold, D. A.; Kloepper, K. D.; Courtney, J. M.; Kim, J. K.; Barclay, A. M.; Kendall, A.; et al. Solid-State NMR Structure of a Pathogenic Fibril of Full-Length Human α-Synuclein. *Nat. Struct. Mol. Biol.* **2016**, *23* (5), 409–415. https://doi.org/10.1038/nsmb.3194.

(17) Rodriguez, J. A.; Ivanova, M. I.; Sawaya, M. R.; Cascio, D.; Reyes, F. E.; Shi, D.; Sangwan, S.; Guenther, E. L.; Johnson, L. M.; Zhang, M.; et al. Structure of the Toxic Core of α-Synuclein from Invisible Crystals. *Nature* **2015**, *525* (7570), 486–490. https://doi.org/10.1038/nature15368.

(18) Li, B.; Ge, P.; Murray, K. A.; Sheth, P.; Zhang, M.; Nair, G.; Sawaya, M. R.; Shin, W. S.; Boyer, D. R.; Ye, S.; et al. Cryo-EM of Full-Length α-Synuclein Reveals Fibril Polymorphs with a Common Structural Kernel. *Nat. Commun.* **2018**, *9* (1), 3609. https://doi.org/10.1038/s41467-018-05971-2.

(19) Guerrero-Ferreira, R.; Taylor, N. M. I.; Mona, D.; Ringler, P.; Lauer, M. E.; Riek, R.; Britschgi, M.; Stahlberg, H. Cryo-EM Structure of Alpha-Synuclein Fibrils. *Elife* **2018**, *7* (e36402). https://doi.org/10.7554/eLife.36402.

(20) Li, Y.; Zhao, C.; Luo, F.; Liu, Z.; Gui, X.; Luo, Z.; Zhang, X.; Li, D.; Liu, C.; Li, X. Amyloid Fibril Structure of α-Synuclein Determined by Cryo-Electron Microscopy. *Cell Res.* **2018**, *28* (9), 897–903. https://doi.org/10.1038/s41422-018-0075-x.

(21) Arvai, A. A Program to Display X-Ray Diffraction Images. *http://www.scripps.edu/tainer/arvai/adxv.html* **2015**.

(22) Notes, I. A. Proliferation Assay MTT Protocol. *Wallert Provast Lab* **2007**, 1–2. https://doi.org/10.1007/978-1-61779-080-5_20.

(23) Holmes, B. B.; Furman, J. L.; Mahan, T. E.; Yamasaki, T. R.; Mirbaha, H.; Eades, W. C.; Belaygorod, L.; Cairns, N. J.; Holtzman, D. M.; Diamond, M. I. Proteopathic Tau Seeding Predicts Tauopathy in Vivo. *Proc. Natl. Acad. Sci.* **2014**, *111* (41), E4376–E4385. https://doi.org/10.1073/pnas.1411649111.

(24) Furman, J. L.; Holmes, B. B.; Diamond, M. I. Sensitive Detection of Proteopathic Seeding Activity with FRET Flow Cytometry. *J. Vis. Exp.* **2015**, *557*, 558-. https://doi.org/10.3791/53205.

(25) Crowther, R. A.; Daniel, S. E.; Goedert, M. Characterisation of Isolated α-Synuclein Filaments from Substantia Nigra of Parkinson's Disease Brain. *Neurosci. Lett.* **2000**, *292* (2), 128–130. https://doi.org/10.1016/S0304-3940(00)01440-3.

(26) Paravastu, A. K.; Leapman, R. D.; Yau, W.-M.; Tycko, R. Molecular Structural Basis for Polymorphism in Alzheimer's β-Amyloid Fibrils. *Proc. Natl. Acad. Sci.* **2008**, *105* (47), 18349–18354. https://doi.org/10.1073/pnas.0806270105.

(27) Kreitzer, A. C.; Malenka, R. C. Striatal Plasticity and Basal Ganglia Circuit Function. *Neuron*. 2008, pp 543–554. https://doi.org/10.1016/j.neuron.2008.11.005.

(28) Stephens, B.; Mueller, A. J.; Shering, A. F.; Hood, S. H.; Taggart, P.; Arbuthnott, G. W.; Bell, J. E.; Kilford, L.; Kingsbury, A. E.; Daniel, S. E.; et al. Evidence of a Breakdown of Corticostriatal Connections in Parkinson's Disease. *Neuroscience* **2005**, *132* (3), 741–754. https://doi.org/10.1016/j.neuroscience.2005.01.007.

(29) Congdon, E. E.; Chukwu, J. E.; Shamir, D. B.; Deng, J.; Ujla, D.; Sait, H. B. R.; Neubert, T. A.; Kong, X. P.; Sigurdsson, E. M. Tau Antibody Chimerization Alters Its Charge and Binding, Thereby Reducing Its Cellular Uptake and Efficacy. *EBioMedicine* **2019**, *42*, 157–173. https://doi.org/10.1016/j.ebiom.2019.03.033.

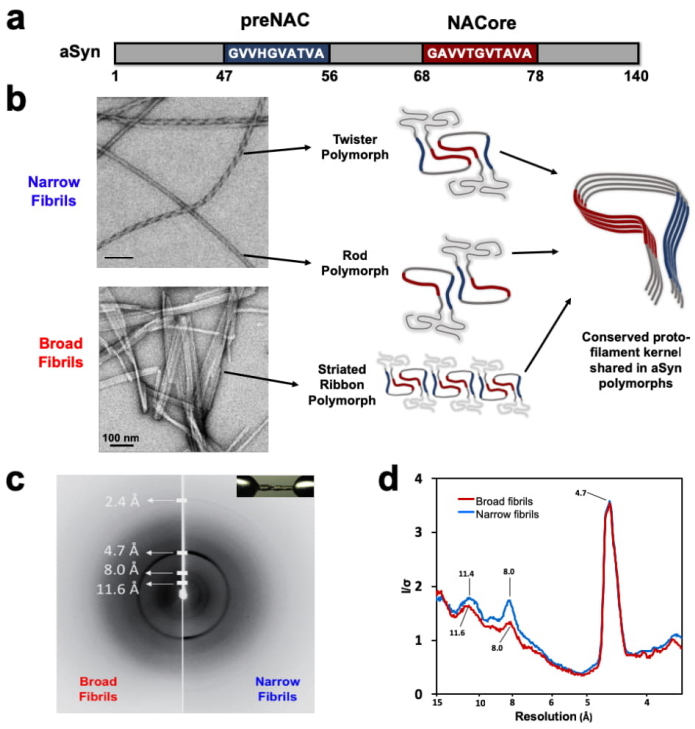

Fig. 1 Two aSyn fibril preparations share a conserved protofilament kernel

(**a**) The locations of preNAC and NACore regions on aSyn that are crucial for fibrilization and cytotoxicity. (**b**) TEM images of narrow and broad fibril preparations exhibit three different polymorphs. The rod, twister and striated ribbon polymorphs share a conserved protofilament kernel. Scale bar = 100 nm. (**c**) Fiber diffraction patterns of the broad (left panel) and narrow (right panel) fibrils exhibit peaks indicating typical cross-β structure: 4.7 Å meridional reflection and a ~10 Å equatorial reflection. Fibrils were air-dried and aligned between 2 capillary glass rods (inset). (**d**) Comparison of radial profiles of the fiber powder diffraction patterns observed for the broad fibrils (red) and narrow fibrils (blue).

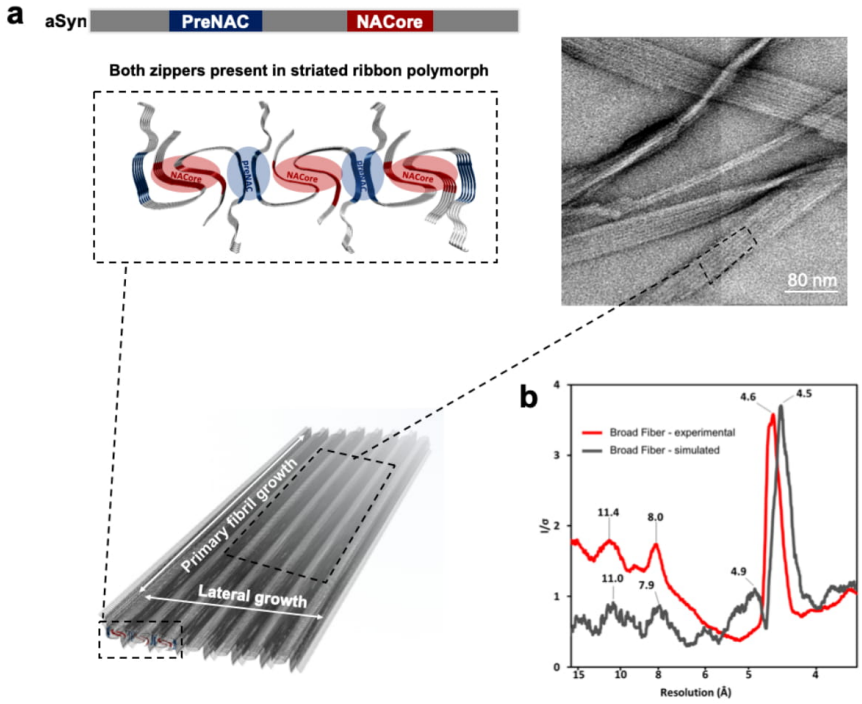

Fig. 2 aSyn fibril polymorphs are constructed around unique steric zipper interfaces between conserved protofilament kernels

(**a**) the schematic of the alternating arrangement of the preNAC (blue) and NACore (red) steric zipper interfaces in the proposed model for the striated ribbon polymorph (broad fibrils). Top and tilted views of the striated ribbon fibril model illustrate the potential for growth both along and lateral to the fiber axis. (**b**) the radial profiles of the simulated fiber powder diffraction of the model for the broad fibril samples agree with the experimental diffraction profile. The simulated profile was calculated using an input model constructed of six protofilaments with alternating zippers formed between the preNAC and NACore. A similar pattern in the diffraction profiles can be observed between the simulated and experimental data.

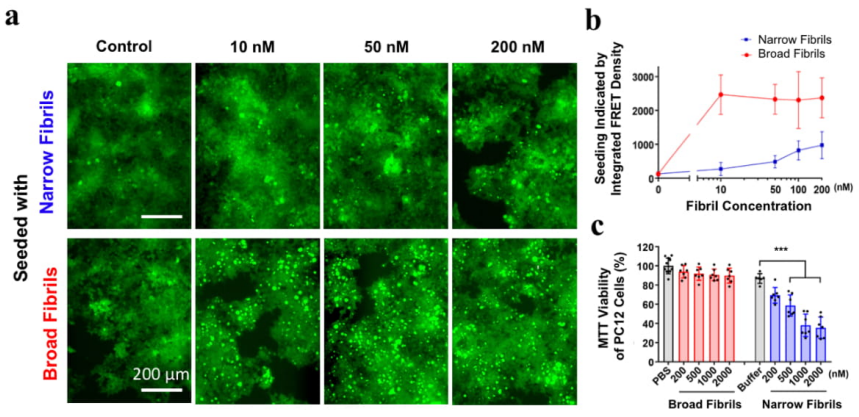

Fig. 3 Two aSyn fibril preparations have distinct *in vitro* seeding efficiency and cytotoxicity

(**a**) Fluorescence images of HEK-293T cells expressing CFP- and YFP-tagged A53T aSyn (Biosensor cells) transduced with the two aSyn fibril preparations. (**b**) FRET-based quantification of aSyn aggregation in aSyn Biosensor cells with the narrow and broad fibril preparations. (**c**) MTT-based toxicity assay in differentiated PC12 cells treated with the narrow and broad fibrils. Data are presented as mean ± SEM. Results are from 2 independent biological experiments with n = 3-5 per experiment. *** $p < 0.001$ vs. buffer used to produce the narrow fibrils.

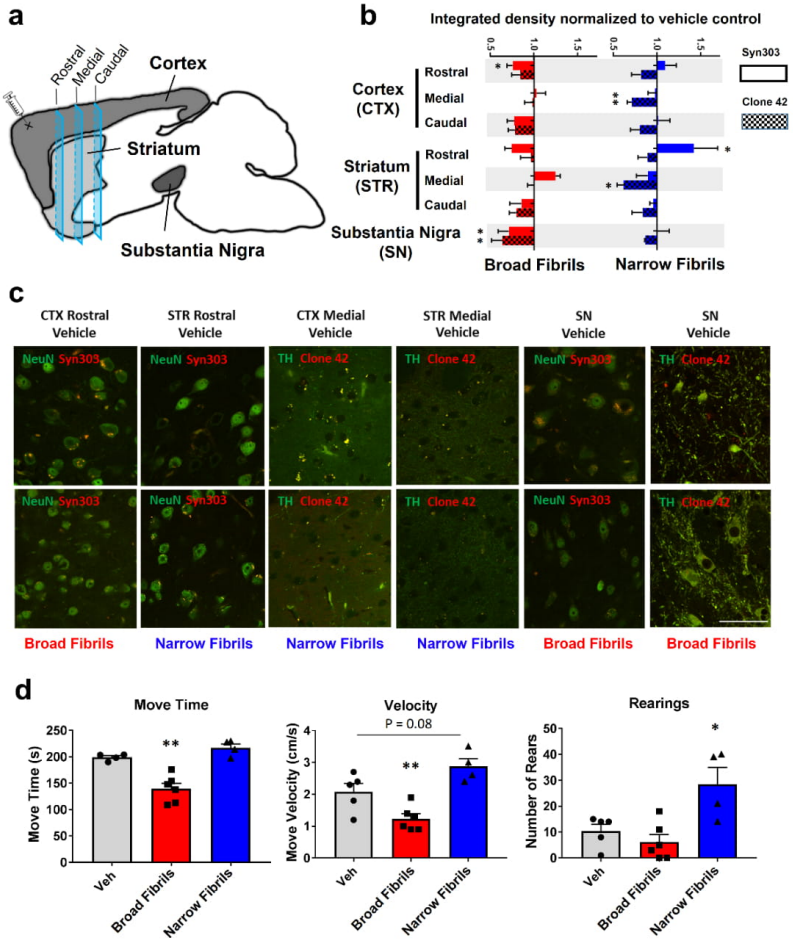

Fig. 4 Stereotaxic injections of the narrow and broad fibrils into the motor cortex induced changes in alpha-synuclein immunostaining in the brain in wild-type mice

Six-month-old mice (vehicle: n = 5, broad fibrils: n = 6, narrow fibrils: n = 4) were assessed 5 months after the fibril injections. A) Schematic illustrating the location of fibril injection and the brain regions examined by immunostaining. B) Injection of narrow or broad fibrils led to distinct changes in Syn303 and Clone 42 aSyn immunoreactivity in different brain. C) Representative confocal images illustrating significant differences in aSyn immunoreactivity following injections of the two fibril preparations. NeuN and TH (green), Syn303 and Clone 42 (red); white scale bar = 50 µm.

Supporting Information

Alternative protofilamental packing arrangements of α-synuclein fibril polymorphs contribute to seeding differences in cells and in brain

Asa Hatami[1,a,**], Binsen Li[1,a], Kevin A. Murray[2], Woo Shik Shin[1], Chris J. Elias[1], Chunni Zhu[1], Mia Broad[1], Chuanqi Sun[1], Michael R. Sawaya[2], Varghese John[1,*], Lin Jiang[1,*]

1 Department of Neurology, David Geffen School of Medicine, UCLA, Los Angeles, CA 90095, USA

2 Departments of Biological Chemistry and Chemistry & Biochemistry, UCLA, Los Angeles, CA 90095, USA

[*]Correspondence to Varghese John, Drug Discovery Lab, Department of Neurology, David Geffen School of Medicine, UCLA, Los Angeles, CA 90095, USA; Email: VJohn@mednet.ucla.edu and Lin Jiang, Department of Neurology, David Geffen School of Medicine, UCLA, Los Angeles, CA 90095, USA; Email: jianglin@ucla.edu

[**]Current affiliation: Sangamo Therapeutics, Richmond, CA 94804

[a] These authors contributed equally to this paper

Methods

Reagents and antibodies

Thiazolyl blue tetrazolium bromide for the MTT cell toxicity assay was purchased from Millipore Sigma (M2128-1G; Burlington, MA). The anti-aSyn antibody Clone 42 was purchased from BD Biosciences (cat. no. 610786; San Jose, CA) and the anti-aSyn antibody Syn303 was purchased from Biolegend (cat. no. 824301; San Diego, CA). The anti-TH antibody was purchased from Pel-Freez (cat. no. P40101-150; Rodgers, AK) and the anti-NeuN antibody was purchased from Abcam (cat. no. ab177487; Cambridge, MA).

Animals

Animal care was conducted in compliance with the United States Public Health Service Guide for the Care and Use of Laboratory Animals, and the procedures were approved by the Institutional Animal Care and Use Committee (IACUC) at the University of California, Los Angeles. Six-month-old non-transgenic mice on a C57Bl6/DBA2/BDF1 background were used for the *in vivo* studies. The animals had continuous and *ad libitum* access to standard mouse chow and water and were housed in a temperature- and humidity-controlled room maintained on a reverse 12/12 light/dark cycle, with the lights on from 2200 to 1000 hours.

Expression and Purification of Recombinant aSyn (1-140)

Full-length aSyn protein was expressed in *E. coli* (BL21-DE3 Gold strain) and purified according to a published protocol [1]. Bacterial induction started at an OD_{600} of ~0.6 with 1 mM Isopropyl β- d-1-thiogalactopyranoside (IPTG) for 6 h at 30°C. The harvested bacteria were lysed with a probe sonicator for 10 minutes in an iced water bath. After centrifugation, the soluble fraction was heated in boiling water for 10 minutes and then titrated with HCl to pH 4.5 to remove the unwanted precipitants. After adjusting to neutral pH, the protein was dialyzed overnight against Q Column loading buffer (20 mM Tris-HCl, pH 8.0). On the next day, the protein was loaded onto a HiPrep Q 16/10 column and eluted using elution buffer (20

mM Tris-HCl, 1M NaCl, pH 8.0). The eluent was concentrated using Amicon Ultra-15 centrifugal filters (Millipore Sigma) to a volume of ~5 mL. The concentrated sample was further purified by size-exclusion chromatography through a HiPrep Sephacryl S-75 HR column (GE Healthcare 17119401; Waukesha, WI) in 20 mM Tris, pH 8.0. The purified protein was dialyzed against water, concentrated to 3 mg/mL, and stored at 4°C. The concentration of the protein was determined using the Pierce™ BCA Protein Assay Kit (cat. No. 23225, Thermo Fisher Scientific; Waltham, MA) following the manufacturer's protocol.

Fibril Preparation Monitoring using ThT assay

Different fibril growth conditions were screened in the 96-well plate format. Purified aSyn (200 μM or 300 μM) was diluted in 1x phosphate-buffered saline (PBS; 10 mM PO_4^{3-}, 137 mM NaCl and 2.7 mM KCl) or 20 mM Tris buffer at various pH (5.5, 6.5, 7.5 or 8.5) in the presence or absence of commercially available crystal screening additives in the Ionic Liquid Screen (Hampton Research; Aliso Viejo, CA). The samples were thoroughly mixed with 20 μM ThT and added into each well. The 96-well plates were incubated at either room temperature or 37°C for 14-30 days. The ThT signal was monitored using a FLUOstar Omega Microplate Reader (BMG Labtech; Cary, NC) at an excitation wavelength of 440 nm and an emission wavelength of 490 nm. Selected fibril growth conditions from the ThT assay were used to grow the fibrils in the absence of ThT to be further characterized using negative-stained TEM. The broad fibrils growth condition was as follows: 300 μM aSyn, 1x PBS, 37°C. The narrow fibrils growth condition was as follows: 300 μM aSyn, 15 mM tetrabutylphosphonium bromide, room temperature. After the preparation, samples were stored in sealed 1.5-mL tubes at room temperature.

Transmission Electron Microscopy

The fibril samples (3 μL) were spotted onto freshly glow-discharged carbon-coated electron microscopy grids. After 1 minute, 6 μL uranyl acetate (2% in aqueous solution) were applied to the grid for 2 minutes and then removed using filter paper. The samples were imaged using an FEI T12 electron microscope at the Electron Imaging Center for NanoMachines at UCLA.

Fiber Diffraction

The procedure followed the protocol described in Rodriguez *et al.* [2]. To replace the solvent with water, the broad and narrow fibril samples (50 µL) were pelleted by centrifugation at 8,000 x g for 5 minutes and washed with deionized H_2O 3 times. The fibrils were resuspended in 10 µL of H_2O, placed between 2 capillary glass rods, and allowed to air-dry. On the next day, the glass rods with fibrils aligned in between were mounted on a brass pin for x-ray diffraction. Each pattern was collected using 1.54-Å x-rays produced by a Rigaku FRE+ rotating anode generator equipped with an HTC imaging plate at a distance of 150 mm for 5° rotation width. The results were analyzed using Adxv software (Arvai, 2015).

Cellular Toxicity Assay

The protocol was adopted from the Provost and Wallert laboratories [4]. PC12 cells were plated in 96-well plates at a density of 10,000 cells/well in DMEM (Dulbecco's modification of Eagle's medium; 5% fetal bovine serum [FBS], 5% heat-inactivated horse serum, 1% penicillin/streptomycin, and 150 ng/mL nerve growth factor 2.5S [Thermo Fisher Scientific]). The cells were incubated for 2 days in 5% CO_2 at 37°C. The cells were treated with different concentrations of aSyn fibrils (200 nM, 500 nM, 1000 nM, and 2000 nM). After 18 hours of incubation, 20 µL of 5 mg/mL MTT was added to every well and the plate was returned to the incubator for 3.5 hours. Following the addition of MTT, the experiment was conducted in a laminar flow hood with the lights off and the plate wrapped in aluminum foil. The media was removed with an aspirator and the remaining formazan crystals in each well were dissolved in 100 µL of 100% DMSO. Absorbance was measured at 570 nm to determine the MTT signal and at 630 nm to determine background fluorescence. The data were normalized to those from cells treated with 1% sodium dodecyl sulfate to obtain a value of 0%, and to those from cells treated with PBS to obtain a value of 100%.

Fibril Seeding Experiment in aSyn Biosensor Cells

Based on a published protocol [5], human embryonic kidney (HEK293T) FRET Biosensor cells expressing full-length aSyn containing the disease-associated A53T mutation were grown in DMEM (4 mM L-

glutamine and 25 mM D-glucose) supplemented with 10% FBS and 1% penicillin/streptomycin. Trypsin-treated HEK293T cells were harvested, seeded on flat 96-well plates at a concentration of 4×10^4 cells/well in 200 μL culture medium per well and incubated in 5% CO_2 at 37°C.

After 18 hours, aSyn fibrils were diluted with Opti-MEM™ (Life Technologies; Carlsbad CA) and sonicated in a water bath sonicator for 10 minutes. The fibril samples were then mixed with Lipofectamine™ 2000 (Thermo Fisher Scientific), incubated for 15 minutes and then added to the cells. The actual volume of Lipofectamine™ 2000 was calculated based on the dose of 1 μL per well. After 48 hours of transfection, the cells were trypsinized, transferred to a 96-well round-bottom plate and resuspended in 200 μL chilled flow cytometry buffer (HBSS, 1% FBS, and 1 mM EDTA) containing 2% paraformaldehyde. The plate was sealed with Parafilm and stored at 4°C for flow cytometry.

Flow Cytometry

The protocol was adapted from the Diamond laboratory [6]. The fluorescence signals of the cells were measured using the settings for CFP (ex. 405 nm, em. 405/50 nm filter), YFP (ex. 488 nm, em. 525/50 nm filter), and FRET (ex. 405 nm, em. 525/50 nm filter) using an LSRII Analytic Flow Cytometer (BD Biosciences). A bivariate plot of FRET vs. CFP was created to introduce a polygon gate to exclude all of the FRET-negative cells treated with only Lipofectamine™ and to include the FRET-positive cells. The integrated FRET density, which was calculated by multiplying the percentage of FRET-positive cells by the mean fluorescence intensity of the FRET-positive cells, was reported in the results.

Stereotaxic Surgery

Aseptic preparations of the aSyn broad and narrow fibrils were sonicated on the day of the surgery. The mice were anesthetized using pentobarbital (Nembutal; Akorn Inc.; Lake Forest, IL) and then mounted in a stereotaxic device (David Kopf Instruments; Tujunga, CA) equipped with a nose cone for delivery of isoflurane. The mice were placed on a heating pad connected to a rectal thermometer for the maintenance of body temperature, and the depth of anesthesia was monitored using the toe-pinch response. The skin and

muscle covering the skull were incised and a craniotomy was produced at the following coordinates relative to bregma using a dental drill (Henry Schein; Chatsworth, CA): +2.0 mm anterior, +2.0 mm to the right of midline. A Hamilton syringe was lowered to a point 2.6 mm below the dura and used to inject 5 µg of aSyn fibrils in 2.5 µl of sterile PBS. The injection was performed at a rate of 0.1 µl per minute, and the syringe was left in place for 10 minutes before slow removal. The surgical incision was sutured and the mice were returned to their home cages after complete recovery from anesthesia.

Open Field Test

Spontaneous activity was monitored for 15 minutes using an automated system (Truscan system for mice; Coulbourn Instruments; Allentown, PA) in a 25.5 cm x 25.5 cm arena. The animals were tested 1 hour after the start of the dark phase in a room dimly lit using 25-W red bulbs after 15 minutes of acclimatization. Different measures, including move distance, move time, velocity, and rearing were monitored using the automated system over three 5-minute bins for a total of 15 minutes.

Euthanasia and Tissue Preparation

The animals were deeply anesthetized using pentobarbital and transcardially perfused with 0.9% saline after disappearance of the tow-pinch response. Brains were removed, divided into hemispheres, and post-fixed in 4% paraformaldehyde for 72 hours at 4°C. The brain hemispheres were then cryoprotected in 30% sucrose at 4°C, flash-frozen in powdered dry ice, and stored at -80°C.

Immunofluorescence Staining and Quantification

All staining procedures and data collection were performed by investigators blinded to treatment. Immunofluorescence studies were performed as described previously [5,6].

Double-immunofluorescence for Clone 42 Anti-aSyn/TH and Syn303 Anti-aSyn/NeuN in SN, Striatum, and Cortex

Brain sections (SN at bregma -3.52 mm or striatal sections at bregma 1.42 mm, 0.74 mm, and 0.14 mm) were washed in 50 mM TBS (pH 7.6) and incubated in mouse IgG blocking reagent (M.O.M., Vector Laboratories; Burlingame, CA) for 1 hour. After a quick wash in TBS for 5 minutes, sections were incubated in 10% normal goat serum (NGS)/0.5% Triton X-100/TBS for 1 hour. The sections were then incubated in mouse anti-aSyn (1:250, BD Biosciences Clone 42) and rabbit anti-TH antibody (1:1,000, Pel-Freeze) or Syn303 (1:1,000, BioLegend) and rabbit anti-NeuN (1:1,000, Abcam) antibody in 5% NGS at 4°C overnight. After washing, sections were incubated in Alexa 647 goat anti-mouse IgG (1:500; Invitrogen; Carlsbad, CA) and Cy3 goat anti-rabbit IgG (1:500; Jackson Immunoresearch; West Grove, PA) in 5% NGS for 2 hours at room temperature. After washing, sections were mounted in tap water on plain glass slides.

Quantification of Fluorescence Intensity in SN, Striatum, and Cortex

For the quantification of aSyn and TH fluorescent immunolabeling in different brain regions, images of immunofluorescence-labeled sections were acquired using an Agilent (Santa Clara, CA) microarray scanner equipped with a krypton/argon laser (647 nm) at 10 μm resolution with the photomultiplier tube set at 5% for aSyn and 10% for TH. Immunofluorescence intensity was measured using ImageJ in the appropriate region of interest (ROI) by subtracting the background fluorescence signal in the same ROI. TH staining was quantified in the SN pars compacta, SN pars reticulata, and the striatum (rostral, medial, and caudal levels). Clone 42- and Syn303-reactive aSyn was quantified in the whole SN, striatum (at 3 levels), and cortex overlying the striatum (at 3 levels).

Statistical analysis

All statistical analyses were performed in SigmaPlot version 13.0 (Systat Software, Inc.; San Jose, CA). The Grubbs test was used to exclude outliers prior to group comparisons. One-way ANOVAs were used to assess differences between the fibril-treated and vehicle-treated cells in the *in vitro* cytotoxicity assay. Student's t-tests between each fibril-treated group and the vehicle-treated group were used to assess the

effects of the fibril injections on behavior in the open field and on the histological measures. P-values <0.05 were considered statistically significant.

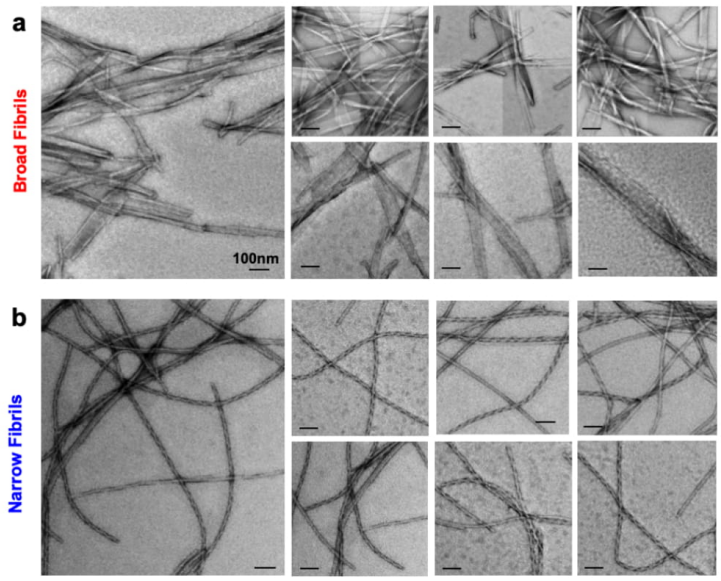

Figure S1 Negative-stained TEM images of the broad (**a**) and narrow fibrils (**b**). The striated ribbon polymorph was observed in the broad fibrils preparation and the rod and twister polymorphs grew in the narrow fibrils preparation. Scale bar: 100 nm.

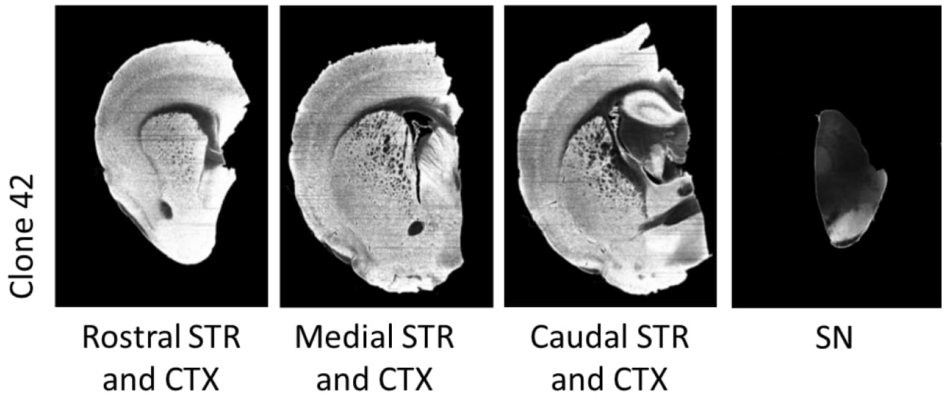

Figure S2 Representative microarray images of studied brain sections. Rostral, medial, and caudal coronal brain sections containing the striatum and the cortex on the ipsilateral side, as well as the ipsilateral substantia nigra were characterized. STR, striatum; CTX, cortex; SN, substantia nigra.

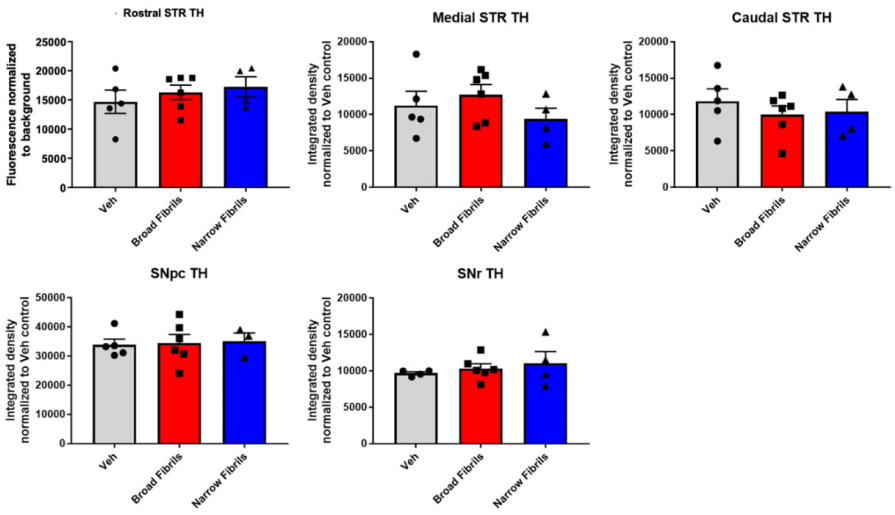

Figure S3 TH immunostaining revealed no significant changes in TH-positive dopaminergic terminals in the striatum or in TH-positive cells in the SN. The effects of the broad and narrow fibrils on TH-positive dopaminergic cell bodies in the substantia nigra and TH-positive terminals in the striatum were assessed. The vehicle control animals received an injection of sterile 0.9% saline at the same volume used for the fibril injections. We observed no significant changes in TH staining in any of the regions tested. STR, striatum; SNpc, substantia nigra pars compacta; SNr, substantia nigra pars reticulata.

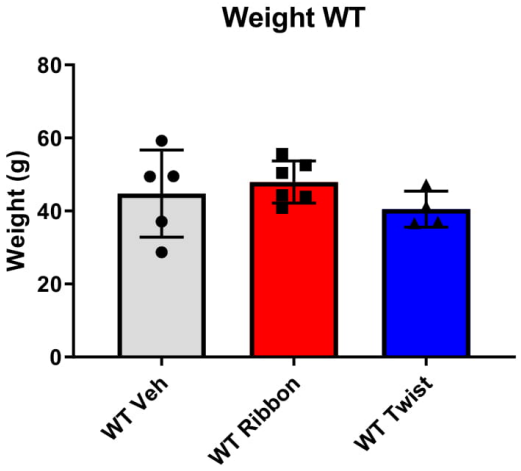

Figure S4 Mouse body weights revealed no gross health effects associated with the fibril injections. There were no significant differences in the body weights of the mice at the time of euthanasia, indicating that the fibril injections led to no gross health effects.

References

(1) Li, B.; Ge, P.; Murray, K. A.; Sheth, P.; Zhang, M.; Nair, G.; Sawaya, M. R.; Shin, W. S.; Boyer, D. R.; Ye, S.; et al. Cryo-EM of Full-Length α-Synuclein Reveals Fibril Polymorphs with a Common Structural Kernel. *Nat. Commun.* **2018**, *9* (1), 3609. https://doi.org/10.1038/s41467-018-05971-2.

(2) Rodriguez, J. A.; Ivanova, M. I.; Sawaya, M. R.; Cascio, D.; Reyes, F. E.; Shi, D.; Sangwan, S.; Guenther, E. L.; Johnson, L. M.; Zhang, M.; et al. Structure of the Toxic Core of α-Synuclein from Invisible Crystals. *Nature* **2015**, *525* (7570), 486–490. https://doi.org/10.1038/nature15368.

(3) Arvai, A. A Program to Display X-Ray Diffraction Images. *http://www.scripps.edu/tainer/arvai/adxv.html* **2015**.

(4) Notes, I. A. Proliferation Assay MTT Protocol. *Wallert Provast Lab* **2007**, 1–2. https://doi.org/10.1007/978-1-61779-080-5_20.

(5) Holmes, B. B.; Furman, J. L.; Mahan, T. E.; Yamasaki, T. R.; Mirbaha, H.; Eades, W. C.; Belaygorod, L.; Cairns, N. J.; Holtzman, D. M.; Diamond, M. I. Proteopathic Tau Seeding Predicts Tauopathy in Vivo. *Proc. Natl. Acad. Sci.* **2014**, *111* (41), E4376–E4385. https://doi.org/10.1073/pnas.1411649111.

(6) Furman, J. L.; Holmes, B. B.; Diamond, M. I. Sensitive Detection of Proteopathic Seeding Activity with FRET Flow Cytometry. *J. Vis. Exp.* **2015**, *557*, 558-. https://doi.org/10.3791/53205.

CHAPTER 3

ARTICLES
https://doi.org/10.1038/s41594-019-0322-y

nature structural & molecular biology

Structures of fibrils formed by α-synuclein hereditary disease mutant H50Q reveal new polymorphs

David R. Boyer[1,3], Binsen Li[2,3], Chuanqi Sun[2], Weijia Fan[2], Michael R. Sawaya[1], Lin Jiang[2*] and David S. Eisenberg[1*]

Deposits of amyloid fibrils of α-synuclein are the histological hallmarks of Parkinson's disease, dementia with Lewy bodies and multiple system atrophy, with hereditary mutations in α-synuclein linked to the first two of these conditions. Seeing the changes to the structures of amyloid fibrils bearing these mutations may help to understand these diseases. To this end, we determined the cryo-EM structures of α-synuclein fibrils containing the H50Q hereditary mutation. We find that the H50Q mutation results in two previously unobserved polymorphs of α-synuclein: narrow and wide fibrils, formed from either one or two protofilaments, respectively. These structures recapitulate conserved features of the wild-type fold but reveal new structural elements, including a previously unobserved hydrogen-bond network and surprising new protofilament arrangements. The structures of the H50Q polymorphs help to rationalize the faster aggregation kinetics, higher seeding capacity in biosensor cells and greater cytotoxicity that we observe for H50Q compared to wild-type α-synuclein.

Several lines of evidence suggest that aggregation of α-synuclein (α-syn) into amyloid fibrils underlies the group of diseases termed synucleinopathies—Parkinson's disease (PD), Lewy body dementia and multiple systems atrophy. (1) α-Syn fibrils are found in the hallmark lesions of PD and Lewy body dementia (Lewy bodies), as well as in the hallmark glial and neuronal lesions in multiple systems atrophy[1,2]. (2) Hereditary mutations in α-syn have been linked to PD and Lewy body dementia[3]. (3) Dominantly inherited duplications and triplications of the chromosomal region that contains wild-type *SNCA*—the gene that encodes α-syn—are sufficient to cause PD (refs. [4–6]). (4) Recombinantly assembled α-syn fibrils show cross-β structure and their injection into the brains of wild-type mice induced PD-like Lewy body and Lewy neurite formation, as well as cell-to-cell spreading and motor deficits reminiscent of PD[7,8].

Advances in solid-state NMR and cryo-EM have greatly increased our knowledge of the structure of full-length amyloid proteins, allowing us to examine interactions beyond the local views provided by crystallographic methods[9–13]. Therefore, we previously used cryo-EM to determine the structures of wild-type full-length α-syn fibrils (Fig. 1a,b, left). These structures reveal two distinct polymorphs—termed the rod and twister[14]. Both fibrils are wound from two identical protofilaments related by an approximate 2_1 fibril axis. The protofilaments that form the rod and twister polymorphs are distinct: the rod protofilaments contain ordered residues 38–97 whereas the twister protofilaments contain ordered residues 43–83. Both polymorphs share a similar structurally conserved β-arch formed by residues 50–77. However, the protofilament interfaces between the two polymorphs differ: in the rod polymorph, residues 50–57 from the preNAC region form the interface of the two protofilaments, whereas, in the twister polymorph, residues 66–78 from the NACore form the interface.

Hereditary mutations offer understanding of the link between protein structure and disease. H50Q is one such mutation that was discovered independently in two individuals with PD, with one patient having a known familial history of parkinsonism and dementia[15,16]. The H50Q mutation enhances α-syn aggregation in vitro by reducing the solubility of the monomer, decreasing the lag time of fibril formation and increasing the amount of fibrils formed[17,18]. Additionally, H50Q has been shown to be secreted at higher levels from SH-SY5Y cells and to be more cytotoxic to primary hippocampal neurons than wild-type α-syn[19]. Taken together these data suggest that patients harboring the H50Q mutation may develop fibrils more easily and that these fibrils may have different underlying structures than wild-type fibrils.

The structure of the wild-type rod polymorph suggests that the H50Q mutation may alter key contacts at the protofilament interface[14]. In this structure, two pairs of H50–E57 residues interact on opposing protofilaments, stabilizing the protofilament interface through charge–charge interactions. The mutation to the uncharged, polar glutamine may therefore disrupt the rod polymorph protofilament interface, leading to different polymorphs of α-syn, potentially explaining the different observed properties of H50Q versus wild-type α-syn[17,18]. To examine the exact effect of the H50Q mutation on the structure of α-syn fibrils, we sought to determine the atomic structures of H50Q α-syn fibrils using cryo-EM and to compare aggregation kinetics, stability, seeding capacity and cytotoxicity to wild-type α-syn.

Results

Cryo-EM structure and architecture of H50Q α-syn fibrils. To pursue cryo-EM structure determination, we expressed and purified recombinant full-length α-syn containing the H50Q hereditary mutation and subsequently grew fibrils under the same conditions

[1]Department of Chemistry and Biochemistry and Biological Chemistry, UCLA-DOE Institute, Molecular Biology Institute and Howard Hughes Medical Institute, UCLA, Los Angeles, CA, USA. [2]Department of Neurology, David Geffen School of Medicine, Molecular Biology Institute, UCLA, Los Angeles, CA, USA. [3]These authors contributed equally: David R. Boyer, Binsen Li. *e-mail: jianglin@ucla.edu; david@mbi.ucla.edu

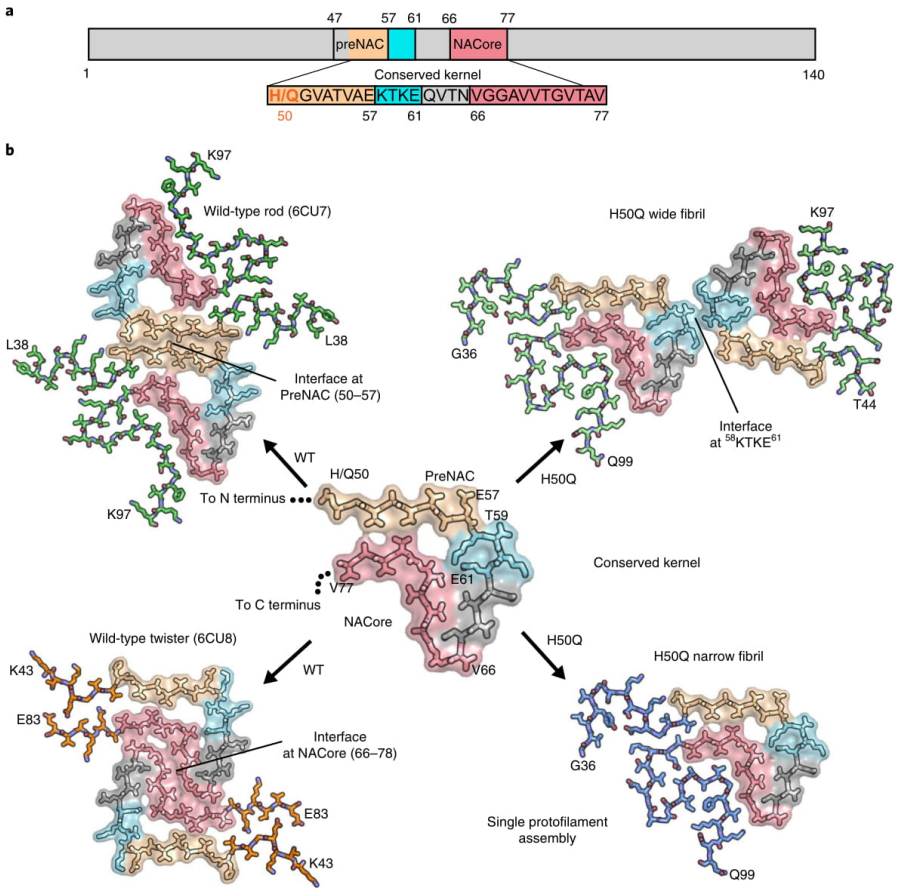

Fig. 1 | Comparison of wild-type and H50Q polymorphs. a, Primary structure schematic highlighting residues of the conserved kernel (50–77) that form protofilament interfaces in α-syn polymorphs. **b**, A conserved kernel is used to assemble wild-type (left) and H50Q (right) α-syn polymorphs in at least four different ways.

as those used for cryo-EM studies of wild-type α-syn (see Methods). After obtaining optimal cryo grid conditions and subsequent high-resolution cryo-EM data collection and processing, we determined the near-atomic structures of two polymorphs, which we term narrow and wide fibrils, to resolutions of 3.3 and 3.6 Å, respectively (Figs. 1b and 2a–d, Extended Data Figs. 1a,b and 2a and Table 1).

Both the narrow and wide fibrils have pitches of ~900 Å, as measured from the cross-over distances observed in electron micrographs as well as 2D classifications of box sizes containing helical segments that encompass an entire helical pitch (Extended Data Fig. 2b,c; see Methods). Narrow fibrils have a width that varies from 55 to 66 Å; wide fibrils have a width that varies from 67 to 116 Å (Fig. 2b and Extended Data Fig. 1a). The narrow fibril is wound from a single protofilament, which we designate protofilament A, while the wide fibril is wound from two slightly different protofilaments, both protofilament A and a second protofilament, which we term protofilament B (Fig. 2c,d). Both narrow and wide fibril reconstructions show identical densities flanking protofilament A, which we term islands 1 and 2 (Supplementary Note 1 and Extended Data Fig. 3). Narrow fibrils are roughly five times more abundant than wide fibrils. Protofilament A contains ordered residues from G36 to Q99, while protofilament B contains ordered residues T44 to K97 (Fig. 2a,c,d).

The protein chains in the ordered cores of both protofilaments fold essentially within a two-dimensional layer (Fig. 2b–d), with stretches of straight β-strand regions interrupted by sharp turns (Fig. 3a,b). The fibrils are formed by the chains within the two-dimensional layers stacking on one another along the fibril axis every 4.8 Å, forming β-sheets that extend for hundreds of nanometers (Fig. 2b).

Differences between protofilaments A and B. To define the differences in protofilaments A and B observed in the two polymorphs, we aligned protofilament A with protofilament B (Fig. 3b). The alignment reveals that residues 47–97 adopt nearly identical conformations in both protofilaments A and B; however, protofilament A has an ordered β-arch formed by residues 36–46, whereas protofilament B becomes disordered after T44 (Fig. 3b,c). The β-arch in protofilament A features an extensive hydrogen-bond network among Y39, T44 and E46 that is not observed in any α-syn structures

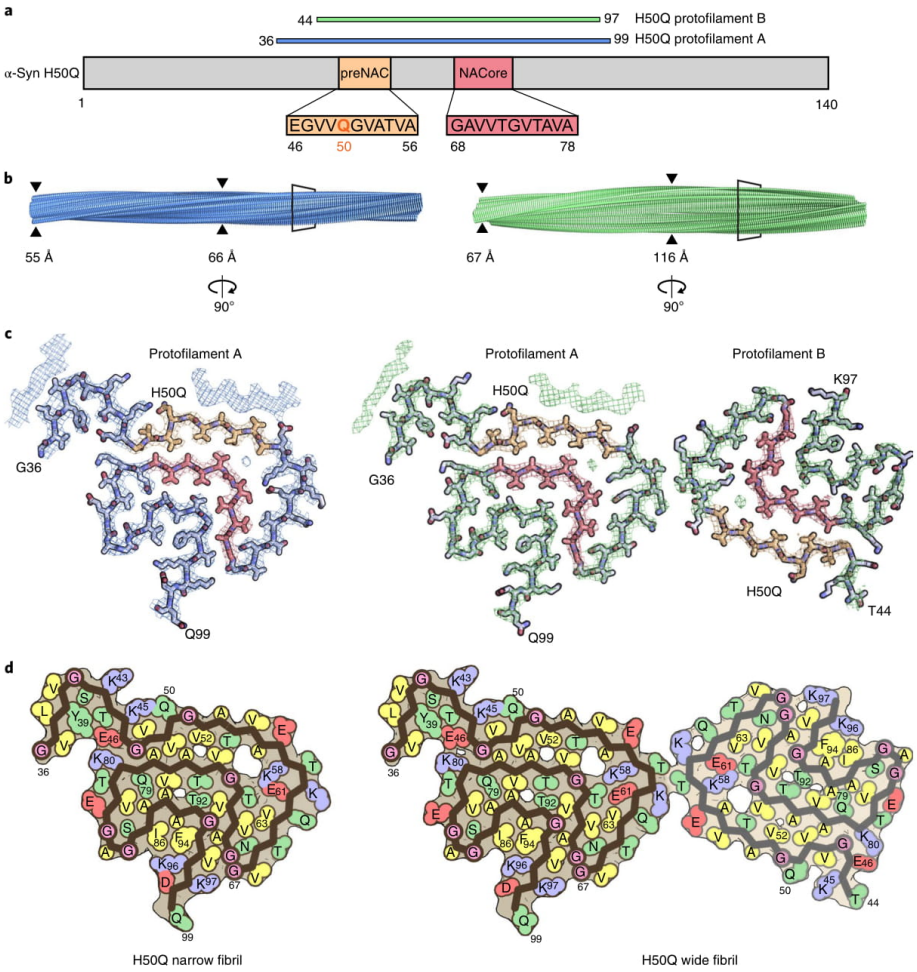

Fig. 2 | Cryo-EM structures of H50Q polymorphs. a, Schematic of α-syn primary structure demonstrating location of the ordered core of H50Q protofilaments A and B, preNAC and NACore and H50Q hereditary mutation. **b**, View perpendicular to the fibril axes of narrow and wide fibril cryo-EM reconstructions with the minimum and maximum widths of the fibrils labeled. **c**, View parallel to the fibril axes of sections of narrow and wide fibrils revealing one layer of each fibril. Narrow fibrils are composed of one protofilament, designated protofilament A. Wide fibrils are composed of two protofilaments: protofilament A and a less well-ordered chain designated protofilament B. Protofilament A is nearly identical in both fibril species, while protofilament B differs from protofilament A and is only found in the wide fibril species. **d**, Schematic representation of fibril structures with amino acid side chains colored as follows: hydrophobic (yellow), negatively charged (red), positively charged (blue), polar, uncharged (green) and glycine (pink).

determined so far (Fig. 3b,c). In addition, we note that in protofilament A, Q50 is hydrogen bonded to K45, whereas in protofilament B, K45 and Q50 are not hydrogen bonded and appear to be solvent facing (Fig. 3b,c). This alternative arrangement of K45 and Q50 may explain why protofilament A forms an ordered β-arch while protofilament B does not. This suggests that the conformation of K45 and Q50 can act as a switch whereby, as they become hydrogen bonded, the amino (N)-terminal residues 36–44 become ordered, forming the Y39–T44–E46 hydrogen bond triad. We also note that protofilament B maintains the E46–K80 hydrogen bond observed in wild-type structures, while participation of E46 in a hydrogen bond with T44 in protofilament A differs from that in wild-type structures. Instead, K80 now hydrogen bonds with T81 in protofilament A (Fig. 3b,c). The differences observed here highlight the impact that hydrogen-bonding arrangements can have on fibril structure and explain the atomic basis for the asymmetry of the two protofilaments in the wide fibril polymorph. Indeed, previous studies on wild-type α-syn fibril structures have revealed fibrils composed of asymmetric protofilaments whose asymmetry could be explained by the types of alternative hydrogen-bond patterns that we observe here[20].

Cavities in α-syn fibril structures. We note that all α-syn fibril structures determined so far display a similar cavity at the center

Table 1 | Cryo-EM data collection, refinement and validation statistics

	H50Q narrow fibril (EMD-20328, PDB 6PEO)	H50Q wide fibril (EMD-20331, PDB 6PES)
Data collection and processing		
Magnification	130,000	130,000
Voltage (kV)	300	300
Camera	K2 Summit (Quantum LS)	K2 Summit (Quantum LS)
Frame exposure time (s)	0.2	0.2
Movie frames (no.)	30	30
Electron exposure (e^-/Å^2)	36	36
Box size (pixel)	288	224
Inter-box distance (Å)	28.8	22.4
Micrographs collected (no.)	3,577	3,577
Segments extracted (no.)	1,183,284	137,395
Segments after Class2D (no.)	510,477	NA[a]
Segments after Class3D (no.)	30,133	28,016
Map resolution (Å)	3.3	3.6
FSC threshold	0.143	0.143
Refinement		
Initial model used	De novo	De novo
Model resolution (Å)	3.2	3.5
FSC threshold	0.5	0.5
Model resolution range (Å)	200–3.3	200–3.6
Map sharpening *B* factor (Å^2)	−148	−207
Model composition		
Nonhydrogen atoms	2,205	4,040
Protein residues	320	590
Ligands	NA	NA
B factors (Å^2)		
Protein	NA	NA
Ligand	NA	NA
R.m.s. deviations		
Bond lengths (Å)	0.003	0.009
Bond angles (°)	0.5	0.7
Validation		
MolProbity score	2.09	2.18
Clashscore	10.62	12.28
Poor rotamers (%)	0	0
Ramachandran plot		
Favored (%)	90.3	87.7
Allowed (%)	9.7	12.3
Disallowed (%)	0	0

[a]Number of segments after Class2D not available (NA) for the wide fibril as only 3D classification was performed.

of the β-arch, surrounded by residues T54, A56, K58, G73 and V74 (Figs. 1b and 2c and Extended Data Fig. 4a,b). However, in contrast to our previously published wild-type structures, K58 now faces inward towards the cavity, instead of outward towards the solvent, while T59 now flips away from the cavity (Extended Data Fig. 4a). This inversion is possible because lysine and threonine have both hydrophobic and hydrophilic character, allowing them to be favorably positioned either facing the solvent or the cavity. Indeed, energetic calculations demonstrate that K58 and T59 can have a positive stabilization energy in both cases (Extended Data Fig. 5b,c).

Presumably the β-arch cavity is filled with disordered solvent that is not defined by cryo-EM or previously used solid-state NMR averaging methods. However, we note here that in our narrow and wide fibril polymorphs we visualize additional density in the cavity that is not accounted for by protein side chains (Fig. 2c and Extended Data Fig. 4b). We wonder whether this density arises from noise, or a back-projection artifact, but it is observed in the same location independently in three protofilaments (protofilament A from the narrow fibril and protofilaments A and B from the wide fibril) leading us to believe that it may come from a solvent molecule (Extended Data Fig. 4b). Since our fibril growth conditions contain only water and tetrabutylphosphonium bromide, whose long aliphatic groups make it too large to fit into the tight cavity, we examined if the density could come from a water molecule and if any of the surrounding residues could serve as hydrogen-bond partners. We observe that the γ-hydroxyl of T54, the ε-amino of K58 and the carbonyl oxygen of G73 are the only potential hydrogen-bonding partners for the putative water molecule (Extended Data Fig. 4b). In addition, there are several methyl groups from V74 and A56 that are proximal to the putative solvent molecule (Extended Data Fig. 4b). The distance between the density and potential hydrogen partners ranges from 4.2 to 5.4 Å, which is longer than usual for hydrogen bonds (Extended Data Fig. 4b). However, given that there are three hydrogen-bond partners, perhaps the density visualized in the reconstruction is an average of positions occupied by water molecules. Nonetheless, given the resolution of our maps we cannot unambiguously identify the molecule(s) occupying the density in the center of the cavity.

Wide fibril protofilament interface. The wide fibril contains a novel protofilament interface formed by residues ^{58}KTKE^{61} not previously seen in wild-type α-syn structures[14]. Residues ^{58}KTKE^{61} are located at a sharp turn in both protofilaments A and B, and, consequently, the interface between protofilaments is remarkably small (Extended Data Fig. 6a). Consistent with the minimal size of the interface, the shape complementarity of 0.57 and buried surface area of 50 Å^2 of the wide fibril interface are low compared to the more extensive preNAC and NACore interfaces seen in our previous wild-type structures (Extended Data Fig. 6b)[14]. Indeed, the Cγ atom of T59 from each protofilament is the only atom to interact across the protofilament interface (Extended Data Fig. 6b), making this interface the smallest fibril protofilament interface observed to date.

We wondered why the H50Q polymorphs do not utilize the extensive preNAC or NACore protofilament interfaces found in the wild-type rod and twister polymorphs, respectively. Our structures reveal that, unlike the wild-type twister polymorph, the NACore is buried within the fibril core and is inaccessible as a protofilament interface (Fig. 2c). However, the preNAC region is more accessible as a potential protofilament interface in both of the H50Q polymorphs (Fig. 2c). To examine why the preNAC region does not form a protofilament interface, we first compared the preNAC protofilament interface in the wild-type rod polymorph with the same region in the H50Q narrow fibril (Extended Data Fig. 7a,b). We noticed that in the wild-type rod polymorph H50 on one protofilament interacts with E57 on the opposite protofilament, possibly through a charge–charge interaction (Extended Data Fig. 7b). The mutation to a polar, uncharged glutamine leads to a loss of interaction with E57 and instead Q50 forms an intramolecular hydrogen bond with K45 in H50Q protofilament A, thereby producing a single protofilament

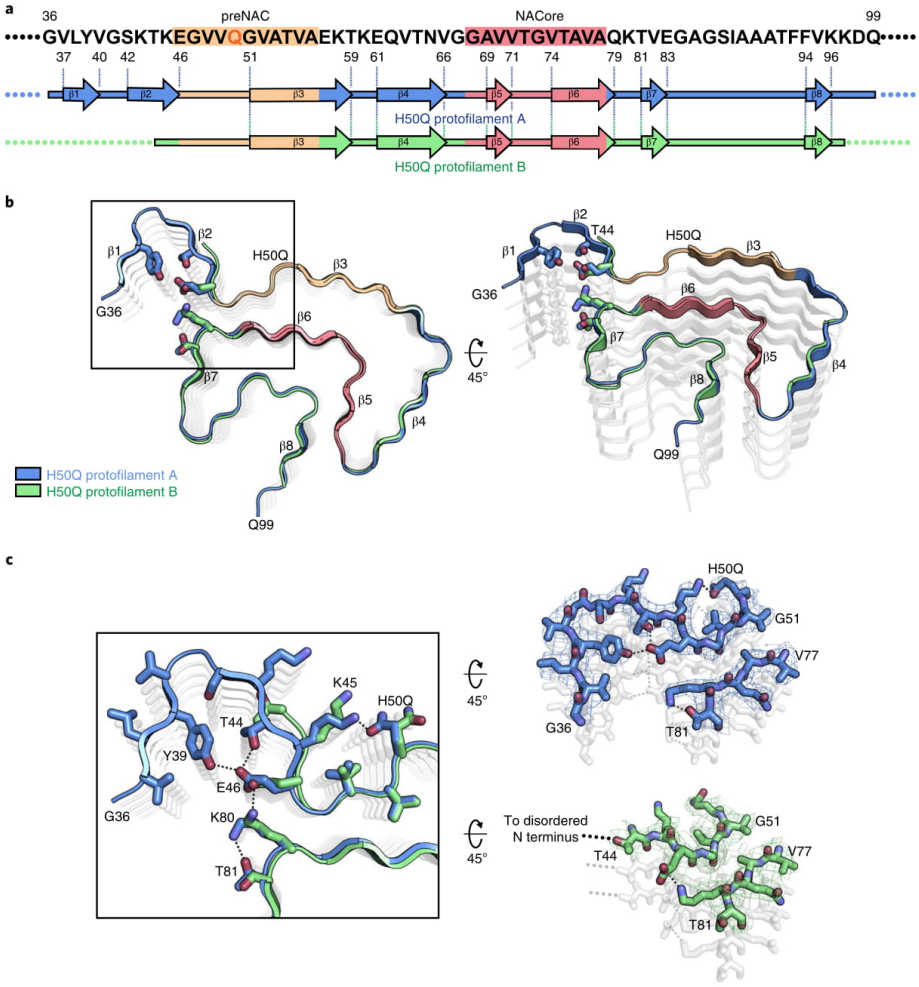

Fig. 3 | Comparison of protofilaments A and B. a, Schematic of primary and secondary structure of the fibril core of H50Q protofilaments A and B. Arrows indicate regions of protofilaments A and B that adopt β-strand conformations. **b**, Structural alignment of H50Q protofilaments A and B. **c**, Alignment of protofilaments A and B reveals that protofilament A has a β-arch formed by residues 36–46, whereas protofilament B is disordered before residue 44. Additionally, in protofilament A, H50Q hydrogen bonds with K45, while in protofilament B, H50Q and K45 adopt different conformations and do not hydrogen bond. In protofilament A, E46 participates in the Y39–T44–E46 hydrogen-bond triad and K80 hydrogen bonds with T81, while in protofilament B E46 hydrogen bonds with K80 as in the wild-type rod polymorphs.

assembly (Extended Data Fig. 7a). Further, speculative models where additional protofilaments are docked at the preNAC region in either protofilament A or B show severe steric clashes occurring, further supporting the idea that the H50Q mutation disallows assembly of protofilaments at the preNAC (Supplementary Note 2 and Extended Data Fig. 7c,d).

Energetic and biochemical analysis of H50Q fibrils. We next wondered if the structural differences that we observe in the H50Q versus wild-type fibrils affect their stabilities. To examine this, we first calculated modified atomic solvation energies for the H50Q mutant structures and wild-type α-syn structures (see Supplementary Note 3 for differences in stabilization energies for some residues in protofilaments A and B in the wide fibril). We find that both wild-type and H50Q fibrils are stabilized by energies comparable to a selection of known irreversible fibrils, including tau-paired helical filament structures from Alzheimer's disease[21], serum amyloid A fibrils from systemic amyloidosis[22] and TDP-43 SegA-sym fibrils[23], and significantly larger than the stabilization energies of the reversible FUS fibrils[24] (Fig. 4a and Table 2). To confirm this, we performed stability assays to measure the resistance of fibrils to heat and SDS, and we found that both wild type and H50Q show a similar resistance to denaturation, consistent with our energetic calculations (Fig. 4c). This is also consistent with the idea that both wild-type and H50Q

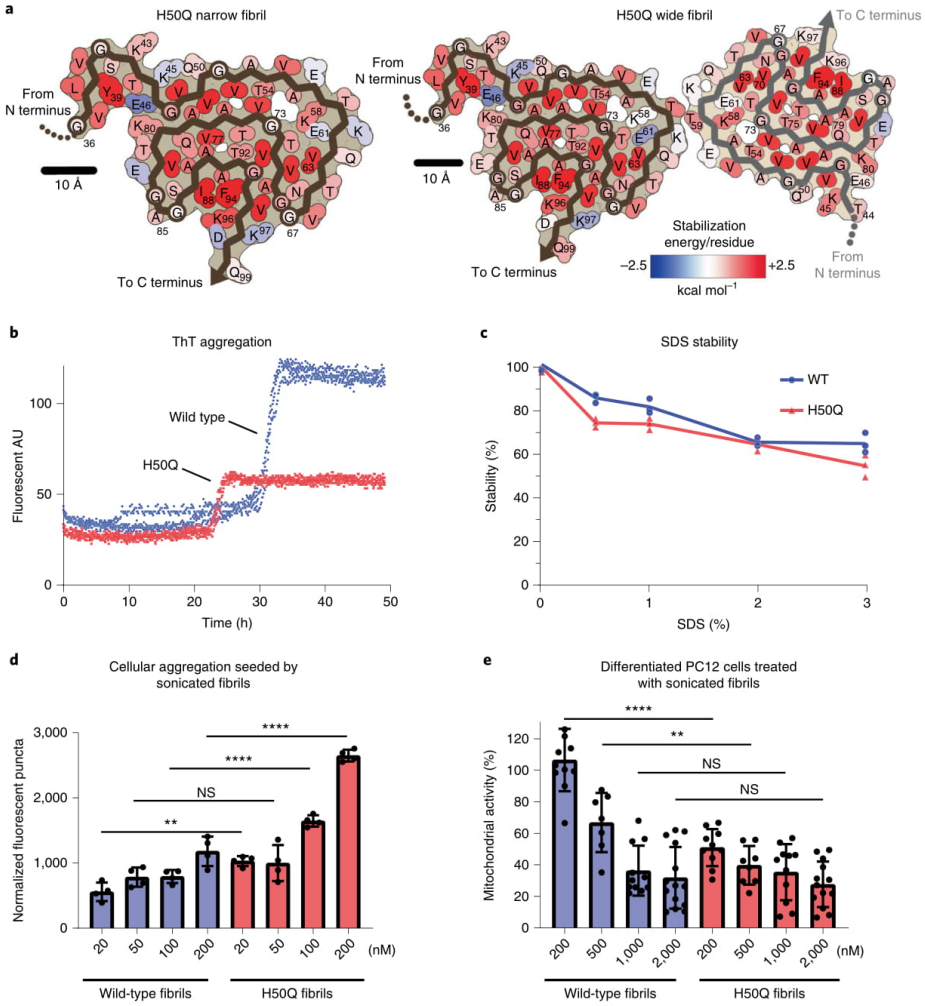

Fig. 4 | Solvation energy maps and biochemical characterization of H50Q and wild-type α-syn. a, Solvation energy maps of H50Q narrow and wide fibrils. The stabilizing residues are red; the destabilizing residues are blue. **b**, ThT assay measuring kinetics of H50Q and wild-type α-syn aggregation. Data from three independent replicates for each sample are shown for each time point. Wild-type aggregation plateaus at 30 h whereas H50Q aggregates faster and plateaus at 23 h. **c**, Stability assay of H50Q and wild-type α-syn. Fibrils were brought to the indicated concentration of SDS and heated at 70 °C for 15 min before ThT signal was measured. Both H50Q and wild-type fibrils are irreversible. **d**, Cell seeding assay of H50Q and wild-type α-syn performed in HEK293T α-syn-A53T-YFP biosensor cells. Sonicated fibrils were transfected into biosensor cells using Lipofectamine. After 48 h, the number of fluorescent puncta indicating aggregated endogenous α-syn-A53T-YFP was counted (see Methods). H50Q fibrils have a higher seeding capacity than wild-type fibrils. Error bars represent standard deviation of four independent measurements. **e**, MTT toxicity assay of H50Q and wild-type α-syn performed in differentiated PC12 cells. H50Q and wild-type α-syn fibrils were introduced to culture medium and after incubation, cell mitochondrial activity was measured via MTT assay. H50Q requires less fibrils than wild type to significantly disrupt mitochondrial activity. Error bars represent standard deviation of a minimum of 7 and a maximum of 14 independent measurements. $^{****}P \leq 0.0001$. $^{**}P \leq 0.01$. NS, not significant $P > 0.05$. *P* values were calculated using an unpaired, two-tailed *t*-test with a 95% CI.

α-syn are associated with pathogenic, irreversible fibrils formed in the synucleinopathies.

We next characterized the kinetics of H50Q and wild-type fibril growth and found that H50Q aggregation has a shorter lag phase and therefore forms fibrils more rapidly than wild-type fibrils, consistent with other studies (Fig. 4c)[18,19,25]. We note that although H50Q fibrils have a lower max thioflavin T (ThT) signal, this is likely explained by different fibril polymorphs having differential ThT binding and not as being due to overall less fibril formation. We also find that H50Q fibrils have higher seeding capacity in HEK293T α-syn-A53T-YFP

Table 2 | Comparative solvation energy calculations

Fibril structure	Atomic solvation standard free energy of stabilization (kcal mol^{-1})		
	Per layer	Per chain	Per residue
H50Q narrow fibril	58	58 (pf A)	0.90 (pf A)
H50Q wide fibril	114	58 (pf A)	0.90 (pf A)
		54 (pf B)	1.00 (pf B)
WT rod cryo-EM (PDB 6CU7)	112	56	0.93
WT twister cryo-EM (PDB 6CU8)	66	33	0.80
WT solid-state NMR (PDB 2N0A)	58	58	0.91
WT rod (PDB 6H6B)	101	51	0.86
WT rod (PDB 6A6B)	122	61	0.96
Tau PHF (PDB 530L)	128	64	0.88
Tau pick's (PDB 6GX5)	98	98	1.00
TDP-43 SegA-sym (PDB 6N37)	73	37	1.00
Serum amyloid A (PDB 6MST)	116	58	1.07
FUS (PDB 5W3N)	41	41	0.66

pf, protofilament; WT, wild type.

biosensor cells[26] and significantly higher cytotoxicity to differentiated neuron-like rat pheochromocytoma (PC12), as measured by a reduction of mitochondrial activity and cell membrane integrity (Fig. 4d,e and Extended Data Fig. 8). These results are similar to other studies demonstrating the enhanced pathogenic properties of H50Q versus wild-type α-syn[17–19,25], and overall our findings support the idea that the differences in the structures of the H50Q fibrils compared to wild-type fibrils result in higher pathogenicity.

Discussion

The structures of α-syn fibrils determined here demonstrate that the H50Q mutation results in two new polymorphs, which we term narrow and wide fibrils. Structural alignments of wild-type and H50Q polymorphs reveal that residues 50–77 in all structures adopt a largely similar β-arch-like fold, which we previously termed the conserved kernel (Extended Data Fig. 9)[14]. However, different sequence segments of the conserved kernel assemble protofilaments into distinct fibril polymorphs (Fig. 1a,b). The wild-type rod polymorph utilizes residues from the preNAC region[14,27,28], the wild-type twister polymorph utilizes residues from the NACore[14] and the H50Q wide fibril utilizes residues ^{58}KTKE^{61} to assemble protofilaments, while the H50Q narrow fibril forms a single protofilament structure (Fig. 1a,b). Therefore, the structures determined to date of wild-type and mutant α-syn fibrils demonstrate that the conserved kernel formed by residues 50–77 acts a modular building block to assemble protofilaments into distinct polymorphs in at least four different ways.

In all seven α-syn fibril structures, the conserved kernel features a cavity, possibly a solvent channel surrounded by T54, A56, K58, G73 and V74 (Figs. 1b and 2c and Extended Data Fig. 4b)[14,27–29]. However, the H50Q polymorphs determined here are, so far, the only α-syn fibril structures to resolve density in this cavity. A hydrophilic cavity is also observed in the human serum amyloid A cryo-EM structure and two structures of immunoglobulin light chain fibrils[22,30,31]. Therefore, full-length amyloid fibrils share the property of crystal structures of amyloid segments where the majority of the protein packs in a manner excluding water, while some water molecules can be seen hydrogen bonding with the backbone or polar side chains[32]. Recent structures of tau fibrils extracted from the brains of patients with chronic traumatic encephalopathy suggest that a hydrophobic molecule may occupy a hydrophobic cavity present in the fibril core[33]. This is also similar to crystal structures of amyloid segments where molecules such as polyethylene glycol can occupy cavities in the crystal packing[34].

The structures of H50Q polymorphs help to explain the differences in aggregation kinetics, seeding capacity and cytotoxicity between H50Q and wild-type α-syn that we and others have observed (Fig. 4b,d,e)[18,19,25]. First, the observation that the H50Q mutation results in a large proportion of narrow fibrils formed from a single protofilament may help explain the faster aggregation kinetics of the mutant fibrils. Given that multiple molecules must come together to nucleate amyloid fibril growth, fibrils composed of a single protofilament may therefore have a shorter lag time than fibrils composed of two protofilaments, as half as many molecules are required to form the nucleus. Thus, the H50Q mutation may lower the barrier to nucleation and more readily lead to fibril formation. Previous studies on wild-type α-syn have demonstrated that minor species of single protofilament fibrils exist in polymorphic preparations, suggesting that wild-type α-syn can also form single protofilaments[20]. However, here we observe that single protofilament structures dominate, suggesting that the H50Q mutation may tip the balance to favor single protofilament fibrils and shorter lag times.

Second, the higher seeding capacity of H50Q versus wild-type fibrils in our biosensor cell assays may be explained by the presence of a secondary nucleation mechanism. We speculate that the wide fibril species represents a step in a secondary nucleation pathway whereby residues ^{58}KTKE^{61} of protofilament A serve as a surface to catalyze the formation of protofilament B (Extended Data Fig. 10)[35]. Several observations support this idea. (1) Protofilament B is never observed alone, and is only observed with protofilament A in the wide fibril, whereas protofilament A is observed alone in the narrow fibril. (2) The structure of protofilament A in both the narrow and wide fibril is nearly identical (r.m.s. deviation = 0.26 Å) and the helical twist of both the narrow and wide fibril is nearly identical (cross-over distance ~900 Å), suggesting that protofilament A acts as an unperturbed scaffold for protofilament B to grow off its side. (3) The wide fibril protofilament interface is exceedingly small, perhaps making it a labile interface where protofilament B can nucleate and elongate but eventually fall off, forming individual single protofilament fibrils. Given that we do not observe protofilament B alone, we speculate that over time protofilament B may convert into protofilament A, perhaps initiated by the switching of H50Q into a conformation that allows hydrogen bonding with K45 and subsequent formation of the Y39–T44–E46 hydrogen-bond triad. We speculate that the conversion of protofilament B to protofilament A may occur immediately before disassembling from the wide fibril to form individual narrow fibrils or after disassembly from the wide fibril (Extended Data Fig. 10).

We note that other mechanisms may lead to the differential seeding capacities that we observe; for instance, there may be a different seed fibril length distribution due to differing sensitivities to sonication between H50Q and wild-type fibrils. In addition, the monomeric α-syn-A53T-YFP may be easier or harder to seed by H50Q or wild-type fibrils due to species barrier effects. Although for the latter point, we note that the wild-type fibrils have only one residue different from the α-syn-A53T-YFP construct, whereas the H50Q fibrils have two differing residues, making the increased seeding potency of H50Q fibrils more noteworthy despite the greater difference in sequence.

Third, the ultrastructural arrangement of protofilaments, the ordered β-arch in protofilament A featuring a unique Y39–T44–E46 hydrogen-bond triad and the presence of islands 1 and 2 represent major structural differences in the H50Q fibrils compared to previously determined wild-type α-syn structures. These structural differences create new ordered surfaces on the fibrils that may enable

their heightened cytotoxicity compared to wild type. Previously, it has been shown that polyQ inclusions can sequester essential cellular proteins and that resupply of sequestered proteins ameliorated toxicity and reduced inclusion size, presumably by coating the fibrils and rendering them inert[36]. This highlights the importance of surfaces of fibrils in mediating cytotoxicity and suggests that different surface properties of amyloid fibrils may explain differential cytotoxicities. Indeed, others have shown that two polymorphs of wild-type α-syn could be homogenously prepared and that these polymorphs had different cytotoxicities to SH-SY5Y cells, suggesting that differences in structure, including exposed fibril surfaces, result in different cytotoxicity[37]. Therefore, we propose that the large structural differences observed in our H50Q fibrils compared to wild type could mediate the higher cytotoxicity of H50Q versus wild-type fibrils.

Hereditary mutations in α-syn are largely clustered in the pre-NAC region (residues 47–56) away from the NACore region (residues 68–78). The E46K hereditary mutation is predicted to disrupt a key salt bridge that forms between E46 and K80, potentially disturbing the fibril core. Consistent with this, NMR studies have shown large chemical shifts for residues in the fibril core of E46K fibrils[38]. Interestingly, in H50Q protofilament A, E46 participates in a hydrogen-bond network with T44 and Y39; therefore, mutation to lysine may disrupt this network making the formation of the N-terminal 36–46 β-arch mutually exclusive with the E46K hereditary mutation. Further, the observation that the E46–K80 hydrogen bond is not maintained in protofilament A—unlike the previous wild-type rod polymorphs and protofilament B—demonstrates that this interaction is not necessary to maintain the overall wild-type fold, and that, in the case of the E46K hereditary mutation, it is the change to lysine and unfavorable juxtaposition of the positively charged E46K and K80 that explains the rearrangement of the fibril core as indicated by NMR[38]. For mutations A30P and A53T, NMR studies of fibrils show small perturbations in chemical shifts and secondary structures at sites proximal to the mutation, suggesting that the overall fold of the fibril is largely unchanged[38,39]. Here, the H50Q mutation seems to lie somewhere in the middle of the A30P, A53T and E46K mutations; in that, H50Q enforces a new conformation of the N terminus of the fibril core, disrupts previously observed protofilament interfaces and creates a new protofilament interface, while maintaining a conserved β-arch fold in the fibril core. Further work is needed to determine the exact structural effects of other α-synuclein hereditary mutations.

Overall, our results demonstrate that the H50Q hereditary mutation leads to new fibril polymorphs that have more rapid fibril-forming kinetics, higher seeding capacity and higher cytotoxicity. These findings provide a starting point for understanding the structural basis of mutation-enhanced pathogenesis in the synucleinopathies.

Online content

Any methods, additional references, Nature Research reporting summaries, source data, extended data, supplementary information, acknowledgements, peer review information; details of author contributions and competing interests; and statements of data and code availability are available at https://doi.org/10.1038/s41594-019-0322-y.

Received: 23 June 2019; Accepted: 30 September 2019;
Published online: 6 November 2019

References

1. Spillantini, M. G., Crowther, R. A., Jakes, R., Hasegawa, M. & Goedert, M. α-Synuclein in filamentous inclusions of Lewy bodies from Parkinson's disease and dementia with Lewy bodies. *Proc. Natl Acad. Sci. USA* **95**, 6469–6473 (1998).
2. Grazia Spillantini, M. et al. Filamentous α-synuclein inclusions link multiple system atrophy with Parkinson's disease and dementia with Lewy bodies. *Neurosci. Lett.* **251**, 205–208 (1998).
3. Spillantini, M. G. & Goedert, M. Neurodegeneration and the ordered assembly of α-synuclein. *Cell Tissue Res.* **373**, 137–148 (2018).
4. Singleton, A. B. et al. α-Synuclein locus triplication causes parkinson's disease. *Science* **302**, 841–841 (2003).
5. Chartier-Harlin, M.-C. et al. α-synuclein locus duplication as a cause of familial Parkinson's disease. *Lancet* **364**, 1167–1169 (2004).
6. Ibáñez, P. et al. Causal relation between α-synuclein gene duplication and familial Parkinson's disease. *Lancet* **364**, 1169–1171 (2004).
7. Serpell, L. C., Berriman, J., Jakes, R., Goedert, M. & Crowther, R. A. Fiber diffraction of synthetic α-synuclein filaments shows amyloid-like cross-β conformation. *Proc. Natl Acad. Sci. USA* **97**, 4897–4902 (2000).
8. Luk, K. C. et al. Pathological α-synuclein transmission initiates Parkinson-like neurodegeneration in nontransgenic mice. *Science* **338**, 949–953 (2012).
9. Tycko, R. Solid-state NMR studies of amyloid fibril structure. *Annu. Rev. Phys. Chem.* **62**, 279–299 (2011).
10. Bai, X., McMullan, G. & Scheres, S. H. W. How cryo-EM is revolutionizing structural biology. *Trends Biochem. Sci.* **40**, 49–57 (2015).
11. Sawaya, M. R. et al. Atomic structures of amyloid cross-β spines reveal varied steric zippers. *Nature* **447**, 453–457 (2007).
12. Rodriguez, J. A. et al. Structure of the toxic core of α-synuclein from invisible crystals. *Nature* **525**, 486–490 (2015).
13. Colvin, M. T. et al. Atomic resolution structure of monomorphic $A\beta_{42}$ amyloid fibrils. *J. Am. Chem. Soc.* **138**, 9663–9674 (2016).
14. Li, B. et al. Cryo-EM of full-length α-synuclein reveals fibril polymorphs with a common structural kernel. *Nat. Commun.* **9**, 3609 (2018).
15. Proukakis, C. et al. A novel α-synuclein missense mutation in Parkinson disease. *Neurology* **80**, 1062–1064 (2013).
16. Appel-Cresswell, S. et al. Alpha-synuclein p.H50Q, a novel pathogenic mutation for Parkinson's disease. *Mov. Disord.* **28**, 811–813 (2013).
17. Rutherford, N. J., Moore, B. D., Golde, T. E. & Giasson, B. I. Divergent effects of the H50Q and G51D SNCA mutations on the aggregation of α-synuclein. *J. Neurochem.* **131**, 859–867 (2014).
18. Porcari, R. et al. The H50Q mutation induces a 10-fold decrease in the solubility of α-synuclein. *J. Biol. Chem.* **290**, 2395–2404 (2015).
19. Khalaf, O. et al. The H50Q mutation enhances α-synuclein aggregation, secretion, and toxicity. *J. Biol. Chem.* **289**, 21856–21876 (2014).
20. Dearborn, A. D. et al. α-Synuclein amyloid fibrils with two entwined, asymmetrically associated protofibrils. *J. Biol. Chem.* **291**, 2310–2318 (2016).
21. Fitzpatrick, A. W. P. et al. Cryo-EM structures of tau filaments from Alzheimer's disease. *Nature* **547**, 185–190 (2017).
22. Liberta, F. et al. Cryo-EM fibril structures from systemic AA amyloidosis reveal the species complementarity of pathological amyloids. *Nat. Commun.* **10**, 1104 (2019).
23. Cao, Q., Boyer, D. R., Sawaya, M. R., Ge, P. & Eisenberg, D. S. Cryo-EM structures of four polymorphic TDP-43 amyloid cores. *Nat. Struct. Mol. Biol.* **26**, 619–627 (2019).
24. Murray, D. T. et al. Structure of FUS protein fibrils and its relevance to self-assembly and phase separation of low-complexity domains. *Cell* **171**, 615–627.e16 (2017).
25. Ghosh, D. et al. The Parkinson's disease-associated H50Q mutation accelerates α-synuclein aggregation in vitro. *Biochemistry* **52**, 6925–6927 (2013).
26. Prusiner, S. B. et al. Evidence for α-synuclein prions causing multiple system atrophy in humans with parkinsonism. *Proc. Natl Acad. Sci. USA* **112**, E5308–E5317 (2015).
27. Li, Y. et al. Amyloid fibril structure of α-synuclein determined by cryo-electron microscopy. *Cell Res.* **28**, 897–903 (2018).
28. Guerrero-Ferreira, R. et al. Cryo-EM structure of α-synuclein fibrils. *eLife* **7**, e36402 (2018).
29. Tuttle, M. D. et al. Solid-state NMR structure of a pathogenic fibril of full-length human α-synuclein. *Nat. Struct. Mol. Biol.* **23**, 409–415 (2016).
30. Radamaker, L. et al. Cryo-EM structure of a light chain-derived amyloid fibril from a patient with systemic AL amyloidosis. *Nat. Commun.* **10**, 1103 (2019).
31. Swuec, P. et al. Cryo-EM structure of cardiac amyloid fibrils from an immunoglobulin light chain AL amyloidosis patient. *Nat. Commun.* **10**, 1269 (2019).
32. Nelson, R. et al. Structure of the cross-β spine of amyloid-like fibrils. *Nature* **435**, 773–778 (2005).
33. Falcon, B. et al. Novel tau filament fold in chronic traumatic encephalopathy encloses hydrophobic molecules. *Nature* **568**, 420–423 (2019).
34. Liu, C. et al. Out-of-register β-sheets suggest a pathway to toxic amyloid aggregates. *Proc. Natl Acad. Sci. USA* **109**, 20913–20918 (2012).
35. Cohen, S. I. A. et al. Proliferation of amyloid-β42 aggregates occurs through a secondary nucleation mechanism. *Proc. Natl Acad. Sci. USA* **110**, 9758–9763 (2013).

36. Hosp, F. et al. Spatiotemporal proteomic profiling of Huntington's disease inclusions reveals widespread loss of protein function. *Cell Rep.* **21**, 2291–2303 (2017).
37. Bousset, L. et al. Structural and functional characterization of two alpha-synuclein strains. *Nat. Commun.* **4**, 2575 (2013).
38. Lemkau, L. R. et al. Site-specific perturbations of alpha-synuclein fibril structure by the Parkinson's disease associated mutations A53T and E46K. *PLoS ONE* **8**, e49750 (2013).
39. Lemkau, L. R. et al. Mutant protein A30P α-synuclein adopts wild-type fibril structure, despite slower fibrillation kinetics. *J. Biol. Chem.* **287**, 11526–11532 (2012).

Methods

Protein purification. Full-length α-syn wild-type and H50Q mutant proteins were expressed and purified according to a published protocol[14]. The bacterial induction started at an optical density (OD_{600}) of ~0.6 with 1 mM IPTG for 6 h at 30 °C. The collected bacteria were lysed with a probe sonicator for 10 min in an iced water bath. After centrifugation, the soluble fraction was heated in boiling water for 10 min and then titrated with HCl to pH 4.5 to remove the unwanted precipitants. After adjusting to neutral pH, the protein was dialyzed overnight against Q Column loading buffer (20 mM Tris–HCl pH 8.0). The next day, the protein was loaded onto a HiPrep Q 16/10 column and eluted using elution buffer (20 mM Tris–HCl, 1 M NaCl, pH 8.0). The eluent was concentrated using Amicon Ultra-15 centrifugal filters (Millipore Sigma) to ~5 ml. The concentrated sample was further purified with size-exclusion chromatography through a HiPrep Sephacryl S-75 HR column in 20 mM Tris, pH 8.0. The purified protein was dialyzed against water, concentrated to 3 mg ml^{-1} and stored at 4C. The concentration of the protein was determined using the Pierce BCA Protein Assay Kit (Thermo Fisher Scientific, catalog no. 23225).

Fibril preparation and optimization. Both wild-type and H50Q fibrils were grown under the same condition: 300 μM purified monomers, 15 mM tetrabutylphosphonium bromide, shaking at 37 °C for 2 weeks.

Negative stain transmission electron microscopy (TEM). The fibril sample (3 μl) was spotted onto a freshly glow-discharged carbon-coated electron microscopy grid. After 1 min, 6 μl uranyl acetate (2% in aqueous solution) was applied to the grid for 1 min. The excess stain was removed by a filter paper. Another 6 μl uranyl acetate was applied to the grid and immediately removed. The samples were imaged using an FEI T20 electron microscope.

ThT binding assay. Purified α-syn monomers (50 μM) were adequately mixed with 20 μM ThT and added into a 96-well-plate. Samples were incubated at 37 °C for 2 d with 600 r.p.m. double orbital shaking. The ThT signal was monitored using the FLUOstar Omega Microplate Reader (BMG Labtech) at an excitation wavelength of 440 nm and an emission wavelength of 490 nm.

SDS stability. SDS was diluted in water to make SDS solutions at 2.5, 5, 10 and 15%. Fibrils at the end of the ThT assay were treated with SDS solution at 5:1 volume ratio to obtain SDS concentrations of 0.5, 1, 2 and 3%. Each solution was transferred to three microcentrifuge tubes and heated at 70 °C for 15 min. After treatment, the ThT signal was obtained. The 0% SDS solution without heating was treated with an equal amount of water and used for normalization.

Cell lines. HEK293T biosensor cells expressing α-syn-A53T-YFP were a generous gift from the laboratory of M. Diamond. PC12 cells originate from the American Type Culture Collection (ATCC CRL-1721). Cells were not authenticated nor tested for mycoplasma infection in our hands.

Fibril seeding aggregation in cells. We performed the biosensor cell seeding assay based on a previously published protocol[26]. Briefly, the assay works as follows: exogenous, unlabeled fibrils are transfected into HEK293T cells expressing α-syn-A53T-YFP. Seeded aggregation of endogenously expressed α-syn-A53T-YFP is monitored by formation of fluorescent puncta. The puncta represent a condensation of α-syn-A53T-YFP as a result of seeding by exogenous H50Q or wild-type fibrils.

HEK293T cells expressing full-length α-syn containing the hereditary A53T mutation were grown in DMEM (4 mM L-glutamine and 25 mM D-glucose) supplemented with 10% FBS, 1% penicillin/streptomycin. Trypsin-treated HEK293T cells were collected, seeded on flat 96-well plates at a concentration of 4×10^4 cells per well in 200 μl culture medium per well and incubated in 5% CO_2 at 37 °C for 18 h.

α-syn fibrils were prepared by diluting with Opti-MEM (Life Technologies) and sonicating in a water bath sonicator for 10 min. The fibril samples were then mixed with Lipofectamine 2000 (Thermo Fisher Scientific) and incubated for 15 min and then added to the cells. The actual volume of Lipofectamine 2000 was calculated based on the dose of 1 μl per well. After 48 h of transfection, the cells were imaged with a Celigo Imaging Cytometer (Nexcelom Bioscience). Fluorescent images were processed in ImageJ to count the number of seeded cells. A buffer-treated control was used for normalization.

MTT mitochondrial activity assay. The addition of sonicated fibrils to nerve growth factor-differentiated PC12 cells is a well-established assay to measure cytotoxicity of amyloid fibrils[40,41]. Use of this neuron-like cell line allows us to obtain a biologically relevant assay for cytotoxicity. Our MTT mitochondrial activity assay followed our previously published protocol[14], which was adapted from the Provost and Wallert laboratories[42]. Thiazolyl blue tetrazolium bromide for the MTT cell toxicity assay was purchased from Millipore Sigma (catalog no. M2128–1G). PC12 cells were plated in 96-well plates with nerve growth factor. The cells were incubated for 2 d in an incubator with 5% CO_2 at 37 °C. The cells were treated with different concentrations of α-syn fibrils (200 nM, 500 nM,1,000 nM, 2,000 nM), which were sonicated in a water bath sonicator for 10 min before being added to the cells. After 18 h incubation, MTT was added to every well and the plate was returned to the incubator for 3.5 h. Absorbance was measured at 570 nm to determine the MTT signal and at 630 nm to determine background. The data were normalized to those from cells treated with 1% SDS to obtain a value of 0%, and to those from cells treated with PBS to obtain a value of 100%.

Lactate dehydrogenase assay. The lactate dehydrogenase viability assay was performed using the CytoTox-ONE Homogeneous Membrane Integrity Assay (Promega, catalog no. G7891). PC12 cells were cultured and differentiated with the same protocol as described in the MTT assay. Different concentrations of α-syn fibrils (200 nM, 500 nM, 1,000 nM, 2,000 nM) were added to the cells for 18 h of incubation with 5% CO_2 at 37 °C. The assay was carried out in a 96-well plate and the fluorescence readings were taken in the FLUOstar Omega Microplate Reader (excitation 560 nm, emission 590 nm; BMG Labtech). PBS- and 0.2% Triton-X100-treated cells were used as negative and positive controls, respectively, for normalization.

Cryo-EM data collection and processing. Fibril solution (2 μl) was applied to a baked and glow-discharged Quantifoil 1.2/1.3 electron microscope grid and plunge-frozen into liquid ethane using a Vitrobot Mark IV (FEI). Data were collected on a Titan Krios (FEI) microscope equipped with a Gatan Quantum LS/K2 Summit direct electron detection camera (operated with 300 kV acceleration voltage and slit width of 20 eV). Counting mode movies were collected on a Gatan K2 Summit direct electron detector with a nominal physical pixel size of 1.07 Å per pixel with a dose per frame 1.2 $e^-/Å^2$. A total of 30 frames with a frame rate of 5 Hz were taken for each movie, resulting in a final dose 36 $e^-/Å^2$ per image. Automated data collection was driven by the Leginon automation software package[43].

Micrographs containing crystalline ice were used to estimate the anisotropic magnification distortion using mag_distortion_estimate[44]. CTF estimation was performed using CTFFIND 4.1.8 on movie stacks with a grouping of three frames and correction for anisotropic magnification distortion[45]. Unblur[46] was used to correct beam-induced motion with dose weighting and anisotropic magnification correction, resulting in a physical pixel size of 1.065 Å per pixel.

All particle picking was performed manually using EMAN2 e2helixboxer.py[47]. We manually picked two groups of particles for further data processing: the first group was composed of all fibrils and the second group was composed of wide fibrils. For the first group, particles were extracted in RELION using the 90% overlap scheme into 1,024- and 288-pixel boxes. Classification, helical reconstruction and three-dimensional (3D) refinement were used in RELION as described[23]. For the first group of all particles, we isolated narrow fibrils during two-dimensional (2D) classification and subsequently processed them as a separate data set. 2D classifications of narrow fibril 1,024-pixel boxes were used to estimate helical parameters. We performed 3D classification with the estimated helical parameters for narrow fibrils and an elongated Gaussian blob as an initial model to generate starting reconstructions. We ran additional 3D classifications using the preliminary reconstructions from the previous step to select for particles contributing to homogenous classes (stable helicity and separation of β-strands in the x–y plane). Typically, we performed Class3D jobs with $K = 3$ and manual control of the tau_fudge factor and healpix to reach a resolution of ~5–6 Å to select for particles that contributed to the highest resolution class for each structure. We employed Refine3D on a final subset of narrow fibril particles with 288-pixel box size to obtain the final reconstruction. We performed the map–map Fourier shell correlation (FSC) with a generous, soft-edged solvent mask and high-resolution noise substitution in RELION PostProcess, resulting in a resolution estimate of 3.3 Å.

We extracted particles from the wide fibril dataset using 1,024- and 686-pixel boxes. 2D classifications of 1,024- and 686-pixel boxes were used to estimate helical parameters. 2D classifications of 686-pixel boxes were used to further isolate only wide fibril segments, since there were still some other fibril species that were included due to the fact that we could not separate all fibril species perfectly during manual picking. Once a homogenous set of wide fibrils was obtained during 2D classification of 686-pixel boxes, we performed a 3D reconstruction using an elongated Gaussian blob as an initial model. The asymmetry present in the 686 box, 2D class averages of the wide fibril (Extended Data Fig. 2d) prompted us to use a helical rise of 4.8 Å and C1 symmetry, due to the fact that if a twofold symmetry were present in the fibrils, 2D class averages would display a mirror symmetry across the fibril axis. After an initial 2D model was generated for the wide fibril, we re-extracted all tubes corresponding to those particles included in the final subset of wide fibril 686-pixel boxes with a box size of 224 pixels. All 224-pixel boxes were subjected to multiple rounds of 3D classification using the initial 686-pixel box wide fibril reconstruction as a reference. We refined the final subset of particles using Refine3D to a resolution of 3.6 Å. We performed resolution estimation as described above for the narrow fibrils.

Atomic model building. We sharpened both the narrow and wide fibril reconstructions using phenix.auto_sharpen[48] at the resolution cut-off indicated by the map–map FSC and subsequently built atomic models into the refined maps with Coot[49]. We built the model for the narrow fibril de novo using previous

structures of wild-type α-synuclein fibrils as guides. To build the wide fibril model, we made a copy of one chain of the narrow fibril structure and rigid-body fit it into the second protofilament density observed in the wide fibril reconstruction. This resulted in the wide fibril being composed of one protofilament nearly identical to the narrow fibril, and one protofilament with less ordered N and carboxy (C) termini, therefore resulting in an asymmetric double protofilament structure.

For both narrow and wide fibrils, we generated a five-layer model to maintain local contacts between chains in the fibril during structure refinement. We performed automated structure refinement for both narrow and wide fibrils using phenix.real_space_refine[50]. We employed hydrogen bond distance and angle restraints for backbone atoms participating in β-sheets and side chain hydrogen bonds during automated refinements. We performed comprehensive structure validation of all our final models in Phenix.

Although we did not include coordinates in our final models for additional residues that could occupy islands 1 and 2 neighboring protofilament A, because we could not be certain which residues occupy those densities, we built several speculative models (Extended Data Fig. 4). For island 2, we assumed that there was a short disordered linker between residue 36 of protofilament A and island 2, resulting in the residues occupying island 2 forming a tight interface with ^{36}GVLYVG^{41} of the fibril core. We noticed that the sequence ^{32}KTKE^{35} immediately precedes the last ordered residue of protofilament A, G36. The sequence ^{32}KTKE^{35} often forms the bends that connect straight β-strands in the ordered fibril core, so we assumed that this sequence would be a good candidate to form the tight bend that connects G36 to island 2. Therefore, we modeled in residues ^{26}VAEAAG^{31} into island 2. These residues satisfied the requirements of having short, hydrophobic side chains forming the tight interface with residues V38 and L40 from the fibril core.

For island 1, we assumed that the densities come either from the N terminus of protofilament A or from the C terminus of protofilament B. For the former case, we assume that there is a minimum of approximately eight residues that are disordered between the end of island 2 and the beginning of island 1 (see Extended Data Fig. 4). This is because there is 27 Å between the end of island 2 (V26) and the beginning of island 1, and we assume a minimum of ~3.3 Å per residue. Therefore, we threaded eight residues at a time from the region ^{1}MDVFMKGLSKAKEGVVAAA^{19} onto a β-strand backbone placed in the island 1 density to identify candidate octamers. While most sequences could not plausibly occupy island 1, due to steric clashes with the preNAC region of the fibril core, or due to glycine residues occupying positions where there were obvious side chain densities, several candidate sequences were identified (Extended Data Fig. 3).

We followed a similar protocol to identify possible sequences from the C terminus. In this case, we assume that these residues could come from either a largely disordered protofilament B molecule in the narrow fibril or an ordered protofilament B molecule as seen in the wide fibril (see Extended Data Fig. 3). Here, we assume there is a minimum of ~15 residues from the last ordered residue of the C terminus of protofilament B—since we assume a minimum of ~3.3 Å per residue and there is ~45 Å between K97 of protofilament B and the beginning of island 1 (see Extended Data Fig. 3). Therefore, we threaded all possible octamers from the region ^{112}ILEDMPVDPDNEAYEMPSEEGYQDYEPEA^{140} onto a β-strand backbone occupying island 1 to identify candidate sequences following the same criterion as above.

We created the speculative model of an H50Q double protofilament containing a homomeric preNAC interface by aligning a single chain from the H50Q narrow protofilament with the helical axis of the wild-type 'rod' structure (6CU7) and applying a pseudo-2(1) helical symmetry to generate a symmetrically related second chain.

Energetic calculation. The stabilization energy is an adaptation of the solvation free energy described previously[51], in which the energy is calculated as the sum of products of the area buried of each atom and its corresponding atomic solvation parameter (ASP). ASPs were taken from our previous work[51]. Area buried is calculated as the difference in solvent accessible surface area (SASA) of the reference state (that is, the unfolded state) and the SASA of the folded state. The SASA of residue i of the unfolded state was approximated as the SASA of residue i in the folded structure after removal of all other atoms except the main chain atoms of residues $i-1$ and $i+1$. The SASA of the folded state was measured for each atom in the context of all amyloid fibril atoms. Fibril coordinates were extended by symmetry by three to five chains on either side of the reported molecule, to ensure the energetic calculations were representative of the majority of molecules in a fibril, rather than a fibril end. To account for energetic stabilization of main chain hydrogen bonds, the ASP for backbone N/O elements was reassigned from −9 to 0 if they participated in a hydrogen bond. Similarly, if an asparagine or glutamine side chain participated in a polar ladder (two hydrogen bonds per amide), and was shielded from solvent (SASAfolded < 5 Å^2), the ASPs of the side chain N and O elements were reassigned from −9 to 0. Last, the ASP of ionizable atoms (in, for example, Asp, Glu, Lys, His, Arg, N-terminal amine, or C-terminal carboxylate) were assigned the charged value (−37/−38), unless the atoms participated in a buried ion pair, defined as a pair of complementary ionizable atoms within 4.2 Å distance of each other, each with SASAfolded < 40 Å^2). In that case, the ASP of the ion pair was reassigned to −9. In the energy diagrams, a single color is assigned to each residue, rather than each atom. The color corresponds to the sum of solvation free energy values of each of the atoms in the residue. The energy reported for FUS in Table 2 is the average over 20 NMR models. The standard deviation is 1.8 kcal mol^{-1}.

Reporting Summary. Further information on research design is available in the Nature Research Reporting Summary linked to this article.

Data availability

All structural data have been deposited into the Protein Database (PDB) and the Electron Microscopy Data Bank (EMDB) with the following accession codes: H50Q narrow fibril (PDB 6PEO, EMD-20328) and H50Q wide fibril (PDB 6PES, EMD-20331). All other data are available from the authors upon reasonable request.

References

40. Wakabayashi, M. & Matsuzaki, K. Formation of amyloids by Aβ-(1–42) on NGF-differentiated PC12 cells: roles of gangliosides and cholesterol. *J. Mol. Biol.* **371**, 924–933 (2007).
41. Ono, K., Condron, M. M. & Teplow, D. B. Structure–neurotoxicity relationships of amyloid β-protein oligomers. *Proc. Natl Acad. Sci. USA* **106**, 14745–14750 (2009).
42. van Meerloo, J., Kaspers, G. J. L. & Cloos, J. in *Cancer Cell Culture*: *Methods and Protocols* (ed. Cree, I. A.) 237–245 (Humana Press, 2011).
43. Suloway, C. et al. Automated molecular microscopy: the new leginon system. *J. Struct. Biol.* **151**, 41–60 (2005).
44. Grant, T. & Grigorieff, N. Automatic estimation and correction of anisotropic magnification distortion in electron microscopes. *J. Struct. Biol.* **192**, 204–208 (2015).
45. Rohou, A. & Grigorieff, N. CTFFIND4: fast and accurate defocus estimation from electron micrographs. *J. Struct. Biol.* **192**, 216–221 (2015).
46. Grant, T. & Grigorieff, N. Measuring the optimal exposure for single particle cryo-EM using a 2.6 Å reconstruction of rotavirus VP6. *eLife* **4**, e06980 (2015).
47. Tang, G. et al. EMAN2: an extensible image processing suite for electron microscopy. *J. Struct. Biol.* **157**, 38–46 (2007).
48. Terwilliger, T. C., Sobolev, O. V., Afonine, P. V. & Adams, P. D. Automated map sharpening by maximization of detail and connectivity. *Acta Crystallogr. D* **74**, 545–559 (2018).
49. Emsley, P., Lohkamp, B., Scott, W. G. & Cowtan, K. Features and development of coot. *Acta Crystallogr. D* **66**, 486–501 (2010).
50. Afonine, P. V. et al. Real-space refinement in PHENIX for cryo-EM and crystallography. *Acta Crystallogr. D* **74**, 531–544 (2018).
51. Eisenberg, D. S., Wesson, M. & Yamashita, M. Interpretation of protein folding and binding with atomic solvation parameters. *Chem. Scr.* **29A**, 217–222 (1989).

Acknowledgements

We thank H. Zhou for use of Electron Imaging Center for Nanomachines (EICN) resources and P. Ge for assistance in cryo-EM data collection. We acknowledge the use of instruments at the EICN supported by NIH (grant nos. 1S10RR23057 and 1S10OD018111), NSF (grant no. DBI-1338135) and CNSI at UCLA. The authors acknowledge grant nos. NIH AG 060149, NIH AG 054022, NIH AG061847 and DOE DE-FC02-02ER63421 for support. D.R.B. was supported by the National Science Foundation Graduate Research Fellowship Program.

Author contributions

D.R.B. and B.L. designed experiments and performed data analysis. B.L. and C.S. expressed and purified the α-syn protein. B.L. grew fibrils of α-syn and performed biochemical experiments. D.R.B. and B.L prepared cryo-EM samples and performed cryo-EM data collection. B.L. and W.F. selected filaments from cryo-EM images. D.R.B. performed cryo-EM data processing and built the atomic models. M.R.S. wrote the software for and D.R.B. carried out solvation energy calculations. All authors analyzed the results and D.R.B wrote the manuscript with input from all authors. L.J. and D.S.E. supervised and guided the project.

Competing interests

D.S.E. is an advisor and equity shareholder in ADRx, Inc.

Additional information

Extended data is available for this paper at https://doi.org/10.1038/s41594-019-0322-y.

Supplementary information is available for this paper at https://doi.org/10.1038/s41594-019-0322-y.

Correspondence and requests for materials should be addressed to L.J. or D.S.E.

Peer review information Inês Chen was the primary editor on this article and managed its editorial process and peer review in collaboration with the rest of the editorial team.

Reprints and permissions information is available at www.nature.com/reprints.

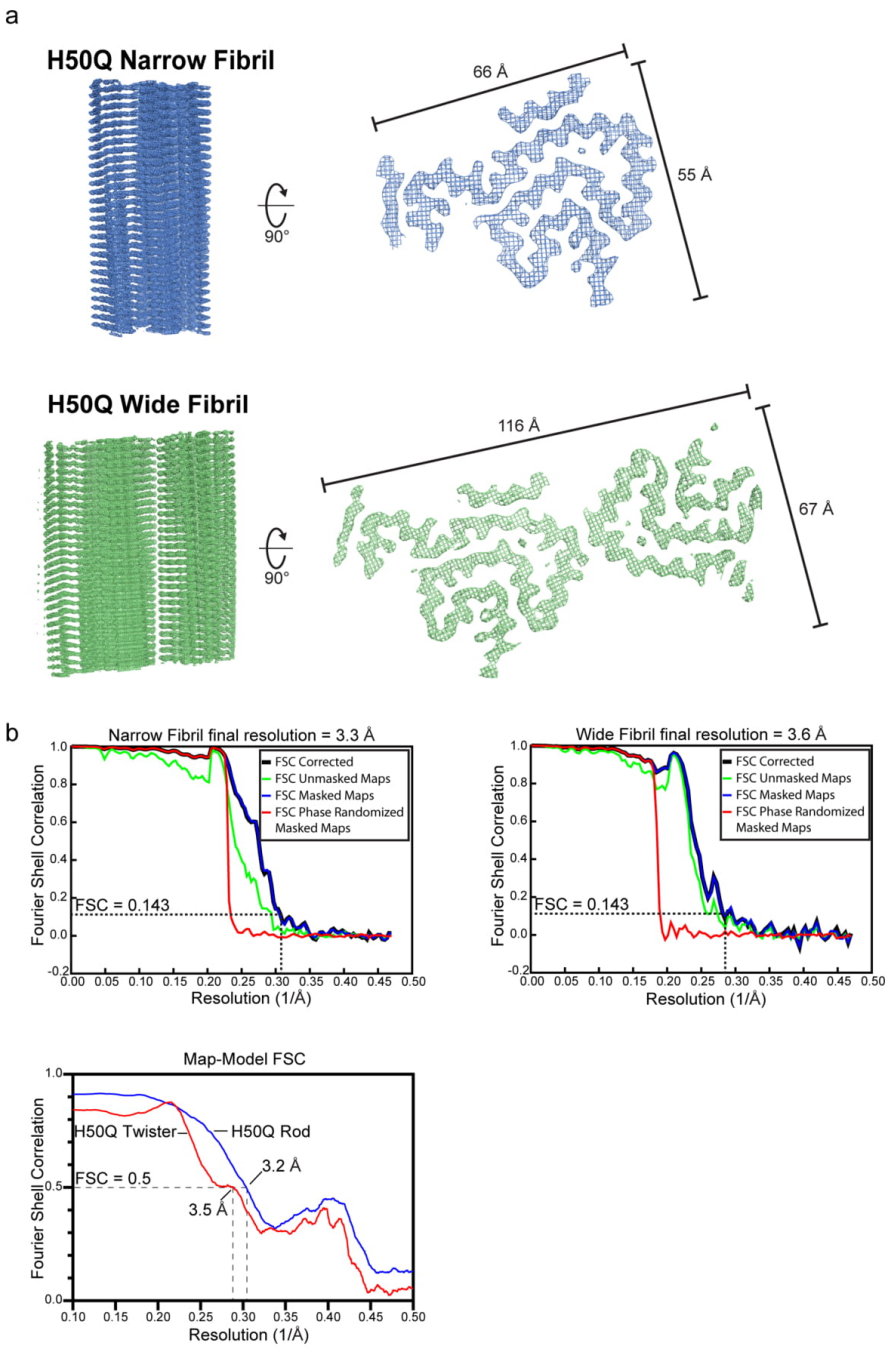

Extended Data Fig. 1 | Fourier Shell Analysis. a) Helical reconstructions of Narrow and Wide Fibrils with minimum and maximum widths labeled. b) Gold-standard half map FSC curves for Narrow (top, left) and Wide (top, right) Fibrils. Map-model FSC curve for Narrow and Wide Fibrils (bottom).

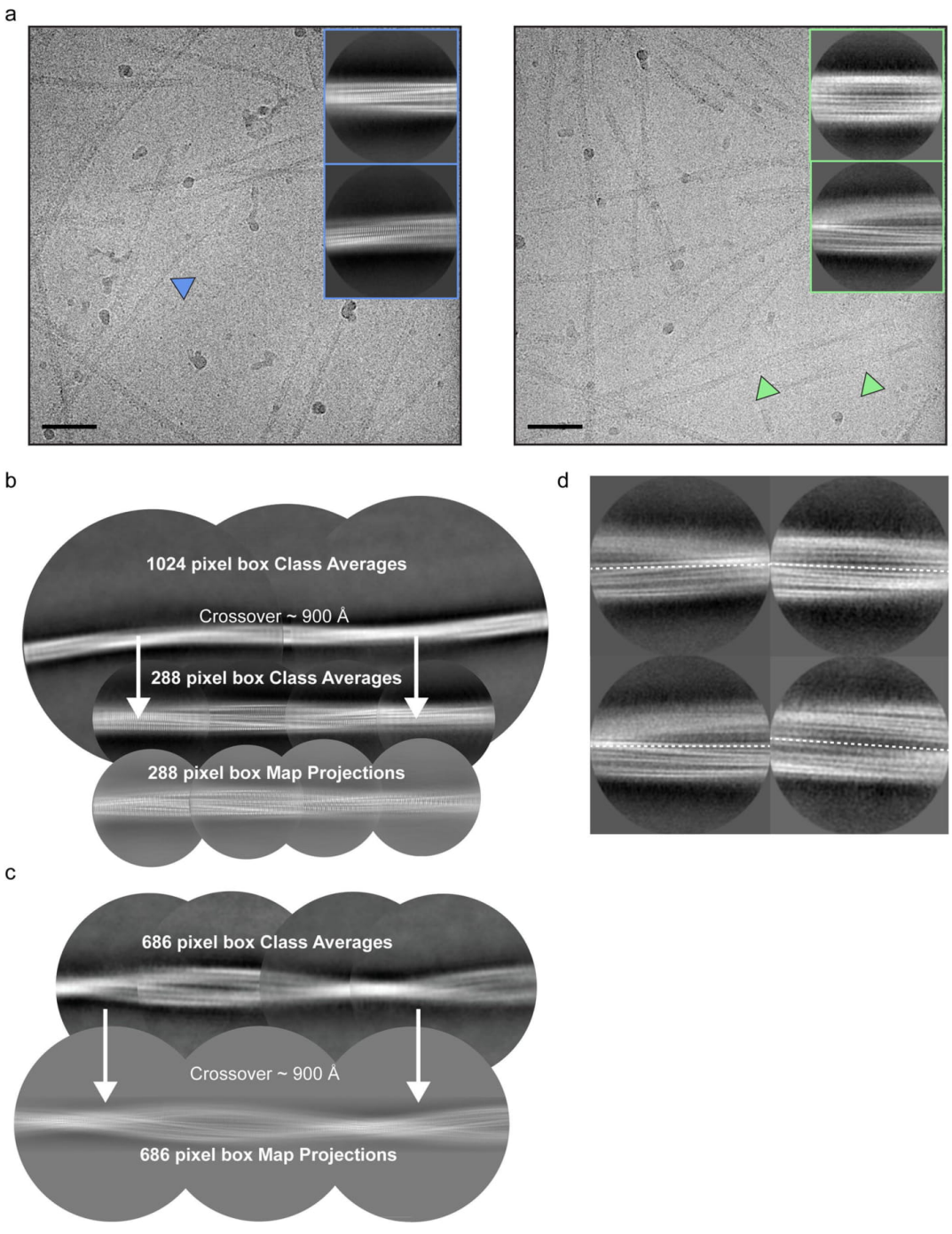

Extended Data Fig. 2 | see figure caption on next page.

Extended Data Fig. 2 | Cryo-EM images and processing. a) Cryo-EM micrographs and 2D class averages of Narrow (left) and Wide (right) Fibrils. Scale bar = 50 nm. b) 1024 and 288 pixel box size class averages of the Narrow Fibril used to determine crossover distance. 288 pixel box map projections match 2D class averages. c) 686 pixel box size class averages used to determine crossover distance. 686 pixel box map projections match 2D class averages. d) Wide Fibril class averages with a 320 pixel box demonstrate a lack of two-fold symmetry across the fibril axis.

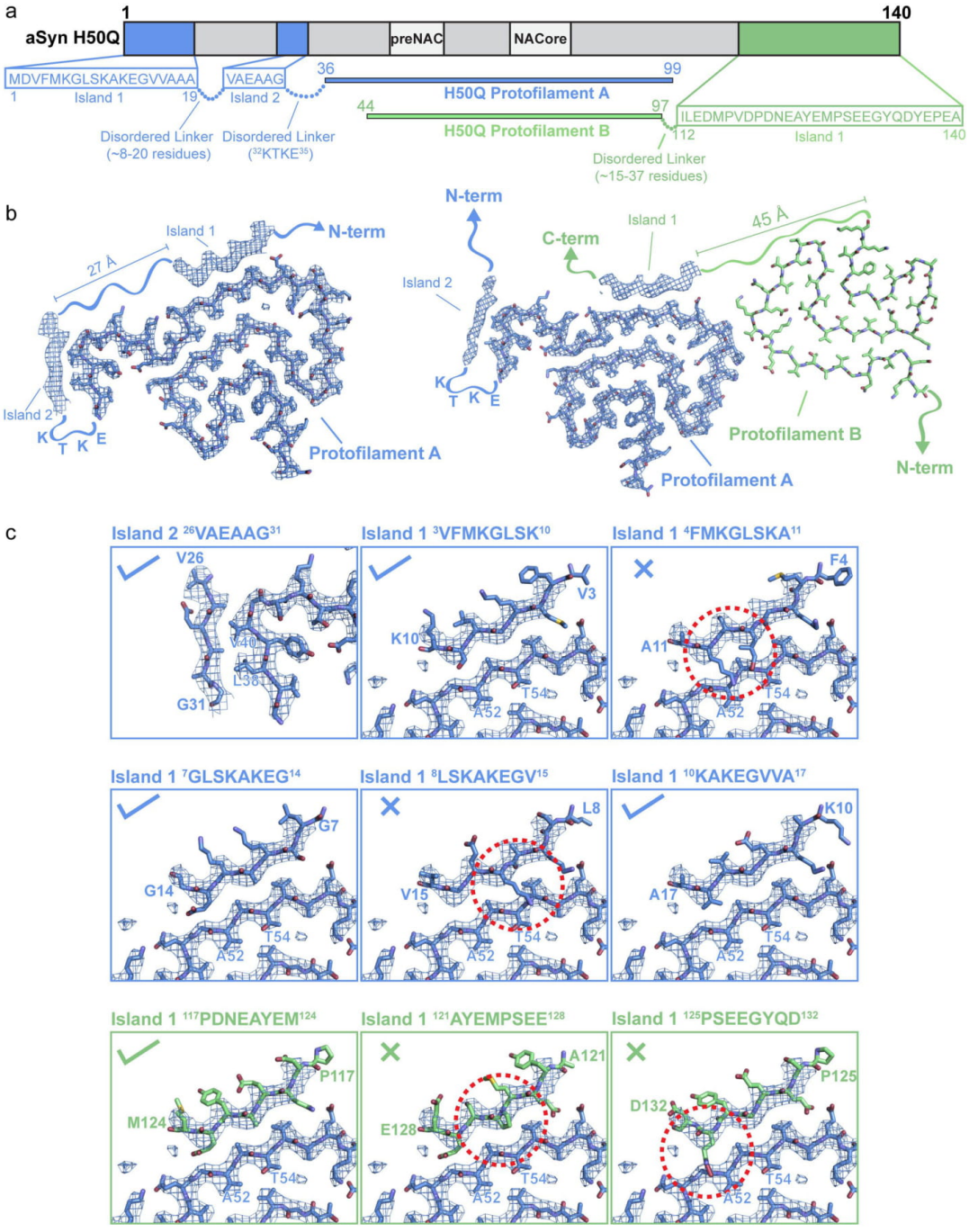

Extended Data Fig. 3 | see figure caption on next page.

Extended Data Fig. 3 | Speculative Atomic Models for Islands 1 and 2. a) Schematic illustrating possible sequences occupying Islands 1 and 2. 8mers from residues 1–19 and 112–140 were considered as possibilities to occupy Island 1. Island 2 is considered to consist of residues 26–31 followed by a disordered linker formed by residues ^{32}KTKE^{35}. b) Illustration of possible regions from either Protofilament A (left) or Protofilament B (right) that could occupy Island 1. Note that residues from the N-terminus of Protofilament A could account for Island 1 in both the Narrow and Wide Fibril; however, only the Narrow Fibril model is shown here. Island 2 is thought to be formed by the N-terminus of Protofilament A in both Narrow and Wide Fibrils. c) Speculative models for Islands 1 and 2. Check marks indicate plausible models while X's indicate implausible models. Island 1 models are from either the N-terminus of Protofilament A (blue panels) or the C-terminus of Protofilament B (green panels). Examples of sequences that were found to not be allowed to occupy Island 1 are shown with red dashed circles highlighting steric clashes or β-strand breaking proline residues.

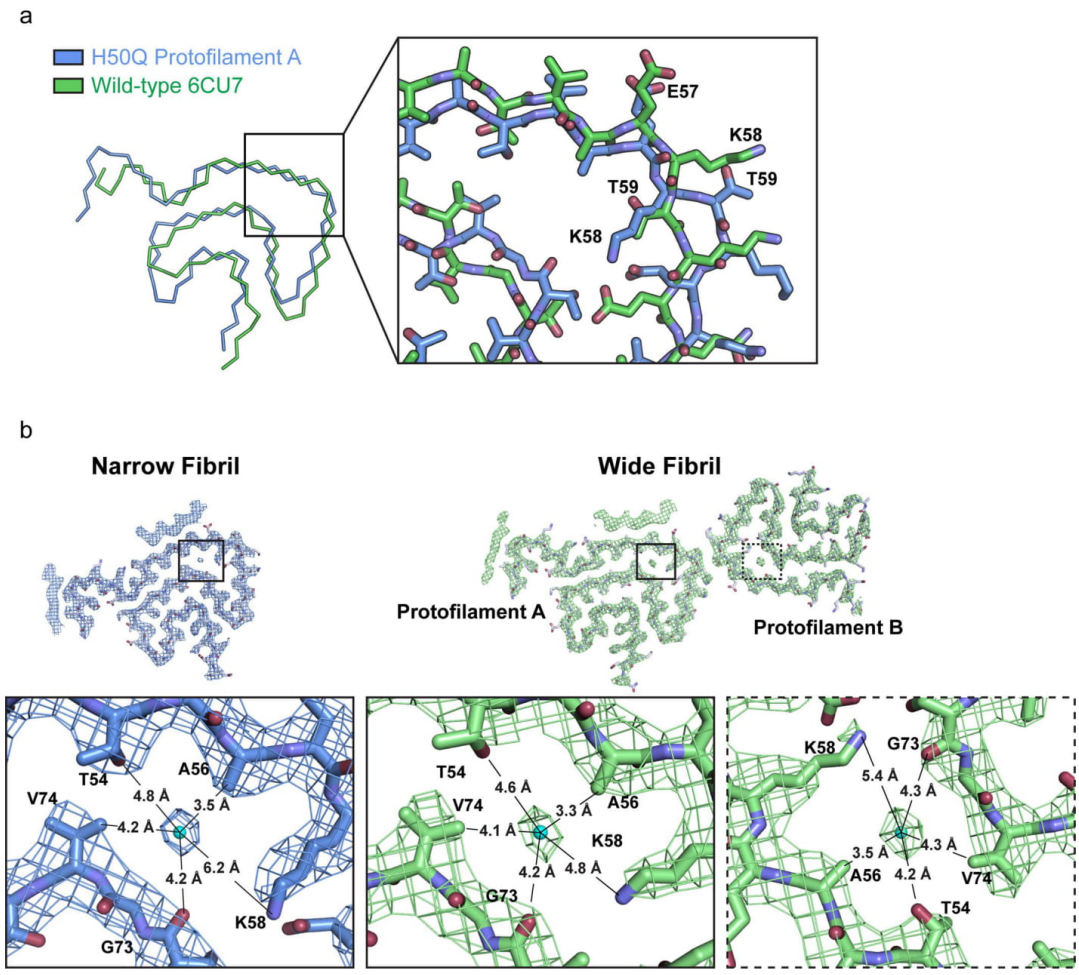

Extended Data Fig. 4 | Alternate conformations of K58 and T59 and potential solvent molecules in the α-syn β-arch cavity. a) Wild-type and H50Q fibrils display alternate conformations of K58 and T59. We note that in order for the Wide Fibril to form, T59 needs to be facing away from the fibril core. Therefore the formation of the Wide Fibril is mutually exclusive with our wild-type rod polymorph. b) Environmental distances of putative water molecule for Protofilament A and B in Wide Fibril and b) Protofilament A in Narrow Fibril.

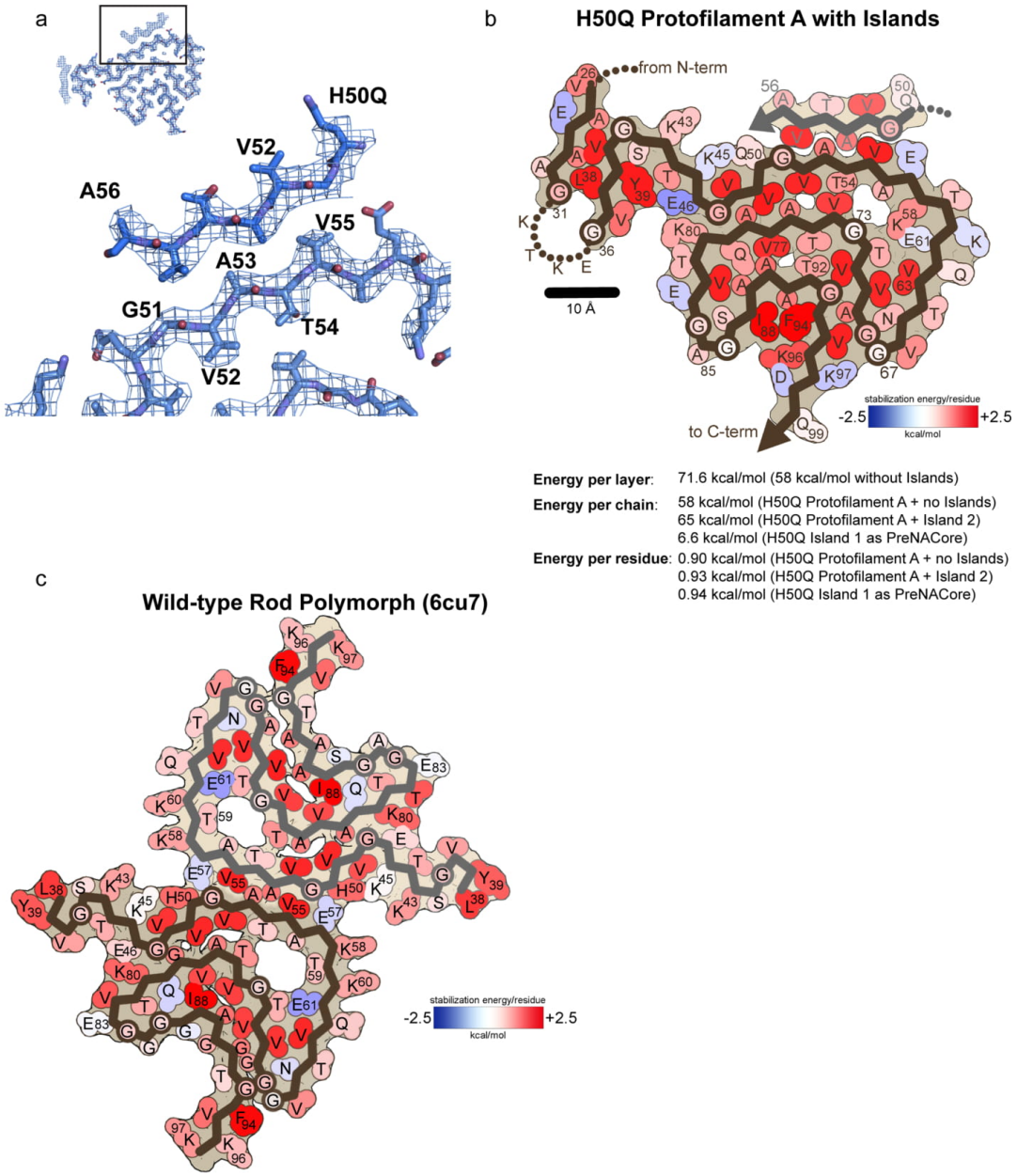

Extended Data Fig. 5 | PreNAC homozipper Island 1 model and additional solvation energy maps. a) Speculative model of preNAC residues ^{50}QGVATVA^{56} occupying Island 1 in Protofilament A. b) Atomic solvation map and energetic calculations for Protofilament A with Island 1 as ^{50}QGVATVA^{56} and Island 2 as ^{26}VAEAAG^{31}. c) Atomic energy solvation map for Wild-type rod polymorph (6cu7). Notice that K58 and T59 can have favorable stabilization energies whether they are facing the solvent or facing the cavity in the β-arch.

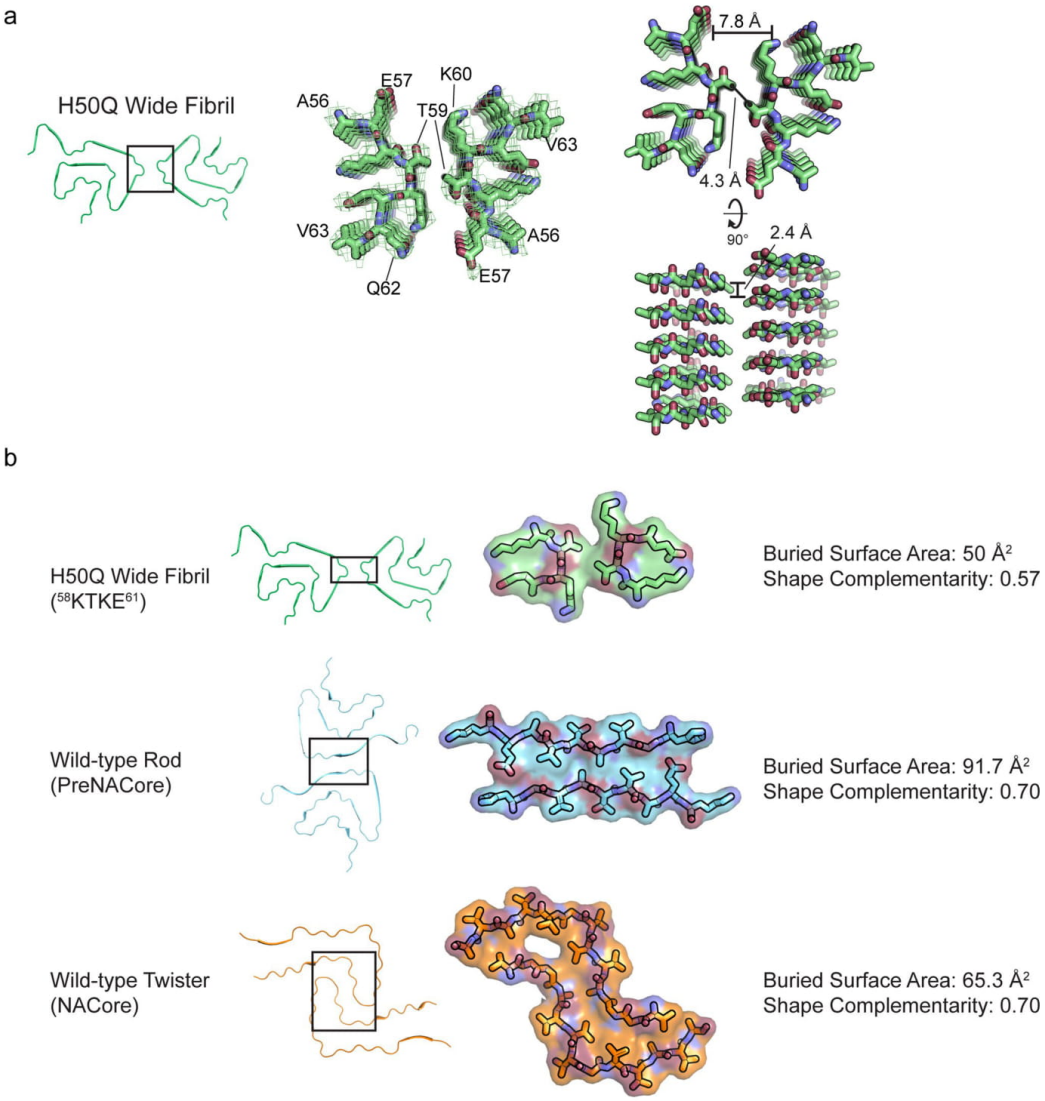

Extended Data Fig. 6 | Comparison of α-syn protofilament interfaces. a) Wide Fibril overview (left). 56AEKTKEQV63 homointerface with Wide Fibril electron density (middle). 56AEKTKEQV63 homointerface showing a 2.4 Å rise between mated strands from Protofilament A and Protofilament B and a distance of 7.8 Å between mated sheets of Protofilament A and B (right). b) Van der Waal's surface, buried surface area, and shape complementarity of 58KTKE61 homointerface, preNAC interface, and NACore interface.

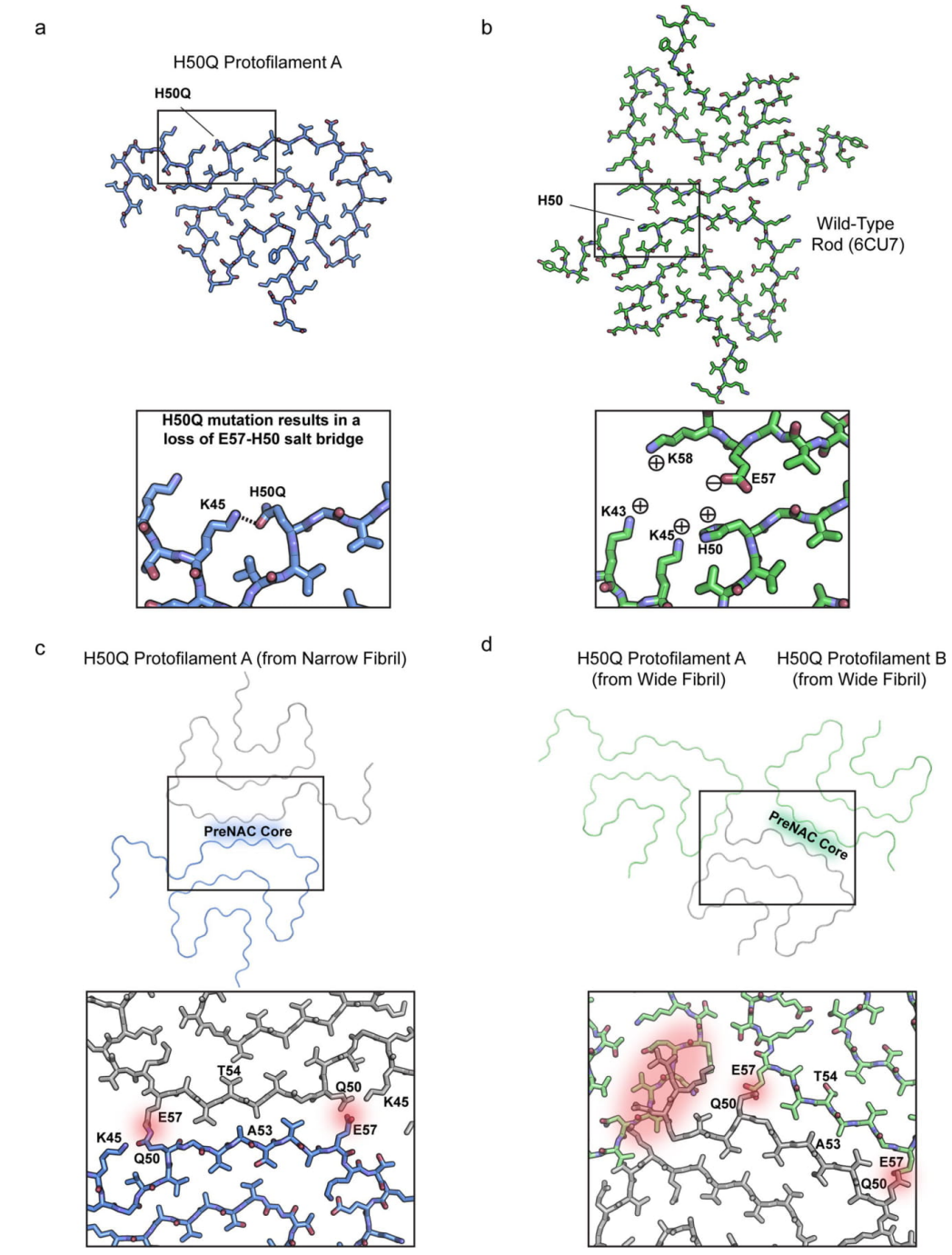

Extended Data Fig. 7 | see figure caption on next page.

Extended Data Fig. 7 | H50Q disrupts the wild-type rod polymorph preNAC protofilament interface. a) Conformation of H50Q Protofilament A K45 and H50Q. b) Interaction of K45-H50-E57 in the wild-type rod polymorph protofilament interface. c) Hypothetical H50Q double protofilament using the preNAC of Protofilament A as a steric zipper interface. Notice that the H50Q mutation disfavors the protofilament interface due to steric clashes with E57. d) Hypothetical H50Q protofilament interface using preNAC of Protofilament B. Notice the steric clashes between H50Q and E57 at the hypothetical protofilament interface as well as clashes of other parts of the protofilament with Protofilament A.

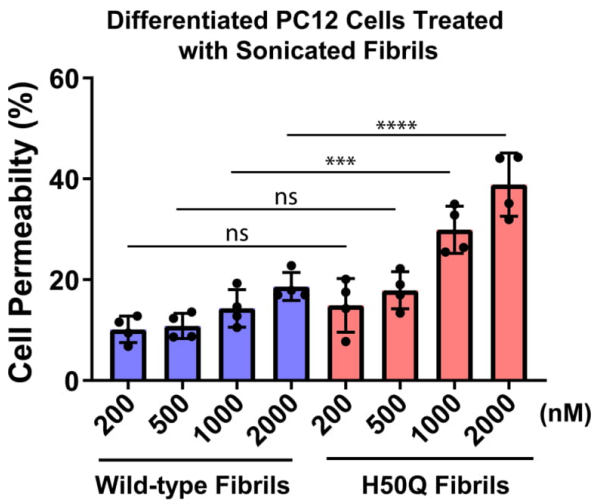

Extended Data Fig. 8 | H50Q fibrils disrupt PC12 cell membranes more than WT fibrils. Differentiated PC12 cells were treated with sonicated WT and H50Q fibrils and cell permeability was measured via LDH activity in the media (see Methods). H50Q leads to significantly higher cell permeabilization at 1000 and 2000 nM than WT a-syn. Error bars represent standard deviation of four independent experiments. **** = p-value ≤ 0.0001. *** = p-value ≤ 0.001. ns = p-value > 0.05. P-values were calculated using an unpaired, two-tailed t-test with a 95% CI.

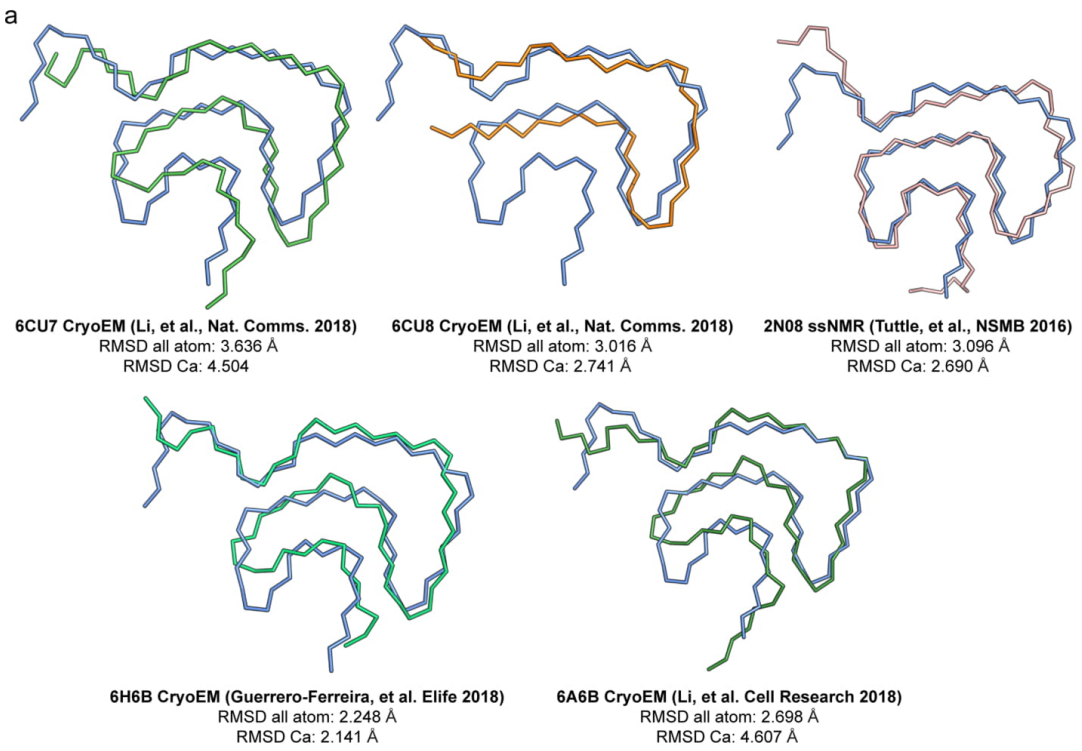

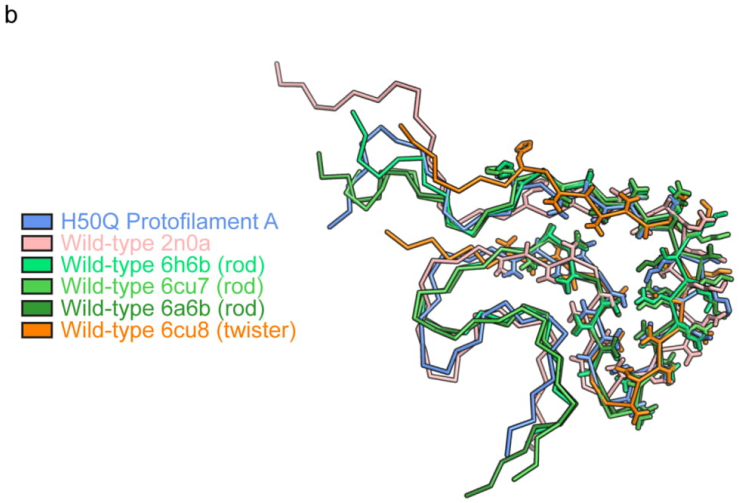

Extended Data Fig. 9 | Structural alignment of different wild-type and mutant α-syn polymorphs. a) Structural alignment of H50Q Protofilament A with all wild-type structures determined thus far. b) Structural alignment of residues 50–57 in wild-type and mutant α-syn polymorphs reveals the kernel region is largely conserved while tail regions, especially the N-terminus, adopt variable conformations.

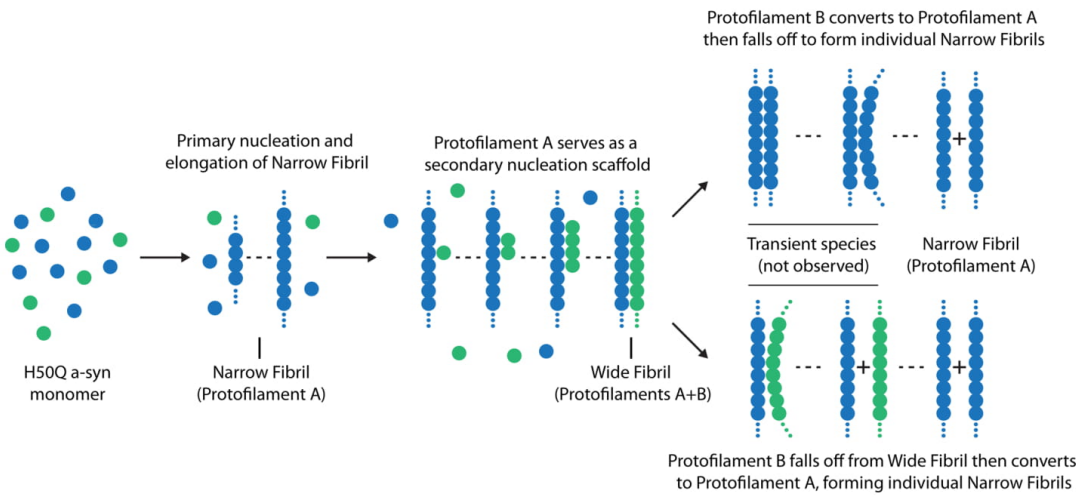

Extended Data Fig. 10 | Schematic illustrating possible secondary nucleation of Protofilament B by Narrow Fibrils.

nature structural & molecular biology

SUPPLEMENTARY INFORMATION

https://doi.org/10.1038/s41594-019-0322-y

In the format provided by the authors and unedited.

Structures of fibrils formed by α-synuclein hereditary disease mutant H50Q reveal new polymorphs

David R. Boyer[1,3], Binsen Li[2,3], Chuanqi Sun[2], Weijia Fan[2], Michael R. Sawaya[1], Lin Jiang[2*] and David S. Eisenberg[1*]

[1]Department of Chemistry and Biochemistry and Biological Chemistry, UCLA-DOE Institute, Molecular Biology Institute and Howard Hughes Medical Institute, UCLA, Los Angeles, CA, USA. [2]Department of Neurology, David Geffen School of Medicine, Molecular Biology Institute, UCLA, Los Angeles, CA, USA. [3]These authors contributed equally: David R. Boyer, Binsen Li. *e-mail: jianglin@ucla.edu; david@mbi.ucla.edu

Supporting Information

Supplementary Note(s):

Supplementary Note 1: Un-modeled Density Flanking Protofilament A

In Protofilament A in both the Narrow and Wide Fibril polymorphs, there are two regions of un-modeled density resembling β-strands that flank residues Q50-E57 and G36-V40 that we term Island 1 and Island 2, respectively (Figure 1 c, Extended Data Figure 4). Since we cannot unambiguously assign residues to these densities, we have made several speculative molecular models for the residues in the Islands (Extended Data Figure 4). First, for Island 2, we assume that there is likely a short, disordered region that precedes the first ordered residue of the fibril core, G36, and follows the first residue in Island 2. We noticed that G36 is preceded by sequence 32KTKE35, a repeated sequence motif in α-synuclein that forms sharp turns in other segments of the fibril. Therefore, we assume that 32KTKE35 may form a similar turn that links Island 2 to G36, and we thus modeled residues 26VAEAAG31 into Island 2 (Extended Data Figure 4 c). These residues satisfy the constraint of maintaining a tight, hydrophobic interface with residues L38 and V40 of the fibril core and demonstrate a reasonable fit into the Island 2 electron density (Extended Data Figure 4 c).

Assigning residues to Island 1 is more ambiguous as there are no close-by termini that could result in a short disordered linker region before the chain becomes ordered again at Island 1, as we believe is the case for Island 2. Therefore, we reasoned that either the residues occupying Island 1 come from Protofilament A or B (Extended Data Figure 4 a, b) or from a different chain of α-syn. The latter case would support the idea of secondary nucleation, whereby the side of an

amyloid fibril provides a template for additional molecules to become ordered and eventually form mature amyloid fibrils[16]. However, since there are too many possible residues within the entire α-syn sequence that could occupy Island 1, we decided to first make models for sequences that could come from the N-terminus of Protofilament A (in either the Narrow or Wide Fibril) or the C-terminus of Protofilament B. This is due to the fact that these two termini are positioned close enough to Island 1 to allow residues from the N- or C-terminus to account for the Island 1 density (Extended Data Figure 4 a-b, see Methods).

We identified several possible sequences from the N- or C-terminus that could account for Island 1 in Protofilament A (Extended Data Figure 4 c, see Methods). We also show several examples of sequences that were eliminated from consideration due to steric clashes, glycine residues at positions where there was obvious side chain density, or proline residues in the middle of a β-strand (Extended Data Figure 4 c). Candidate sequences include 3VFMKGLSK10, 7GLSKAKEG14, and 10KAKEGVVA17 from the N-terminus and 117PDNEAYEM124 from the C-terminus (Extended Data Figure 4 c).

We also noticed that Island 1 is located in the same region as the protofilament interface of the rod polymorph[1], perhaps suggesting that a portion of another protein chain is interacting with the preNAC residues from Protofilament A. We therefore modeled in residues from the preNAC into Island 1 in a manner similar to the wild-type rod polymorph (Extended Data Figure 6 a). We find that residues 50QGVATVA56 match the Island 1 density well and form a tight steric zipper with the preNAC residues on Protofilament A (Extended Data Figure 6 a). Energetic analysis of a model with Island 1 as residues 50QGVATVA56 and Island 2 as residues 26VAEAAG31

reveals that Protofilament A is stabilized by the presence of residues in these unmodeled densities (71.6 kcal/mol/layer with islands occupied vs. 58 kcal/mol/layer with islands empty) (Extended Data Figure 6 b). In summary, although we cannot assign unambiguously the residues that occupy Islands 1 and 2, speculative models demonstrate sequences within α-syn that can account for these densities and that the presence of these sequences in Islands 1 and 2 stabilizes Protofilament A.

Supplementary Note 2: Speculative models of inter-protofilament interfaces at the H50Q preNAC region.

To confirm that H50Q disallows assembly of protofilaments at the preNAC, we made a speculative model of two chains from Protofilament A forming a steric zipper at the preNAC, similar to the wild-type rod polymorphs (Extended Data Figure 8 c). We observe that although the wild-type residues G51-V55 form a tight homomeric steric zipper at the preNAC, H50Q clashes with E57, disfavoring the use of the preNAC as an inter-protofilament interface (Extended Data Figure 8 c). We performed the same analysis in Protofilament B where Q50 is not hydrogen bonding with K45 to examine why we do not observe a protofilament interface formed at the preNAC there. A hypothetical model where the preNAC residues of Protofilament B are used as a protofilament interface reveals that the conformation of Q50 even more severely clashes with E57 on the opposite protofilament than in the hypothetical Protofilament A model and that major clashes occur in other areas as well (Extended Data Figure 8 d). Together, these models help to explain why the preNAC region is disfavored as a protofilament interface in both Protofilaments A and B. Additionally, the severity of the clashes in the Protofilament B model

may explain why Protofilament B does not show un-modeled density flanking the preNAC region like Island 2 in Protofilament A (Figure 2 c, Extended Data Figure 8 d).

Supplementary Note 3: Differences in stabilization energies for some residues in Protofilament A and B in the Wide Fibril

The differences in stabilizing energies of some residues in the two protofilaments of the Wide Fibril may be due to differences in side chain rotamers that subsequently affect each side chain's hydrogen bonding and area buried. This is due to the asymmetry in the reconstruction whereby the two protofilaments have slightly different density maps and hence slightly different atomic models, even in the conserved kernel region. For instance, K58 and E61 have different energies in the two protofilaments of the Wide Fibril because they display slightly different hydrogen bonding patterns (Figure 4 a). Since the solvation energy of each residue is the sum of the product of the buried surface area multiplied by the atomic solvation parameter (ASP) for each of its constituent atoms and the ASP for charged atoms depends on if they are involved in a hydrogen bond, the energies for Lys58 and Glu61 can vary depending on their hydrogen bond arrangements. In other cases, such as Glu83 which is not involved in a hydrogen bond network, variation occurs between the two protofilaments because Glu83 adopts two different rotamers. The rotamer with more buried surface area will have a greater stabilization energy.

CHAPTER 4

The α-synuclein hereditary mutation E46K unlocks a more stable, pathogenic fibril structure

David R. Boyer[a,b,c,d,e,1], Binsen Li[d,f,1], Chuanqi Sun[d,f], Weijia Fan[d,f], Kang Zhou[g], Michael P. Hughes[a,b,c,d,e,2], Michael R. Sawaya[a,b,c,d,e], Lin Jiang[d,f,3], and David S. Eisenberg[a,b,c,d,e,3]

[a]Department of Chemistry and Biochemistry, University of California, Los Angeles, CA 90095; [b]Department of Biological Chemistry, University of California, Los Angeles, CA 90095; [c]Department of Energy Institute, University of California, Los Angeles, CA 90095; [d]Molecular Biology Institute, University of California, Los Angeles, CA 90095; [e]Howard Hughes Medical Institute, University of California, Los Angeles, CA 90095; [f]Department of Neurology, David Geffen School of Medicine, University of California, Los Angeles, CA 90095; and [g]California NanoSystems Institute, University of California, Los Angeles, CA 90095

Edited by William F. DeGrado, University of California, San Francisco, CA, and approved January 6, 2020 (received for review October 12, 2019)

Aggregation of α-synuclein is a defining molecular feature of Parkinson's disease, Lewy body dementia, and multiple systems atrophy. Hereditary mutations in α-synuclein are linked to both Parkinson's disease and Lewy body dementia; in particular, patients bearing the E46K disease mutation manifest a clinical picture of parkinsonism and Lewy body dementia, and E46K creates more pathogenic fibrils in vitro. Understanding the effect of these hereditary mutations on α-synuclein fibril structure is fundamental to α-synuclein biology. We therefore determined the cryo-electron microscopy (cryo-EM) structure of α-synuclein fibrils containing the hereditary E46K mutation. The 2.5-Å structure reveals a symmetric double protofilament in which the molecules adopt a vastly rearranged, lower energy fold compared to wild-type fibrils. We propose that the E46K misfolding pathway avoids electrostatic repulsion between K46 and K80, a residue pair which form the E46-K80 salt bridge in the wild-type fibril structure. We hypothesize that, under our conditions, the wild-type fold does not reach this deeper energy well of the E46K fold because the E46-K80 salt bridge diverts α-synuclein into a kinetic trap—a shallower, more accessible energy minimum. The E46K mutation apparently unlocks a more stable and pathogenic fibril structure.

α-synuclein | Parkinson's disease | Lewy body dementia | cryo-EM | hereditary mutations

The group of diseases termed the synucleinopathies—Parkinson's disease (PD), Lewy body dementia (LBD), and multiple systems atrophy (MSA)—are thought to be caused by the aggregation of α-synuclein (α-syn) into amyloid fibrils. The causal relationship between the formation of amyloid fibrils of α-syn and the synucleinopathies is supported by several observations. Aggregated α-syn is a major component of Lewy bodies, the hallmark lesion in PD and LBD, and the hallmark lesions of MSA (1, 2). Hereditary mutations in α-syn are linked to familial forms of PD and LBD (3). Overexpression of wild-type α-syn via dominantly inherited duplications and triplications of the gene that encodes α-syn, SNCA, are sufficient to cause PD (4–6). Further, the injection of fibrils of α-syn into the brains of mice induced PD-like pathology including Lewy body and Lewy neurite formation, cell-to-cell spreading of Lewy body pathology, and motor deficits similar to PD (7). Although it is never fully possible to establish causation, these combined observations suggest the case is strong for the linkage of aggregated α-syn to the synucleinopathies.

To gain a molecular level understanding of amyloid fibrils of α-syn, we previously applied cryo-electron microscopy (cryo-EM) to determine the near-atomic structures of fibrils of recombinantly assembled α-syn (9). We observed two distinct structures—termed the rod and the twister—that share a similar structural kernel formed by residues 50 to 77 but differ in their protofilament interfaces and flanking regions of the fibril core (Fig. 1*B* and *SI Appendix*, Fig. S1 *A* and *B*; also see Fig. 4 *B* and *C*). The rod and twister structures display amyloid polymorphism—the formation of distinct fibril conformations by the same protein sequence.

Amyloid polymorphism has been observed in numerous other amyloid-forming proteins, including the tau protein and amyloid-β (7, 10–12). For tau protein, the different polymorphs observed correspond to distinct diseases, namely Alzheimer's, Pick's disease, and chronic traumatic encephalopathy (7, 10, 11). Although the structures of α-syn fibrils derived from human disease brain tissue have not yet been determined, previous research has shown that fibrils derived from PD have different biochemical properties than fibrils from MSA, including differential seeding activity and cell-type origin and infectivity, that may result from the formation of distinct polymorphs in the two diseases (13). Therefore, atomic structures of fibril polymorphs are key to both basic understanding of amyloid protein structure and the development of disease-specific therapeutics.

Although hereditary mutations offer a crucial link between α-syn and disease, it is unknown how they might exert their effects. One hypothesis is that hereditary mutations may encode new structures of α-syn with enhanced pathogenicity. We note that new structures formed as the result of hereditary mutations are not true polymorphs—different structures adopted by the same protein

Significance

Parkinson's is the second most prevalent neurodegenerative condition, leading to movement disorders, and dementia in some cases. Because of the strong association of this condition with amyloid aggregates of the protein α-synuclein, structural understanding of these amyloid aggregates may be the path to eventual therapies. Our study of the structure of a variant α-synuclein inherited in families afflicted with a clinical picture of parkinsonism and Lewy body dementia supplements recent structures of the wild-type structure and shows how a single residue change can result in a greatly changed structure that may underlie the inherited form of the disease.

Author contributions: D.R.B., B.L., L.J., and D.S.E. designed research; D.R.B., B.L., W.F., and K.Z. performed research; D.R.B., B.L., C.S., M.P.H., and M.R.S. contributed new reagents/analytic tools; D.R.B., B.L., L.J., and D.S.E. analyzed data; and D.R.B., B.L., L.J., and D.S.E. wrote the paper.

Competing interest statement: D.S.E. is an advisor and equity shareholder in ADRx, Inc.

This article is a PNAS Direct Submission.

Data deposition: The cryo-EM map and model have been deposited in the Protein Data Bank, https://www.wwpdb.org/ (PDB ID code 6UFR) and the Electron Microscopy Data Bank, https://www.ebi.ac.uk/pdbe/emdb (accession no. EMD-20759).

[1]D.R.B. and B.L. contributed equally to this work.

[2]Present address: Department of Cell & Molecular Biology, St. Jude Children's Research Hospital, Memphis, TN 38105.

[3]To whom correspondence may be addressed. Email: jianglin@ucla.edu or david@mbi.ucla.edu.

This article contains supporting information online at https://www.pnas.org/lookup/suppl/doi:10.1073/pnas.1917914117/-/DCSupplemental.

First published February 3, 2020.

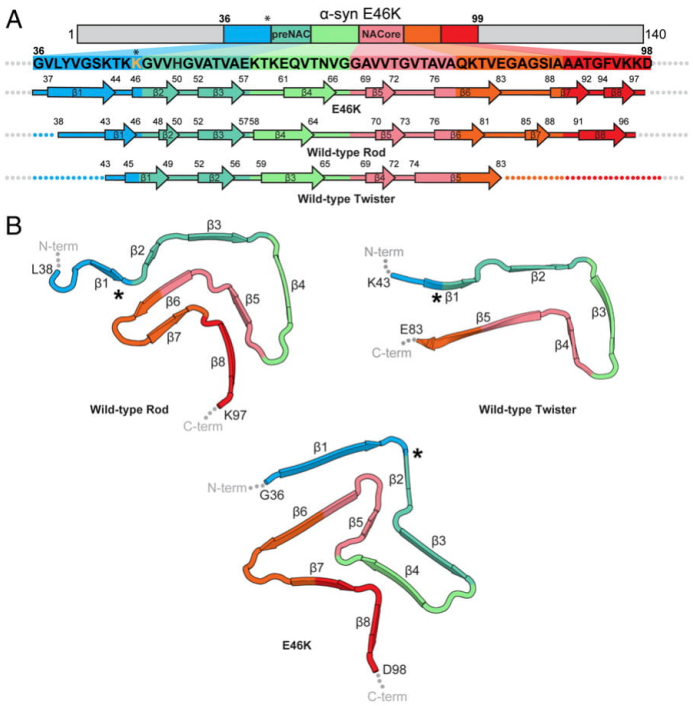

Fig. 1. The E46K mutation leads to a repacked protofilament fold. (*A*) Primary and secondary structure of α-syn wild-type and E46K fibrils. PreNAC comprises residues 47–56; NACore comprises residues 68–78 (8). Arrows indicate regions adopting β-strand conformation while other residues form loops and turns. The E46K mutation lies N-terminal to the preNAC region. (*B*) Protofilament folds of the previously determined wild-type folds (rod and twister) and E46K protofilament fold determined here (9). Asterisks indicate the location of residue 46.

sequence. Instead, we label them as "quasi-polymorphs"—different structures adopted by a protein pair with almost identical sequences.

Several hereditary mutations in α-syn may result in the formation of quasi-polymorphs. Mutations A30P, E46K, H50Q, G51D, A53E, and A53T have all been discovered to result in autosomal dominant synucleinopathies (3). Of these, E46K seems to be the only hereditary mutation that manifests in a clinical picture closer to LDB whereas other mutations are found in the context of PD, suggesting that E46K may have a unique effect on the structure of amyloid fibrils of α-syn (14). Indeed, solid state NMR studies of α-syn E46K show large chemical shift differences relative to wild-type fibrils, suggesting large scale rearrangements in the fibril structure as a result of the E46K mutation (15).

Consistent with the evidence that E46K alters α-syn fibril structure and disease manifestation, E46K has been shown to increase the pathogenicity of α-syn fibrils compared to wild-type. In vitro studies have shown that E46K results in an increase in α-syn's phospholipid binding ability and an enhancement of fibril formation (16). In addition, E46K promotes higher levels of aggregation in cultured cells relative to wild-type, A53T, and A30P α-syn (17). Further, others have found that α-syn bearing E46K is more toxic to rat primary neurons compared to wild-type, A30P, and A53T (18).

Three previous structures of full-length wild-type non-acetylated as well as three structures of acetylated full-length and C-terminally truncated α-syn reveal that E46 participates in a conserved salt bridge with K80 (*SI Appendix*, Fig. S1*A*) (9, 19–22). The E46K mutation must eliminate this salt bridge due to electrostatic repulsion that disfavors the proximity of K46 to K80, potentially leading to a different fibril structure (quasi-polymorph). A structural difference such as this may help explain the altered biochemical properties and solid state NMR (ssNMR) chemical shifts of E46K α-syn fibrils. Therefore, we sought to determine the structure of α-syn fibrils containing the E46K hereditary mutation. We find that the E46K mutation produces a homogenous sample composed of a single species whose structure differs radically from structures determined thus far. Consistent with prior studies demonstrating increased pathogenicity of E46K α-syn, we also find that E46K fibrils are more powerful seeds in α-syn HEK293T biosensor cells and more strongly impair mitochondrial activity in PC12 cells. Combining structural, energetic, and biochemical analysis, we attempt to understand the structure–function relationship of α-syn fibrils.

Results

Cryo-EM Structure Determination and Architecture of E46K α-Syn Fibrils. We purified α-syn bearing the E46K hereditary mutation and generated amyloid fibrils using the same growth conditions as in our previous studies (9). We then optimized cryo-EM grids of E46K fibrils and imaged them at 165,000× magnification on an energy-filtered Titan Krios equipped with a K2 Summit direct electron detector operating in superresolution mode. We also took advantage of image shift induced-beam tilt correction in SerialEM to maintain coma-free alignment during data collection (23). Using helical refinement procedures in Relion 3.0, we obtained a 2.5-Å resolution reconstruction of

E46K α-syn fibrils (Fig. 2 *A–E*, *SI Appendix*, Figs. S2 *A–C* and S3, and Table 1).

The high resolution allowed us to confidently assign side chain rotamer and carbonyl positions, confirming the left handedness and the internal C_2 symmetry of the helical reconstruction, and to build an unambiguous atomic model de novo (Fig. 2 *B–E*, *SI Appendix*, Fig. S3, and *Materials and Methods*). We were also able to visualize water molecules hydrogen bonded to polar and charged side chains such as threonine, serine, and lysine, as well as to backbone carbonyl oxygen atoms (Fig. 2 *D* and *E* and *SI Appendix*, Fig. S3). The atomic model reveals that the E46K fibrils are wound from two protofilaments formed by ordered residues Gly36 to Asp98 that come together at a "wet" two-fold symmetric interface formed by residues K45-E57 (Figs. 2 *B* and *C* and 3*A*).

Comparison of E46K and Wild-Type α-Syn Protofilament Folds. Overall, the E46K mutation leads to a different protofilament fold than the previously observed wild-type rod and twister structures, resulting in a quasi-polymorph of α-syn. Fig. 1 *A* and *B* compares the secondary and tertiary structure of the E46K fibril with the wild-type rod and twister. Both the rod and twister form a similar structural kernel comprised of residues 50 to 77, in which β-strands β3, β4, and β5 in the rod and β2, β3, and β4 in the twister form a bent β-arch (Fig. 2). The twister has fewer ordered residues at the N and C termini of its fibril core compared to the rod (Fig. 1 *A* and *B* and *SI Appendix*, Fig. S1). The C-terminal residues in the rod structure form a Greek key-like fold comprising β5, β6, β7, and β8. However, in the E46K structure, the kernel and Greek key are not maintained, and a different packing arrangement is formed. This is likely due to the E46K mutation disrupting the wild-type E46-K80 salt bridge, allowing a rearrangement of the backbone (Fig. 2*B*). Interestingly, K80 is now buried in the fibril core although we visualize an ordered molecule binding to the primary amine of the K80 side chain, suggesting that an extensive hydrogen bond network may help to counteract the apparent unfavorable placement of this polar, charged residue within the fibril core. Without the constraint of the E46-K80 salt bridge, a different set of residues form sheet–sheet interfaces within the protofilament (Fig. 2). Now tightly mated heterozippers are formed by β-strands β1 and β6, β3 and β4, and a roughly triangular-shaped bent β-arch fold is formed by β4, β5, β6, and β7 (Fig. 1).

SI Appendix, Fig. S4 *A–C* helps to visualize the changes in interacting residues among the structures by displaying all pairwise interactions found within the protofilaments of wild-type and E46K quasi-polymorphs. This analysis of pairwise interactions not only codifies the differences in sets of interacting residues between the wild-type and E46K structures but also clearly reveals that the E46K structure has more interacting residues than its wild-type counterparts. Correspondingly, each chain within the E46K protofilament has a greater buried surface area than wild-type structures (7,944 $Å^2$ for E46K; 7,605 $Å^2$ for wild-type rod; 5,082 $Å^2$ for wild-type twister). In line with this observation, energetic analysis indicates that the E46K structure has a lower standard free energy (greater stabilization) than wild-type structures (*SI Appendix*, Fig. S1 *A–C* and Table 2). To verify the energy estimate, we performed a sodium dodecyl sulfate (SDS) denaturation assay where both wild-type and E46K fibrils were incubated with various concentrations of SDS at 37 °C followed by thioflavin-T (ThT) fluorescence measurements. Our results demonstrate that E46K fibrils are more resistant to chemical denaturation than wild-type fibrils, consistent with our energetic calculation suggesting that E46K fibrils are more stable than wild-type fibrils (*SI Appendix*, Fig. S5*B*).

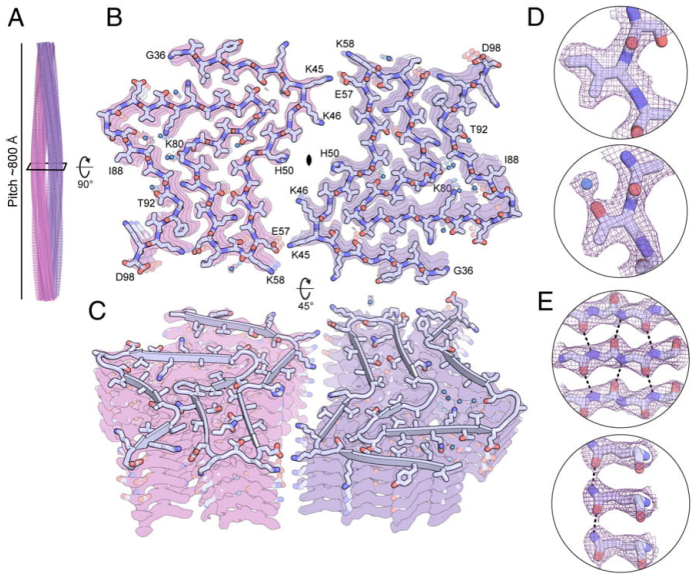

Fig. 2. Overview of E46K cryo-EM structure. (*A*) E46K fibril side view demonstrating a pitch of ~800 Å. (*B*) Cross-sectional view of one layer of the E46K fibril. The fibril is wound from two identical protofilaments related by a two-fold rotational symmetry axis. The E46K protofilament contains ordered residues 36 to 98. (*C*) Tilted view of E46K fibril cross-section demonstrating the stacking of identical layers. (*D* and *E*) Representative side chain and backbone densities highlight resolution of reconstruction and good map-to-model agreement. (*D*) Coulombic potential map of Ile88 and Thr92. An ordered water molecule is bound to the oxygen of the threonine side chain. (*E*) Coulombic potential map of representative backbone (Gln79-Val82) and side chain amide hydrogen bonding (Gln62).

Table 1. Cryo-EM data collection, refinement, and validation statistics

Name	E46K α-syn
PDB ID	6UFR
EMDB ID	EMD-20759
Data collection	
Magnification	×165,000
Defocus range, μm	0.75–3.37
Voltage, kV	300
Camera	K2 summit (quantum LS)
Frame exposure time, s	0.2
No. of movie frames	30
Total electron dose, $e^{-}/Å^2$	36
Pixel size, Å	0.838
Reconstruction	
Box size, pixels	400
Interbox distance, Å	33.5
No. of micrographs collected	3,078
No. of segments extracted	210,593
No. of segments after Class2D	N/A
No. of segments after Class3D	114,260
Resolution, Å	2.5
Map sharpening B-factor, $Å^2$	−140
Helical rise, Å	4.85
Helical twist, °	178.92
Point group	C_2
Atomic model	
No. of nonhydrogen atoms	4330
No. of protein residues	630
rmsd bonds, Å	0.012
rmsd angles, °	0.958
Molprobity clashscore, all atoms	4.36
Molprobity score	1.64
Poor rotamers, %	0
Ramachandran outliers, %	0
Ramachandran allowed, %	6.6
Ramachandran favored, %	93.4
Cβ deviations > 0.25 Å, %	0
Bad bonds, %	0
Bad angles, %	0

Information for number of segments after Class2D is not available as only Class3D was performed for 400 pixel box segments (*Materials and Methods*)

A key difference between E46K and wild-type structures is their pattern of electrostatic interactions. The E46K fibril core has a greater number of charged pairs (interacting pairs of glutamate and lysine), creating a more balanced set of electrostatic interactions despite having a higher net charge than the wild-type fibrils (Fig. 3 *A*–*C*). This results from the E46K structure containing four electrostatic triads per layer featuring residues K45-E57-K58 and K60-E61-K96 while the wild-type rod and twister structures both contain only two electrostatic zippers featuring residues E46-K80 and E57-K58, respectively (Fig. 3 *A*–*C*). Therefore, in line with the observation above that the E46K structure has overall more interresidue contacts, a higher buried surface area, and a lower free energy than wild-type, it also has a richer set of electrostatic interactions.

Interestingly, although the wild-type and E46K structures differ, many residues adopt similar secondary structures. For instance, β-strand interrupting loops and turns are formed by KTKE pseudorepeats (residues 43 to 46, 58 to 61, and 80 to 83) and glycines (residues 51, 67 to 68, 73, 84, and 93) while other residues form β-strands (Fig. 1 *A* and *B*). Indeed, if one compares the structures in Fig. 1*B*, especially the wild-type rod and E46K, loops and turns between β-strands often lead to a similar change in chain direction. For example, turns between β3 and β4 (right turn), β4 and β5 (right turn), β5 and β6 (left turn), β6 and β7 (left turn), and β7 and β8 (right turn) change the chain in generally similar manners. However, there are differences in the extent and radii of the turns that generate the structural diversity seen in the structures. For instance, the turn between β3 and β4 leads to an ∼90° turn in the rod and an ∼180° turn in the E46K structure. Also, the turn between β4 and β5 leads to an ∼180° turn in the rod and an ∼100° turn in the E46K structure. These observations highlight the critical importance of turn and loop regions in generating amyloid polymorphism.

Electrostatic Zippers Constitute the E46K Protofilament Interface. Despite having a tighter protofilament fold that buries more surface area, the interface between E46K protofilaments contains fewer contacts than those in the wild-type rod and twister structures (Fig. 4 *A*–*C*). Instead of the two protofilaments meeting at a classical steric zipper interface in which beta-sheets from each protofilament tightly mate with interdigitating side chains excluding water, the E46K structure forms a largely solvent-filled interface spanning residues 45 to 57 (buried surface area = 47.3 $Å^2$). This is in contrast to the dry, steric zipper-like interfaces formed by the preNAC (residues 47–56, buried surface area = 91.7 $Å^2$) and NAC (residues 68–78, buried surface area = 65.3 $Å^2$) residues in the wild-type rod and twister, respectively. Although most residues are too far apart to interact in the E46K interface, two electrostatic zippers form on either side of the interface (Fig. 4*A*). Electrostatic zippers have previously been observed to enable counterion-induced DNA condensation whereby anionic phosphates and cations such as Mn^{2+} and spermidines alternate along the length of the DNA–DNA interface forming a "zipper" that "fastens" the molecules together (24). In the E46K protofilament interface, electrostatic zippers consist of carboxylate anions of E57 interleaving with the K45 side chain aminium cations, fastening the two protofilaments together (Fig. 4*A*). This interaction is not only repeated twice per protofilament interface due to the two-fold helical symmetry but extends for thousands of layers along the fibril axis. We note that the staggered nature of the electrostatic zipper leaves unpaired charges on both the top and bottom of the fibril, potentially attracting additional monomers to add to the fibril through long-range electrostatic interactions. We also observe that no single protofilaments were detected during class averaging, indicating that, despite its relative lack of interactions across the protofilament, the E46K interface is apparently strong enough to consistently bind together the two protofilaments of the fibril.

E46K Fibrils Are More Pathogenic than Wild-Type. We wondered if the differences in structure between the E46K and wild-type fibrils resulted in differences in biochemical properties. Therefore, we first examined the ability of sonicated E46K and wild-type fibrils to seed endogenously expressed α-syn-A53T-YFP in HEK293T biosensor cells (25). If seeding occurs, normally diffuse α-syn-A53T-YFP will aggregate into discrete puncta, which can be counted and used as a robust measure of seeding. Our results indicate that, at most concentrations tested, E46K fibrils are significantly more powerful seeds than wild-type fibrils (Fig. 5*A*). Whereas the biosensor cell assay supports that E46K fibrils are better seeds than wild-type fibrils, the biosensor cells express α-syn-A53T-YFP, and not wild-type α-syn. In addition, differences in lipofectamine uptake may influence which fibril species is able to induce more seeding in the biosensor cell assay. Therefore, in order to directly examine whether E46K fibrils can seed wild-type protein more strongly than wild-type fibrils, we next tested the seeding ability of E46K fibrils in an in vitro assay (*SI Appendix*, Fig. S5*A*). Similar to the biosensor cell assay, E46K fibrils were more efficient than wild-type fibrils in seeding growth of wild-type α-syn (*SI Appendix*, Fig. S5*A*). Further, the different

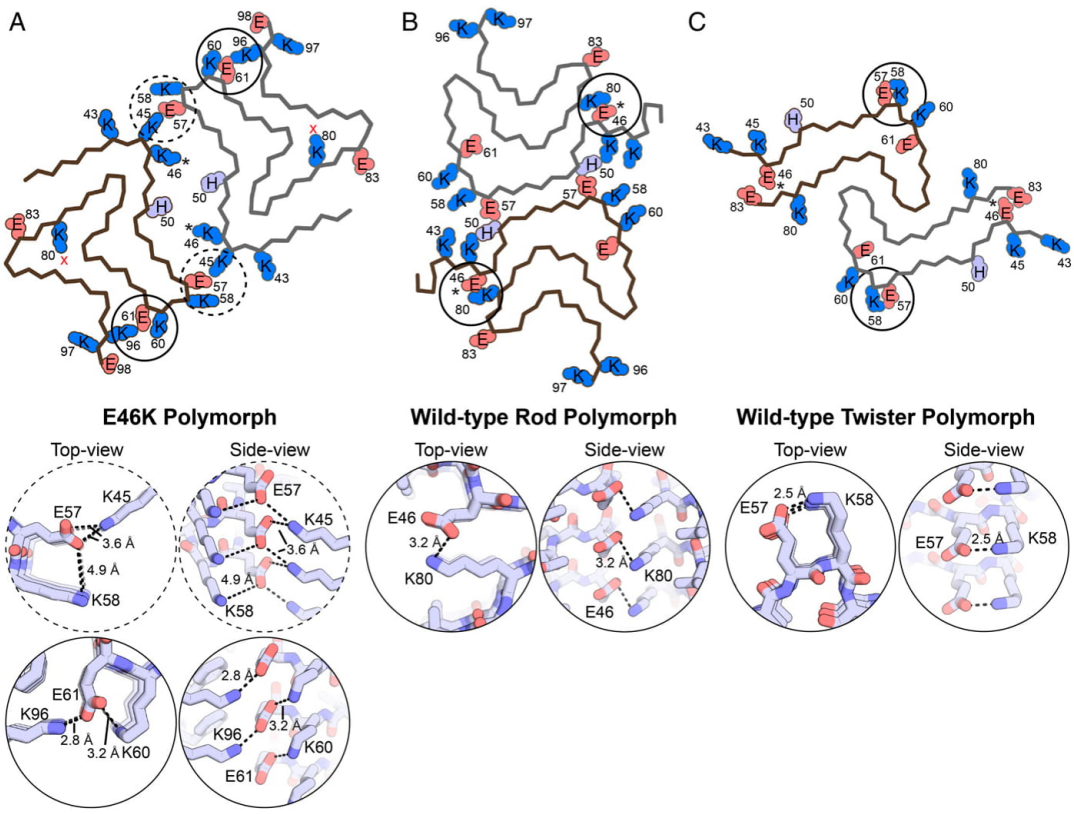

Fig. 3. Electrostatic residues and interactions of wild-type and E46K fibrils. (*A*) Overview of E46K quasi-polymorph fold with charged and ionizable residues shown (*Top*). Top and side view of the K45-E57-K58 and K60-E61-K96 electrostatic triads (*Bottom*). The E46K fibril core has a net charge of +11 per layer (2 × 8 lysine per chain + 2 × 1/2 histidine per chain − 2 × 3 glutamate per chain) and eight charged pairs per layer (2 × K45-E57 + 2 × E57-E58 + 2 × K60-E61 + 2 × E61-K96). (*B*) Overview of the wild-type rod polymorph fold with charged and ionizable residues shown (*Top*). Top and side view of the E46-K80 salt bridge (*Bottom*). The wild-type rod fibril core has a net charge of +7 per layer (2 × 7 lysine per chain + 2 × 1/2 histidine per chain − 2 × 4 glutamate per chain) and two charge pairs per layer (2 × E46-K80 per chain). (*C*) Overview of wild-type twister polymorph fold with charged and ionizable residues shown (*Top*). Top and side view of the E57-K80 salt bridge (*Bottom*). The wild-type twister fibril core has a net charge of +3 per layer (2 × 5 lysine per chain + 2 × 1/2 histidine per chain − 2 × 4 glutamate per chain) and two charge pairs per layer (2 × E57-K58 per chain). Asterisks denote the location of residue 46. A red x denotes the location of the ordered water molecules hydrogen bonding to K80 in the E46K structure.

ThT binding ability of wild-type fibrils either grown without seeds or with wild-type seeds compared to wild-type fibrils seeded by E46K fibrils suggests that seeding by E46K fibrils can induce a different wild-type fibril structure, possibly one similar to the E46K fibril structure (*SI Appendix*, Fig. S5*A*). This is similar to what is seen in Watson and Lee where both non-acetylated and acetylated α-syn form fibrils to the same extent, yet acetylated α-syn has a substantially lower ThT signal (26). We also observe that unseeded E46K has a longer lag phase than unseeded wild-type α-syn; we speculate why E46K may form fibrils more slowly than wild-type in *Discussion*.

We next compared the ability of E46K and wild-type fibrils to impair mitochondrial activity of differentiated neuron-like rat pheochromocytoma (PC12) cells as a proxy for comparing cytotoxicities (27, 28). We observe significantly impaired mitochondrial activity by lower concentrations of E46K fibrils than of wild-type fibrils (Fig. 5*B*). Consistent with previous results showing increased aggregation in SH-SY5Y cultured cells, and higher toxicity to rat primary neurons, our results indicate that the structure formed by E46K fibrils is more pathogenic than wild-type (16–18).

Discussion

Structural Differences Help Explain Enhanced Pathogenicity of E46K α-Syn Fibrils. The structural differences between E46K and wild-type fibrils help rationalize the differences in biochemical properties we observe. First, we have shown an increased seeding efficiency of E46K fibrils compared to wild-type in HEK293T biosensor cells and in vitro (Fig. 5*A* and *SI Appendix*, Fig. S5*A*). This difference may arise from the stronger electrostatic templating mechanism of E46K fibrils than wild-type fibrils: There are four electrostatic triads per layer in the E46K fibril structure compared to two E46-K80 salt bridges in the wild-type rod structure and two E57-K80 salt bridges in the wild-type twister structure, and each one of them forms a staggered electrostatic zipper, with overhanging, unsatisfied charges (Fig. 3 *A* and *C*). Since all of these electrostatic residues are present in the α-syn-A53T-YFP construct in the biosensor cells and in wild-type α-syn

Table 2. Comparative solvation energies

Fibril structure	Atomic solvation standard free energy of stabilization, kcal/mol		
	Per layer	Per chain	Per residue
E46K	−73.8	−36.9	−0.59
WT cryo-EM rod (6CU7)	−59.6	−29.3	−0.49
WT cryo-EM twister (6CU8)	−25.0	−12.5	−0.30
Tau PHF (530L)	−62.8	−31.4	−0.43
Tau pick's (6GX5)	−44.8	−44.8	−0.48
Tau CTE type I (6NWP)	−67.4	−33.7	−0.48
TDP-43 SegA-sym (6N37)	−34.2	−17.1	−0.47
Serum amyloid A (6MST)	−68.8	−34.4	−0.65
FUS (5W3N)	−12.2	−12.2	−0.20

used in the in vitro assay, it is plausible that the electrostatic triads in the E46K fibril guide α-syn monomers to the ends of E46K fibrils through long-range electrostatic attraction. Second, the E46K fibril has a different set of ordered surfaces than wild-type fibrils, which may lead to a different set of interacting partners in the cellular milieu. It has previously been shown that aggregates of polyQ can siphon essential proteins into amyloid inclusions and that overexpression of these essential proteins can help alleviate toxicity and reduce aggregate size, presumably by rendering fibrils inert by coating their surface (29). In this way, the different ordered surfaces of E46K fibrils may interact more strongly than wild-type fibrils with certain essential proteins in the cell (for instance, those involved in mitochondrial homeostasis), and this may help to explain the greater reduction in mitochondrial activity we observe (Fig. 5*B*).

Amyloid Polymorphism. The differences in biological activity associated with structural differences between mutant and wild-type fibrils highlight the relevance of amyloid polymorphism to disease. Hereditary mutations may represent one important influence over the formation of different amyloid polymorphs. Here, we learn that the E46K hereditary mutation leads to a distinct α-syn quasi-polymorph by facilitating a large rearrangement in fibril structure, including a repacked protofilament fold and a protofilament interface. Furthermore, additional recent cryo-EM studies have captured yet another quasi-polymorph of E46K α-synuclein fibrils, which is different still from our own E46K fibril structure (30). The polymorphism displayed by E46K is reminiscent of modal polymorphism, first introduced by Caspar and Cohen (31), whereby identical units have different dispositions in different assemblies (in other words, two fibril structures of the same protein adopt different structures). Although wild-type and E46K fibrils are not strictly modal polymorphs because of the difference in sequence at one amino acid position and hence we refer to them as quasi-polymorphs, it has recently been shown that, under different buffer conditions from our own, the wild-type sequence can indeed form a structure—termed polymorph 2a—similar to the E46K structure determined here (32). This is consistent with the solvent-facing orientation of side chain 46 in the E46K structure, thereby compatible with either the negatively charged wild-type glutamate or the positively charged mutant lysine.

The vast difference in structure between the wild-type and E46K fibrils due to a change at a single amino acid position, or a change in fibril growth buffer conditions (32), highlights the large degree of sensitivity of α-syn fibril assembly to certain interactions. This vulnerability to large-scale rearrangements due to small changes in protein sequence or fibril growth environment reveals that the fibril misfolding landscape for α-syn is flat with many local minima (33). Here, a single amino acid change, the E46K mutation, shifts the fibril misfolding pathway of α-syn to a different minimum in the folding landscape. Energetic analysis reveals that the E46K quasi-polymorph is significantly more stable than the wild-type folds (−0.59 kcal/mol/residue for E46K vs. −0.49 kcal/mol/residue for wild-type rod and −0.30 kcal/mol/residue for wild-type twister) (Table 1). This calculation, along with the fact that the wild-type sequence has been shown to be able to adopt the E46K structure (32), prompts the question why the wild-type sequence does not always form the more stable E46K structure?

Kinetic Factors That Influence Amyloid Structure. The predominance of one amyloid polymorph over another depends on stochastic nucleation events and kinetically driven growth processes, permitting less stable polymorphs in a sample to dominate if they form and replicate quicker than more stable polymorphs (34). We hypothesize that the formation of the E46-K80 salt bridge observed in all structures of the wild-type rod polymorph determined thus far is an early event in the fibril formation pathway, occurring in the transition state between prefibrillar and fibrillary structures, that lowers the energy barrier to forming the rod structure (9, 19, 20). In other words, the early formation of the E46-K80 salt bridge may divert α-syn into a kinetic trap. By constraining the residues connecting Glu46 and Lys80 to adopt a specific conformation that allows Glu46 and Lys80 to maintain their proximity, the E46-K80 salt bridge shifts the misfolding pathway away from the E46K structure and toward the rod structure, thus enforcing the formation of the less stable structure. This salt bridge could be one contributing factor to the observation of the similar kernels formed by residues 50 to 77 observed in wild-type rod structures (9, 19, 20). The mutation of residue 46 to lysine via the E46K hereditary mutation eliminates the potential to form the E46-K80 salt bridge. This raises the energy barrier to forming the rod and diverts α-syn to a different misfolding pathway, resulting in the more energetically stable E46K structure. These ideas are summarized in Fig. 6, which imagines the misfolding landscape of the α-syn rod and E46K quasi-polymorphs (we label the structure on the right the "compact" polymorph in order to avoid confusion as both E46K and other sequences could adopt this fold). This folding landscape is also consistent with our results that E46K α-syn aggregates more slowly than wild-type (*SI Appendix*, Fig. S5*A*) given that the transition state for the wild-type sequence to form the rod structure is predicted to be lower than the transition state for the E46K sequence to form the compact polymorph (Fig. 6).

To date, no other studies of wild-type or mutant α-syn have revealed the twister polymorph we determined in our initial cryo-EM study (9). It is especially surprising that E46K α-syn does not form the twister structure given that it was predicted that E46K would result in a favorable interaction with E83 in the twister conformation (9). We speculate that—given the role of kinetics in selecting amyloid polymorphs—the twister polymorph may be the result of a stochastic nucleation event leading to a rare fibril polymorph. Therefore, the twister structure may not be easily reproducible when mutations are added or buffer conditions (influence of fibril growth conditions discussed below) are changed, thereby providing an explanation for why we and others have not recapitulated the twister structure in more recent studies.

Growth Conditions That Influence Amyloid Structure. That the wild-type sequence can also adopt the E46K fold adds complexity to the argument that the formation of the E46-K80 salt bridge is an early event in fibril formation that determines the resulting fibril structure (32). Clearly, there are other factors at play. One such consideration is the role of the fibril growth environment. Guerrero-Ferreira et al. note that the juxtaposition of multiple positively charged lysines at positions 43, 45, and 58 seen in the wild-type rod structures may be allowed only in the presence of poly-anionic counter charges, such as phosphate (32). They

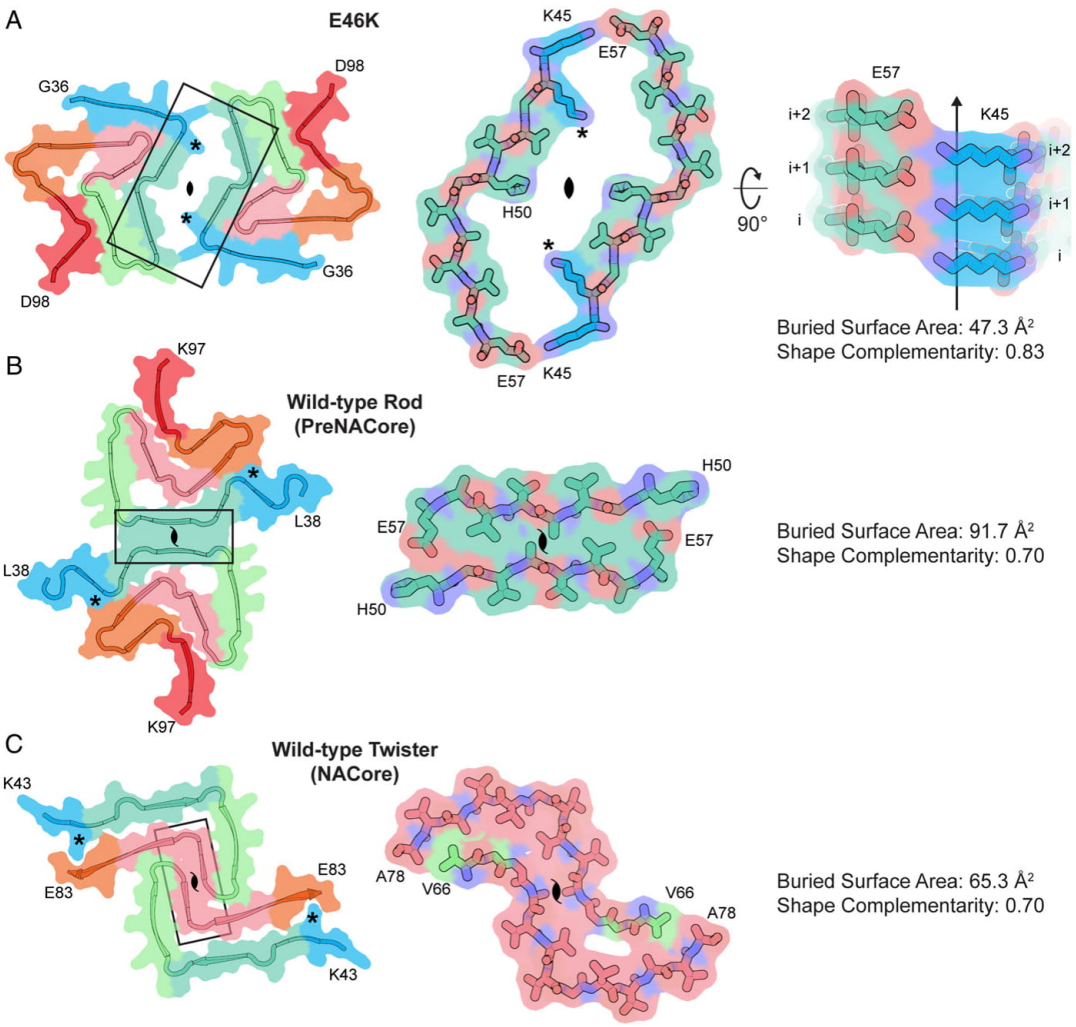

Fig. 4. Comparison of protofilament interfaces of E46K and wild-type fibrils. (*A*) The E46K quasi-polymorph forms a two-fold symmetric protofilament interface comprised of residues Lys45-Glu57. The interface is largely solvent-filled and is held together by electrostatic interaction of Lys45 and Glu57 at both ends of the interface. The Lys45-Glu57 salt bridge is repeated along the length of the fibril, creating an electrostatic zipper. (*B*) The wild-type rod polymorph forms a pseudo-2_1 symmetric dry steric zipper interface comprised of residues His50-E57 from the preNAC region (residues 47–56). (*C*) The wild-type twister polymorph forms a pseudo-2_1 symmetric dry steric zipper interface comprised of residues Val66-Ala78 from the NACore (residues 68–78). In all panels, the single asterisk indicates the location of residue 46.

observe that the removal of phosphate from the buffer conditions disallows this juxtaposition of lysine residues, facilitating the formation of the E46K-like polymorph they term 2a. This finding emphasizes again the sensitivity of α-syn fibril structure to perturbations in sequence or growth environment and that both of these factors play a role in producing varied folds. Further, our cross-seeding experiments demonstrating that E46K fibrils can seed wild-type monomer and the fact that the resulting fibrils have different ThT binding ability compared to unseeded wild-type—indicative of a different underlying structure—suggests that the E46-K80 salt bridge can also be disrupted by templated aggregation with seeds of a different structure (*SI Appendix*, Fig. S5*A*). Together, these findings indicate that the force exerted by the E46-K80 salt bridge is relatively small and can be overcome by different buffer conditions or templated aggregation. However, these small forces have a large influence in selecting the polymorph because they are exerted early in the aggregation pathway.

Interestingly, Guerrero-Ferreira et al. also reconstruct a low-resolution density map of E46K α-syn grown in phosphate buffer that resembles the 2a polymorph and our E46K structure determined here (32). This is identical to the buffer they used previously to grow fibrils of wild-type, C-terminally truncated α-syn that produced a rod polymorph similar to the one we determined

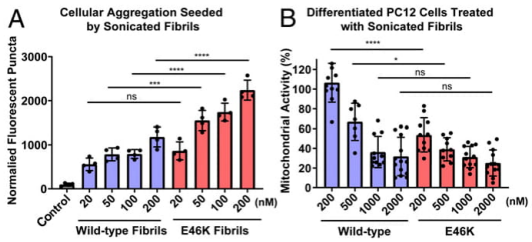

Fig. 5. Biochemical analysis of E46K vs. wild-type fibrils. (*A*) Fibrils of E46K and wild-type α-syn were sonicated and transfected into HEK293T α-syn-A53T-YFP biosensor cells, and aggregation is measured by the normally soluble and diffuse intracellular α-syn-A53T-YFP forming discrete puncta, which are then quantified through fluorescent image analysis (25). At all concentrations but 20 nM, E46K fibrils are significantly more powerful seeds than wild-type fibrils. Error bars represent the SD of four technical replicates. (*B*) In order to assay the toxicity of E46K and wild-type fibrils, we treated PC12 cells with sonicated fibrils and measured mitochondrial activity with an MTT assay (27, 28). E46K fibrils require a lower concentration to significantly impair mitochondrial activity compared to wild-type fibrils. Error bars represent the SD of 7 to 14 technical replicates. ****P value $\leq$ 0.0001. ***P value $\leq$ 0.001 *P value $\leq$ 0.05 ns, P value $>$ 0.05. P values were calculated using an unpaired, two-tailed t test with a 95% CI.

(9, 19). This is similar to the case we describe here in which we grow E46K fibrils using identical buffer conditions as those used to grow fibrils of the wild-type rod polymorph, and the E46K mutation results in a different fold. Taking these results together, this implies that, under identical buffer conditions, E46K acts as a switch to shift the fibril folding pathway, likely through the disruption of the E46-K80 kinetic trap discussed above, thereby unlocking a more stable polymorph.

Initial studies examining the effect of the E46K mutation on recombinantly assembled α-syn fibrils further emphasize the importance of fibril growth conditions on selecting polymorphs. Whereas we find that E46K α-syn forms fibrils more slowly than wild-type α-syn (*SI Appendix*, Fig. S5*A*), Choi et al. found that the E46K mutation accelerates α-syn fibril formation (16). However, the fibrils formed in their study appear to have a different morphology than our E46K fibrils (16). Specifically, the E46K fibrils prepared under their conditions have a faster twist and greater variation in width along the fibril, indicative of a different underlying molecular structure. This distinction is most likely due to the differences in buffer conditions between our two preparations: Choi et al. (16) grew their fibrils in Mops buffer whereas we grow our fibrils in water and tetrabutylphosphonium bromide, a fibrillation agent we identified in our initial screening to identify wild-type fibrils suitable for cryo-EM structure determination (9). The observed differences in fibril morphology and aggregation kinetics again highlight the sensitivity of α-syn fibrillation to growth conditions and hints at the ability of E46K α-syn to form still further polymorphs not determined in this work.

The Folding Landscape of Amyloid Proteins. As mentioned above, amyloid polymorphism is likely due to a flat protein folding landscape in which many local minima exist. This landscape contrasts with that of most proteins whose sequences have evolved to encode one structure with the lowest free energy in a funnel-shaped protein folding landscape (33, 35). The prodigious polymorphism observed not only in α-syn structures determined in our work but in other amyloid structures hints that evolution

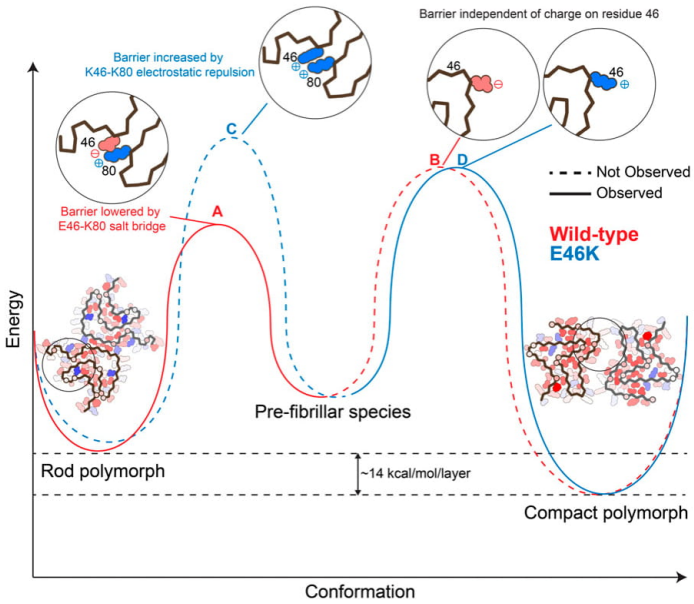

Fig. 6. Proposed misfolding landscape of α-syn rod and compact polymorphs. The E46-K80 salt bridge of the wild-type sequence (*A*) lowers the transition-state barrier to the rod polymorph. Thus the salt bridge kinetically favors formation of the rod polymorph, rather than the hypothetical, compact wild-type structure (*B*). That is, the compact polymorph we observe here is not observed for the wild-type sequence because the E46-K80 salt bridge acts as a kinetic trap, diverting the sequence to fold into the rod structure. The E46K mutation thereby serves to raise the transition state energy of forming the rod polymorph via electrostatic repulsion between K46-K80 (*C*), thus facilitating the formation of the compact polymorph (*D*).

has not played a role in specifying pathogenic amyloid structures. Therefore, many factors, such as concentration and intrachain interactions, may guide the sequence to forming a nonevolved structure. The E46-K80 salt bridge may represent one of these intrachain interactions that diverts wild-type α-syn into a local energy minimum (i.e., a kinetic trap), and the E46K hereditary mutation unlocks this constraint, allowing a more stable structure to form.

The release of local constraints leading to lower free energy structures could be a mechanism by which other hereditary mutations operate as well. This hypothesis is in line with our previous studies showing that pathogenic mutations and posttranslational modifications can lead to more stable amyloid assemblies (36–38). That work was done on shorter peptide segments, however, and may not have captured all of the interactions present in a full-length amyloid fibril. Therefore, future work is needed to compare structures of full-length wild-type and hereditary mutant or posttranslationally modified amyloid fibrils to identify the possible mechanisms by which hereditary mutations and posttranslational modifications (PTMs) can alter amyloid protein pathogenicity. We have previously shown that the H50Q hereditary mutation alters α-syn's protofilament assembly, resulting in more pathogenic fibrils—a first step in understanding the role of hereditary mutations in fibril structure and activity (39). Recently, a pair of studies demonstrated that N-terminally acetylated α-syn has different ThT binding ability and different seeding properties compared to nonacetylated α-syn although the structures of nonacetylated and acetylated α-syn fibril cores remain largely similar (21, 26). Further, ssNMR studies of α-syn hereditary mutants A30P, which lies outside the fibril core of α-syn structures determined to date, and A53T, which lies at the protofilament interface of wild-type rod polymorphs, suggest only local perturbations compared to the wild-type fibril structure (15, 40). Also, hereditary mutations in transthyretin have been discovered that serve to destabilize transthyretin's native fold, thereby promoting fibril formation (41). Together, these data indicate that other modes of mutationally or PTM-encoded pathogenicity may exist, including effects localized to regions outside the fibril core or effects on the monomeric protein structure. Indeed, PTMs such as phosphorylation, oxidative stress, and truncation, have varying effects on α-syn aggregation and toxicity (42).

Conclusion

In summary, we have determined a 2.5-Å resolution reconstruction of recombinantly assembled E46K α-syn fibrils that provides the atomic structure of this hereditary mutation initially discovered in a family with a clinical diagnosis of parkinsonism and Lewy body dementia (14). The fibril structure of E46K α-syn greatly differs from, and has a lower free energy than, wild-type structures, and we attempt to use the structure to rationalize its higher seeding capacity and mitochondrial impairment compared to wild-type. We posit that, due to fibril α-syn's unevolved nature, the E46-K80 salt bridge in wild-type fibrils represents a local constraint that prevents the formation of the lower free energy fibril fold; E46K alleviates this constraint, allowing refolding to a more stable structure. The release of local constraints to allow repacking into more stable, pathogenic fibrils may be a mechanism by which other hereditary mutations operate in α-syn and other amyloid proteins.

Materials and Methods

Protein Purification. Full-length α-syn wild-type and E46K mutant proteins were expressed and purified according to a published protocol (9). Transformed bacteria were induced at an OD600 of ∼0.6 with 1 mM IPTG for 6 h at 30 °C. The bacteria were then lysed with a probe sonicator for 10 min in an iced water bath. After centrifugation, the soluble fraction was heated in boiling water for 10 min and then titrated with HCl to pH 4.5 to remove the pellet. After adjusting to neutral pH, the protein was dialyzed overnight against Q Column loading buffer (20 mM Tris·HCl, pH 8.0). On the next day, the protein was loaded onto a HiPrep Q 16/10 column and eluted using elution buffer (20 mM Tris·HCl, 1 M NaCl, pH 8.0). The eluent was concentrated using Amicon Ultra-15 centrifugal filters (10 NMWL; Millipore Sigma) to ∼5 mL The concentrated sample was further purified with size-exclusion chromatography through a HiPrep Sephacryl S-75 HR column in 20 mM Tris, pH 8.0. The purified protein was dialyzed against water, concentrated to 3 mg/mL, and stored at 4 °C. The concentration of the protein was determined using the Pierce BCA Protein Assay Kit (cat. No. 23225; Thermo Fisher Scientific).

Fibril Preparation and Optimization. Both wild-type and E46K fibrils were grown under the same condition: 300 μM purified monomers, 15 mM tetrabutylphosphonium bromide, shaking at 37 °C for 2 wk.

Fibril Seeding Aggregation in Cells. We performed the biosensor cell seeding assay based on a previously published protocol (25). Briefly, the assay works as follows: Exogenous, unlabeled fibrils are transfected into HEK293T cells expressing α-syn-A53T-YFP. Seeded aggregation of endogenously expressed α-syn-A53T-YFP is monitored by formation of fluorescent puncta. The puncta represent intracellular aggregation of α-syn-A53T-YFP as a result of seeding by exogenous E46K or wild-type fibrils.

Human embryonic kidney FRET Biosensor HEK293T cells expressing full-length α-syn containing the hereditary A53T mutation were grown in DMEM (4 mM L-glutamine and 25 mM D-glucose) supplemented with 10% fetal bovine serum (FBS), 1% penicillin/streptomycin. Trypsin-treated HEK293T cells were harvested, seeded on flat 96-well plates at a concentration of 4×104 cells per well in 200 μL of culture medium per well and incubated in 5% CO_2 at 37 °C for 18 h.

α-syn fibrils were prepared by diluting with Opti-MEM (Life Technologies, Carlsbad, CA) and sonicating in a water bath sonicator for 10 min. Fibril concentration was determined as monomer-equivalent concentration. The fibril samples were then mixed with Lipofectamine 2000 (Thermo Fisher Scientific) and incubated for 15 min and then added to the cells. The actual volume of Lipofectamine 2000 was calculated based on the dose of 1 μL per well. After 48 h of transfection, the cells were trypsinized, transferred to a 96-well round-bottom plate, and resuspended in 200 μL of chilled flow cytometry buffer (HBSS, 1% FBS, and 1 mM EDTA) containing 2% paraformaldehyde. The plate was sealed with Parafilm and stored at 4 °C for imaging. Fluorescent images were processed in ImageJ to count number of seeded cells.

Mitochondrial Activity Assay. The addition of sonicated fibrils to nerve growth factor-differentiated PC12 cells is a well-established assay to measure cytotoxicity of amyloid fibrils (9, 27, 28, 39). Use of this neuron-like cell line allows us to obtain a biologically relevant assay for cytotoxicity. For our MTT (3-(4, 5-dimethylthiazolyl-2)-2, 5-diphenyltetrazolium bromide) mitochondrial activity assay, the protocol was adapted from the Provost and Wallert laboratories and was performed in an identical manner to our previous work (39, 43). Thiazolyl blue tetrazolium bromide for the MTT cell toxicity assay was purchased from Millipore Sigma (M2128-1G; Burlington, MA). PC12 cells were plated in 96-well plates at 10,000 cells per well in DMEM (Dulbecco's modification of Eagle's medium; 5% fetal bovine serum, 5% heat-inactivated horse serum, 1% penicillin/streptomycin, and 150 ng/mL nerve growild-typeh factor 2.5S [Thermo Fisher Scientific]). The cells were incubated for 2 d in an incubator with 5% CO_2 at 37 °C. The cells were treated with different concentrations of monomer-equivalent α-syn fibrils (200 nM, 500 nM, 1,000 nM, and 2,000 nM). After 18 h of incubation, 20 μL of 5 mg/mL MTT was added to every well, and the plate was returned to the incubator for 3.5 h. With the presence of MTT, the experiment was conducted in a laminar flow hood with the lights off, and the plate was wrapped in aluminum foil. The media was then removed with an aspirator, and the remaining formazan crystals in each well were dissolved with 100 μL of 100% DMSO. Absorbance was measured at 570 nm to determine the MTT signal and at 630 nm to determine background. The data were normalized to those from cells treated with 1% SDS to obtain a value of 0%, and to those from cells treated with PBS to obtain a value of 100%.

In Vitro Aggregation and Seeding Assay. α-syn wild-type or E46K monomers (100 μM) were mixed with 60 μM thioflavin-T (ThT) and transferred into a 96-well plate. The signal was monitored using the FLUOstar Omega Microplate Reader (37 °C with 600 rpm double orbital shaking, ex. 440 nm, em. 490 nm; BMG Labtech). For the seeding groups, preformed wild-type or E46K fibrils

(10 μM) after 10 min of water-bath sonication were added to the wild-type α-syn monomers immediately before beginning the aggregation assay.

SDS Stability Assay. The wild-type and E46K aggregated α-syn samples at the end of the ThT assay were treated with addition of 10% SDS to reach SDS final concentration of 0.5%. The ThT signal was measured after 5 min of incubation at 37 °C with 600 rpm double orbital shaking. The addition of SDS and ThT measurement was repeated with increments of 0.5% to a final SDS concentration of 3.5%. The initial ThT signals at 0% SDS were used for normalization.

Cryo-EM Data Collection and Processing. Two microliters of fibril solution was applied to a baked and glow-discharged Quantifoil 1.2/1.3 electron microscope grid and plunge-frozen into liquid ethane using a Vitrobot Mark IV (FEI). Data were collected on a Titan Krios (FEI) microscope equipped with a Gatan Quantum LS/K2 Summit direct electron detection camera (operated with 300-kV acceleration voltage and slit width of 20 eV). Counting mode movies were collected on a Gatan K2 Summit direct electron detector with a nominal physical pixel size of 0.843 Å per pixel with a dose per frame 1.2 e-/Å^2. A total of 30 frames with a frame rate of 5 Hz were taken for each movie, resulting in a final dose of 36 e-/Å^2 per image. Automated data collection was driven by the SerialEM automation software package, with image shift induced-beam tilt correction (23).

Micrographs containing crystalline ice were used to estimate the anisotropic magnification distortion using mag_distortion_estimate (44). CTF estimation was performed using CTFFIND 4.1.8 on movie stacks with a grouping of three frames and correction for anisotropic magnification distortion (45). Unblur (46) was used to correct beam-induced motion with dose weighting and anisotropic magnification correction, resulting in a physical pixel size of 0.838 Å/pixel.

All particle picking was performed manually using EMAN2 e2helixboxer.py (47). All fibril particles were first extracted using 1,024-pixel box sizes and a 10% interbox distance and then subjected to two-dimensional (2D) class averaging. 2D class averages reveal that E46K α-syn forms fibrils of a single morphology with a pitch of ∼800 Å (*SI Appendix*, Fig. S2*B*). We next extracted all fibrils with a 686-pixel box size and 10% interbox distance and again performed 2D class averaging. 2D class averaging of 686 pixel boxes resulted in clear separation of beta-strands along the length of the fibril. 2D class averages and their corresponding simulated diffraction patterns together indicate that the helical rise is ∼4.8 Å with a C_n rotational symmetry due to the presence of a meridional reflection (*SI Appendix*, Fig. S2*B*). Due to the two-fold mirror symmetry present in the 2D class averages, we reasoned that the fibril had a C_2 rotational symmetry. Using a calculated helical twist of 178.92° (given pitch of 800 Å and rise of 4.8 Å) and C_2 rotational symmetry, we carried out three-dimensional (3D) class averaging with a single class and a featureless cylinder created by relion_helical_toolbox as an initial model (48). The featureless cylinder was refined to a reasonable model where separation of beta-sheets in the *x*–*y* plane of the fibril could be visualized. This model was then used to separate good and bad particles with a 3D class averaging job with three classes. Fibrils contributing to the best class in the previous 3D classification were reextracted with a 400-pixel box size and 10% interbox distance and phase flipped for subsequent classification and high resolution refinement. An additional 3D class averaging job was performed, and a final subset of 114,260 helical segments were selected for gold-standard auto-refinement in RELION. Refinement yielded a final 2.5-Å reconstruction (*SI Appendix*, Fig. S2*C*). We sharpened the map using phenix.auto_sharpen with a sharpening factor of −140 Å^2 and a resolution cutoff of 2.5 Å (49).

Atomic Model Building. We used phenix.map_to_model with an input sequence corresponding to E46K α-syn to build an initial model (49). Phenix.map_to_model correctly built a segment of the N terminus of the fibril core, and we manually built the rest of the structure into the density map in COOT (50). We generated a five-layer model to maintain local contacts between chains in the fibril during structure refinement. We performed automated structure refinement using phenix.real_space_refine (49). We employed hydrogen bond distance and angle restraints for backbone atoms participating in β-sheets and side chain hydrogen bonds during automated refinements. We performed comprehensive structure validation of all our final models in Phenix.

Energetic Calculation. The standard free energy of stabilization of a given amyloid chain is computed as the difference in atomic solvation energy of a pseudoextended, solvated chain and the folded chain in the center of five layers of the known structure of a protofilament (51). The atomic solvation parameters are those of Eisenberg et al. (52), with additional terms to describe the entropy change of side chains on folding, as calculated by Koehl and Delarue (53), scaled by the percentage of side chain surface area buried.

Data Availability Statement. All structural data have been deposited into the Worldwide Protein Data Bank (wwPDB) and Electron Microscopy Data Bank (EMDB) with the following accession codes: PDB 6UFR and EMDB EMD-20759.

ACKNOWLEDGMENTS. We thank H. Zhou for use of the Electron Imaging Center for Nanomachines (EICN) resources and P. Ge for assistance in cryo-EM data collection. We acknowledge the use of instruments at the EICN supported by NIH Grants 1S10RR23057 and 1S10OD018111, NSF Grant DBI-1338135, and the California NanoSystems Institute at the University of California, Los Angeles. The authors acknowledge NIH Grant AG 060149, NIH Grant AG 054022, NIH Grant AG061847, and Department of Energy Grant DE-FC02-02ER63421 for support. D.R.B. was supported by the National Science Foundation Graduate Research Fellowship Program.

1. M. G. Spillantini, R. A. Crowther, R. Jakes, M. Hasegawa, M. Goedert, alpha-Synuclein in filamentous inclusions of Lewy bodies from Parkinson's disease and dementia with lewy bodies. *Proc. Natl. Acad. Sci. U.S.A.* **95**, 6469–6473 (1998).
2. M. G. Spillantini *et al*., Filamentous α-synuclein inclusions link multiple system atrophy with Parkinson's disease and dementia with Lewy bodies. *Neurosci. Lett.* **251**, 205–208 (1998).
3. M. G. Spillantini, M. Goedert, Neurodegeneration and the ordered assembly of α-synuclein. *Cell Tissue Res.* **373**, 137–148 (2018).
4. A. B. Singleton *et al*., α-Synuclein locus triplication causes Parkinson's disease. *Science* **302**, 841 (2003).
5. M.-C. Chartier-Harlin *et al*., Alpha-synuclein locus duplication as a cause of familial Parkinson's disease. *Lancet* **364**, 1167–1169 (2004).
6. P. Ibáñez *et al*., Causal relation between alpha-synuclein gene duplication and familial Parkinson's disease. *Lancet* **364**, 1169–1171 (2004).
7. A. W. P. Fitzpatrick *et al*., Cryo-EM structures of tau filaments from Alzheimer's disease. *Nature* **547**, 185–190 (2017).
8. J. A. Rodriguez *et al*., Structure of the toxic core of α-synuclein from invisible crystals. *Nature* **525**, 486–490 (2015).
9. B. Li *et al*., Cryo-EM of full-length α-synuclein reveals fibril polymorphs with a common structural kernel. *Nat. Commun.* **9**, 3609 (2018).
10. B. Falcon *et al*., Structures of filaments from Pick's disease reveal a novel tau protein fold. *Nature* **561**, 137–140 (2018).
11. B. Falcon *et al*., Novel tau filament fold in chronic traumatic encephalopathy encloses hydrophobic molecules. *Nature* **568**, 420–423 (2019).
12. R. Tycko, Molecular structure of aggregated Amyloid-β: Insights from solid-state nuclear magnetic resonance. *Cold Spring Harb. Perspect. Med.* **6**, a024083 (2016).
13. C. Peng *et al*., Cellular milieu imparts distinct pathological α-synuclein strains in α-synucleinopathies. *Nature* **557**, 558–563 (2018).
14. J. J. Zarranz *et al*., The new mutation, E46K, of α-synuclein causes Parkinson and Lewy body dementia. *Ann. Neurol.* **55**, 164–173 (2004).
15. L. R. Lemkau *et al*., Site-specific perturbations of alpha-synuclein fibril structure by the Parkinson's disease associated mutations A53T and E46K. *PLoS One* **8**, e49750 (2013).
16. W. Choi *et al*., Mutation E46K increases phospholipid binding and assembly into filaments of human α-synuclein. *FEBS Lett.* **576**, 363–368 (2004).
17. N. Pandey, R. E. Schmidt, J. E. Galvin, The alpha-synuclein mutation E46K promotes aggregation in cultured cells. *Exp. Neurol.* **197**, 515–520 (2006).
18. I. Íñigo-Marco *et al*., E46K α-synuclein pathological mutation causes cell-autonomous toxicity without altering protein turnover or aggregation. *Proc. Natl. Acad. Sci. U.S.A.* **114**, E8274–E8283 (2017).
19. R. Guerrero-Ferreira *et al*., Cryo-EM structure of alpha-synuclein fibrils. *eLife* **7**, e36402 (2018).
20. Y. Li *et al*., Amyloid fibril structure of α-synuclein determined by cryo-electron microscopy. *Cell Res.* **28**, 897–903 (2018).
21. X. Ni, R. P. McGlinchey, J. Jiang, J. C. Lee, Structural insights into α-synuclein fibril polymorphism: Effects of Parkinson's disease-related C-terminal truncations. *J. Mol. Biol.* **431**, 3913–3919 (2019).
22. M. D. Tuttle *et al*., Solid-state NMR structure of a pathogenic fibril of full-length human α-synuclein. *Nat. Struct. Mol. Biol.* **23**, 409–415 (2016).
23. D. N. Mastronarde, E. M. Serial, A program for automated tilt series acquisition on Tecnai microscopes using prediction of specimen position. *Microsc. Microanal.* **9**, 1182–1183 (2003).
24. A. A. Kornyshev, S. Leikin, Electrostatic zipper motif for DNA aggregation. *Phys. Rev. Lett.* **82**, 4138–4141 (1999).
25. S. B. Prusiner *et al*., Evidence for α-synuclein prions causing multiple system atrophy in humans with parkinsonism. *Proc. Natl. Acad. Sci. U.S.A.* **112**, E5308–E5317 (2015).
26. M. D. Watson, J. C. Lee, N-terminal acetylation affects α-synuclein fibril polymorphism. *Biochemistry* **58**, 3630–3633 (2019).
27. M. Wakabayashi, K. Matsuzaki, Formation of amyloids by abeta-(1-42) on NGF-differentiated PC12 cells: Roles of gangliosides and cholesterol. *J. Mol. Biol.* **371**, 924–933 (2007).
28. K. Ono, M. M. Condron, D. B. Teplow, Structure-neurotoxicity relationships of amyloid β-protein oligomers. *Proc. Natl. Acad. Sci. U.S.A.* **106**, 14745–14750 (2009).

29. F. Hosp *et al*., Spatiotemporal proteomic profiling of Huntington's disease inclusions reveals widespread loss of protein function. *Cell Rep.* **21**, 2291–2303 (2017).
30. K. Zhao *et al*., Parkinson's disease associated mutation E46K of α-synuclein triggers the formation of a novel fibril structure. bioRxiv 870758, 10.1101/870758 (2019).
31. D. L. Caspar, C. Cohen, "Polymorphism of tropomyosin and a view of protein function" in *Nobel Symposium 11. Symmetry and Function of Biological Systems at the Macromolecular Level*, A. Engstrom, B. Strandberg, Eds. (Almquist and Wiksell; John Wiley and Sons, Inc., 1969), pp. 393–414.
32. R. Guerrero-Ferreira *et al*., Two new polymorphic structures of human full-length alpha-synuclein fibrils solved by cryo-electron microscopy. *eLife* 8, e48907 (2019).
33. J. N. Onuchic, P. G. Wolynes, Z. Luthey-Schulten, N. D. Socci, Toward an outline of the topography of a realistic protein-folding funnel. *Proc. Natl. Acad. Sci. U.S.A.* **92**, 3626–3630 (1995).
34. R. Riek, D. S. Eisenberg, The activities of amyloids from a structural perspective. *Nature* **539**, 227–235 (2016).
35. C. B. Anfinsen, Principles that govern the folding of protein chains. *Science* **181**, 223–230 (1973).
36. E. L. Guenther *et al*., Atomic structures of TDP-43 LCD segments and insights into reversible or pathogenic aggregation. *Nat. Struct. Mol. Biol.* **25**, 463–471 (2018).
37. R. A. Warmack *et al*., Structure of amyloid-β (20-34) with Alzheimer's-associated isomerization at Asp23 reveals a distinct protofilament interface. *Nat. Commun.* **10**, 3357 (2019).
38. Q. Cao, D. R. Boyer, M. R. Sawaya, P. Ge, D. S. Eisenberg, Cryo-EM structures of four polymorphic TDP-43 amyloid cores. *Nat. Struct. Mol. Biol.* **26**, 619–627 (2019).
39. D. R. Boyer *et al*., Structures of fibrils formed by α-synuclein hereditary disease mutant H50Q reveal new polymorphs. *Nat. Struct. Mol. Biol.* **26**, 1044–1052 (2019).
40. L. R. Lemkau *et al*., Mutant protein A30P α-synuclein adopts wild-type fibril structure, despite slower fibrillation kinetics. *J. Biol. Chem.* **287**, 11526–11532 (2012).
41. A. R. Hurshman Babbes, E. T. Powers, J. W. Kelly, Quantification of the thermodynamically linked quaternary and tertiary structural stabilities of transthyretin and its disease-associated variants: The relationship between stability and amyloidosis. *Biochemistry* **47**, 6969–6984 (2008).
42. H. A. Lashuel, C. R. Overk, A. Oueslati, E. Masliah, The many faces of α-synuclein: From structure and toxicity to therapeutic target. *Nat. Rev. Neurosci.* **14**, 38–48 (2013).
43. J. van Meerloo, G. J. L. Kaspers, J. Cloos, "Cell sensitivity assays: The MTT assay" in *Cancer Cell Culture: Methods and Protocols*, I. A. Cree, Ed. (Humana Press, 2011), pp. 237–245.
44. T. Grant, N. Grigorieff, Automatic estimation and correction of anisotropic magnification distortion in electron microscopes. *J. Struct. Biol.* **192**, 204–208 (2015).
45. A. Rohou, N. Grigorieff, CTFFIND4: Fast and accurate defocus estimation from electron micrographs. *J. Struct. Biol.* **192**, 216–221 (2015).
46. T. Grant, N. Grigorieff, Measuring the optimal exposure for single particle cryo-EM using a 2.6 Å reconstruction of rotavirus VP6. *eLife* **4**, e06980 (2015).
47. G. Tang *et al*., EMAN2: An extensible image processing suite for electron microscopy. *J. Struct. Biol.* **157**, 38–46 (2007).
48. S. He, S. H. W. Scheres, Helical reconstruction in RELION. *J. Struct. Biol.* **198**, 163–176 (2017).
49. P. V. Afonine *et al*., Real-space refinement in PHENIX for cryo-EM and crystallography. *Acta Crystallogr. D Struct. Biol.* **74**, 531–544 (2018).
50. P. Emsley, B. Lohkamp, W. G. Scott, K. Cowtan, Features and development of Coot. *Acta Crystallogr. D Biol. Crystallogr.* **66**, 486–501 (2010).
51. D. Eisenberg, A. D. McLachlan, Solvation energy in protein folding and binding. *Nature* **319**, 199–203 (1986).
52. D. S. Eisenberg, M. Wesson, M. Yamashita, Interpretation of protein folding and binding with atomic solvation parameters. *Chem. Scr.* **29A**, 217–222 (1989).
53. P. Koehl, M. Delarue, Application of a self-consistent mean field theory to predict protein side-chains conformation and estimate their conformational entropy. *J. Mol. Biol.* **239**, 249–275 (1994).

Supporting Information

Supplementary Figures:

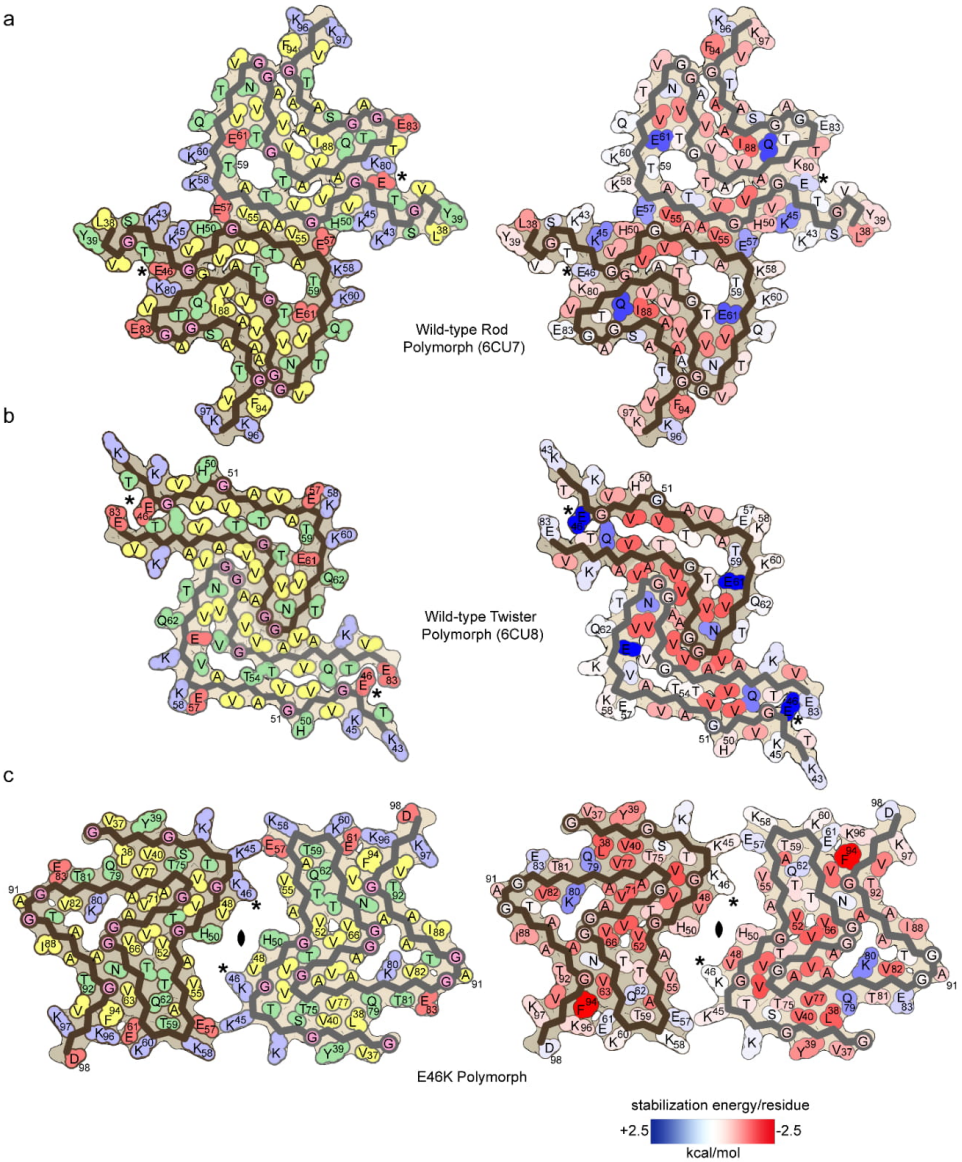

Supplementary Figure 1 Schematic representation and free energy of stabilization maps for the wild-type and E46K polymorphs

a-c) (left) Schematic representation of fibril structures with amino acid side chains colored as follows: hydrophobic (yellow), negatively charged (red), positively charged (blue), polar, uncharged (green), and glycine (pink). (right) Solvation energy maps of fibril structures. The stabilizing residues are red; the de-stabilizing residues are blue.

a

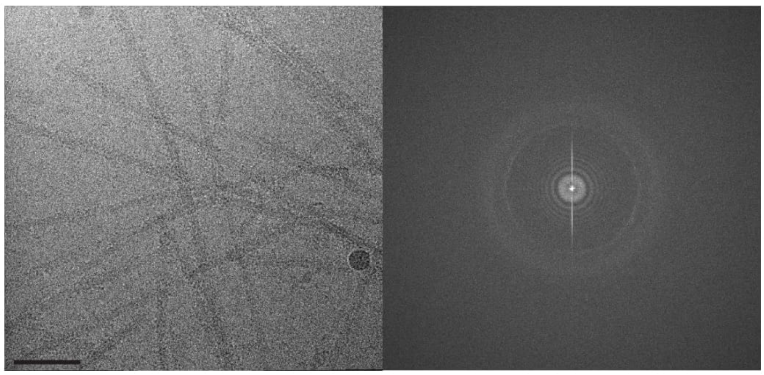

b

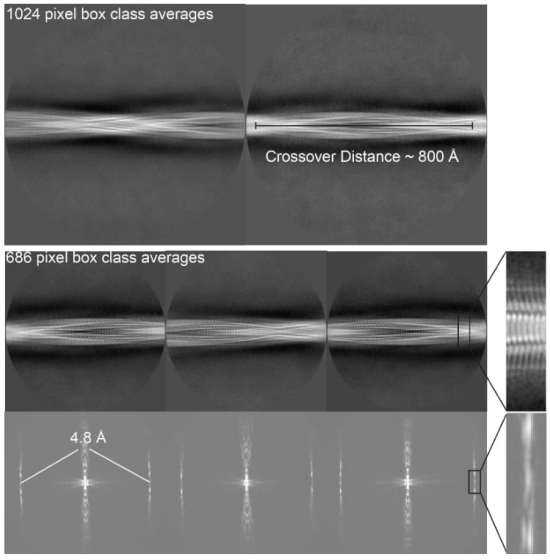
1024 pixel box class averages
Crossover Distance ~ 800 Å
686 pixel box class averages
4.8 Å

c

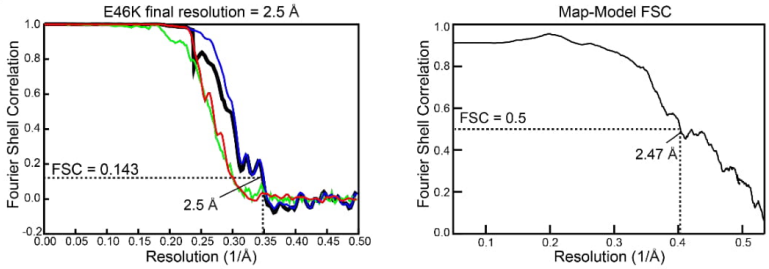
E46K final resolution = 2.5 Å
Fourier Shell Correlation
FSC = 0.143
2.5 Å
Resolution (1/Å)
Map-Model FSC
Fourier Shell Correlation
FSC = 0.5
2.47 Å
Resolution (1/Å)

3

Supplementary Figure 2 Cryo-EM Data Collection and Processing

a) Representative cryo-EM image and power spectrum. Scale bar 50 nm. b) 1024 pixel box class averages reveal a helical pitch of ~800 Å. 686 pixel box class averages and corresponding simulated diffraction patterns reveal a rise of ~4.8 Å and a C_2 rotational symmetry. c) Gold-standard half-map-half-map FSC and map-to-model FSC.

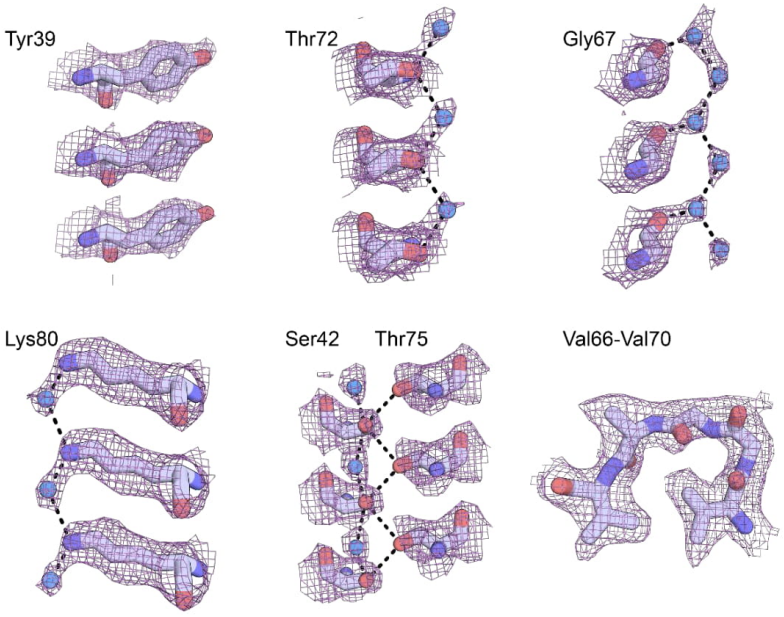

Supplementary Figure 3 Atomic model and density map highlight resolution of reconstruction and hydrogen bonding networks.

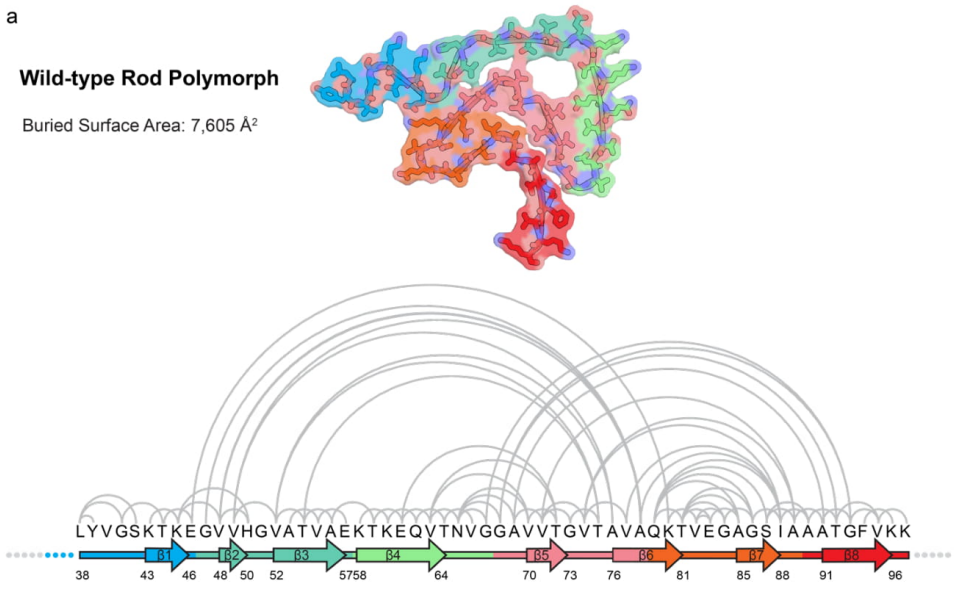
a
Wild-type Rod Polymorph
Buried Surface Area: 7,605 Å²
LYVGSKTKEGVVHGVATVAEKTKEQVTNVGGAVVTGVTAVAQKTVEGAGSIAAATGFVKK
β1
β2
β3
β4
β5
β6
β7
β8
38
43
46
48
50
52
57
58
64
70
73
76
81
85
88
91
96

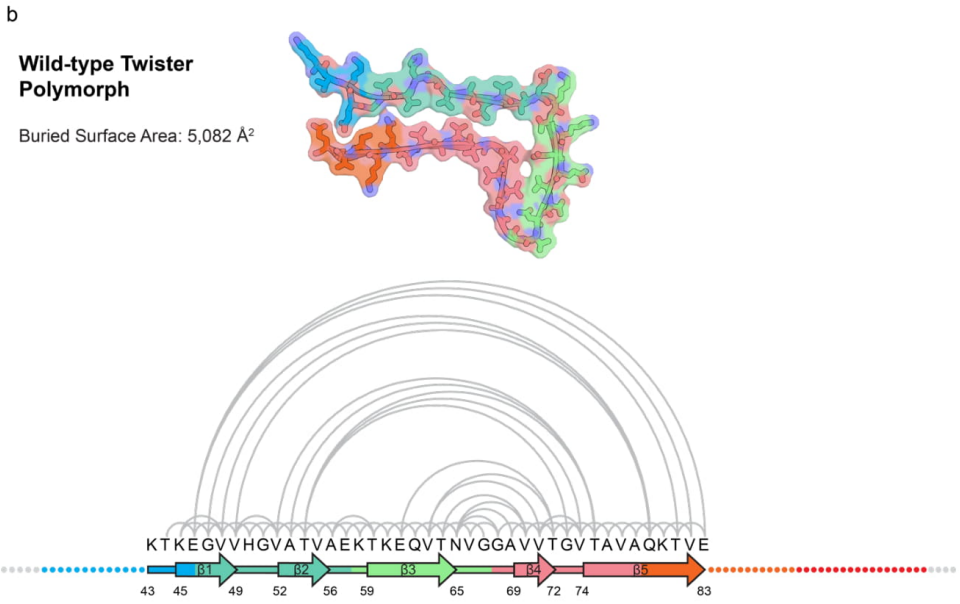
b
Wild-type Twister Polymorph
Buried Surface Area: 5,082 Å²
KTKEGVVHGVATVAEKTKEQVTNVGGAVVTGVTAVAQKTVE
β1
β2
β3
β4
β5
43
45
49
52
56
59
65
69
72
74
83

5

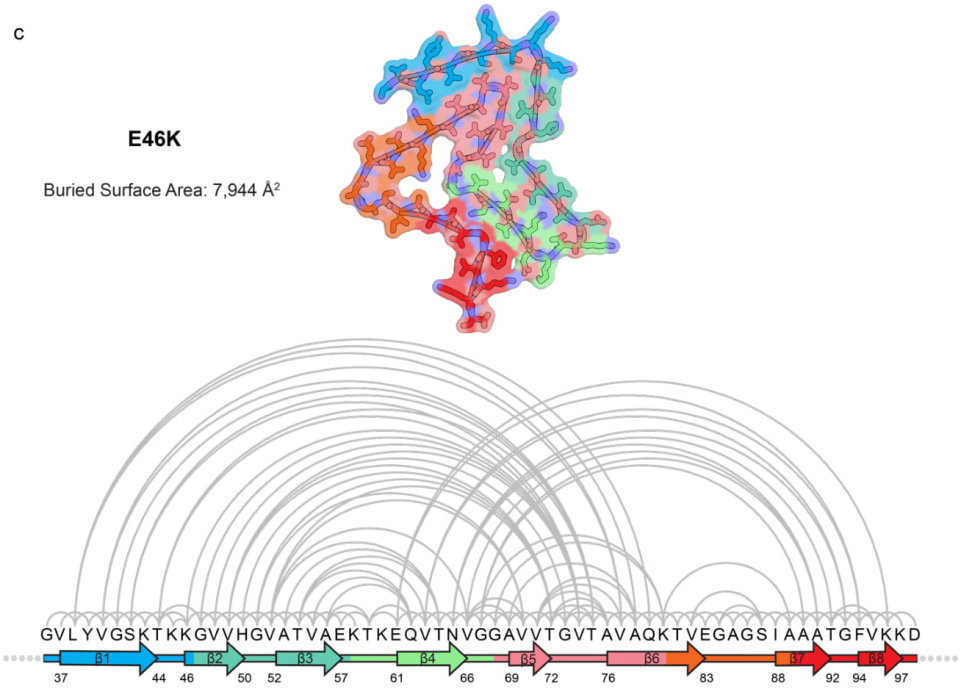

Supplementary Figure 4 Pairwise interaction analysis of wild-type and E46K protofilament folds

a-c) Protofilament fold and calculated buried surface area (top) and fibril core primary and secondary structure with pairs of interacting residues connected by half-circles (bottom) for a) wild-type rod, b) wild-type twister, and c) E46K polymorphs. E46K polymorph has a different set of interacting residues highlighting the difference in protofilament fold compared to wild-type. The E46K polymorph also has a larger number of interactions, which is reflected in its higher buried surface area.

6

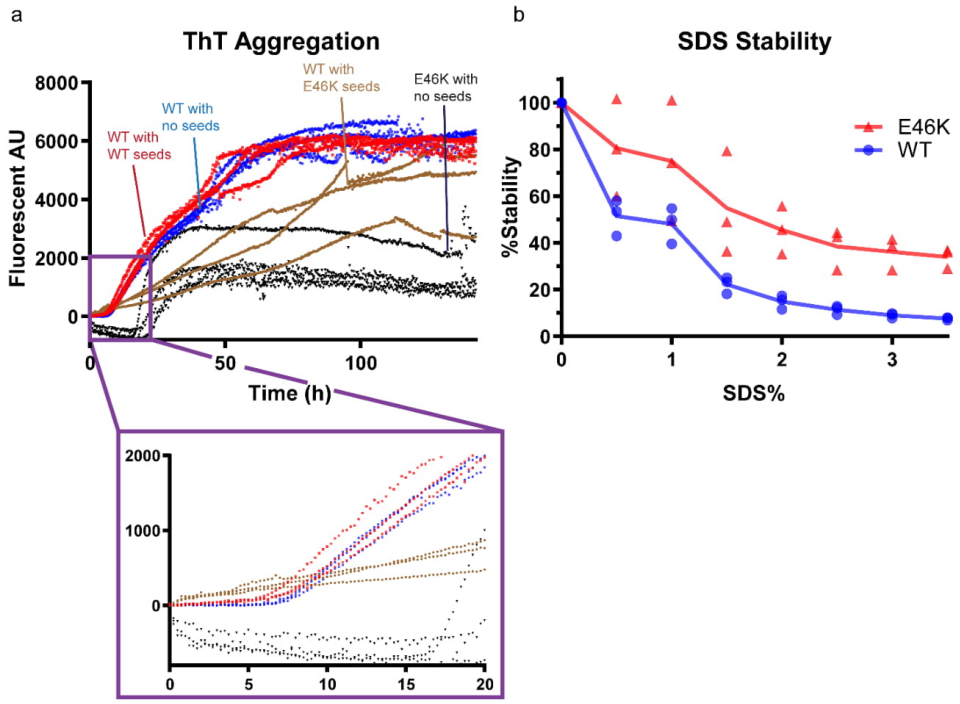

Supplementary Figure 5 Cross-seeding of wild-type α-syn by E46K fibrils and SDS fibril stability assay

a) Seeding of wild-type α-syn by wild-type fibrils results in a modestly reduced lag-time while seeding by E46K fibrils eliminates the lag phase. In addition, both unseeded and self-seeded wild-type α-syn have similar ThT binding ability shown by their similar ThT aggregation curves; on the other hand, wild-type α-syn seeded by E46K fibrils has a different ThT fluorescence intensity, indicating a different underlying structure. Unseeded wild-type α-syn has a shorter lag phase and higher max ThT signal than E46K α-syn. Breaks in the ThT curves originate from the microplate-reader being interrupted and re-started to allow other experiments to be performed in separate wells in the same microplate. Due to normalizing the initial reading to zero, the E46K

lag phase dips below zero fluorescence AU. The reason for this slight dip after the initial ThT reading is unknown; however, the classical nucleation-elongation sigmoidal growth curve is still demonstrated for E46K α-syn. b) E46K and wild-type fibrils were heated to 37 ˚C and incubated with varying concentrations of SDS. E46K fibrils are more resistant to SDS than wild-type fibrils. Individual triplicate measurements are shown and the plotted line represents the average of the triplicates.

CHAPTER 5

Structural exploration of α-synuclein fibril from Parkinson's disease

Brain seeded αSyn fibrils

Dr. Virginia Lee's lab at University of Pennsylvania kindly provided the brain extracted seeded aSyn fibrils. Resembling to previously characterized recombinant αSyn fibrils using EM, the brain seeded fibrils showed similar 5nm and 10 nm width (Fig. 1a). However, non-twisting ribbon appeared to be the major fibril polymorph, unlike the recombinant wildtype αSyn fibrils, where twisting fibrils (twister and rod) consisted of major species. To further elucidate the structural details of the brain seeded fibrils, 180,000 fibril particles extracted from 7000 cryo-EM micrographs yielded major 2D classes (Fig. 1b). In fact, none of the discernible 2D class showed any twist. This further confirmed the non-twisting nature of the major species with symmetry units aligned along the perfect two-one screw axis. Although the ribbon polymorph is not uncommon in the recombinant fibrils, it was significantly enriched in the brain seeded fibrils.

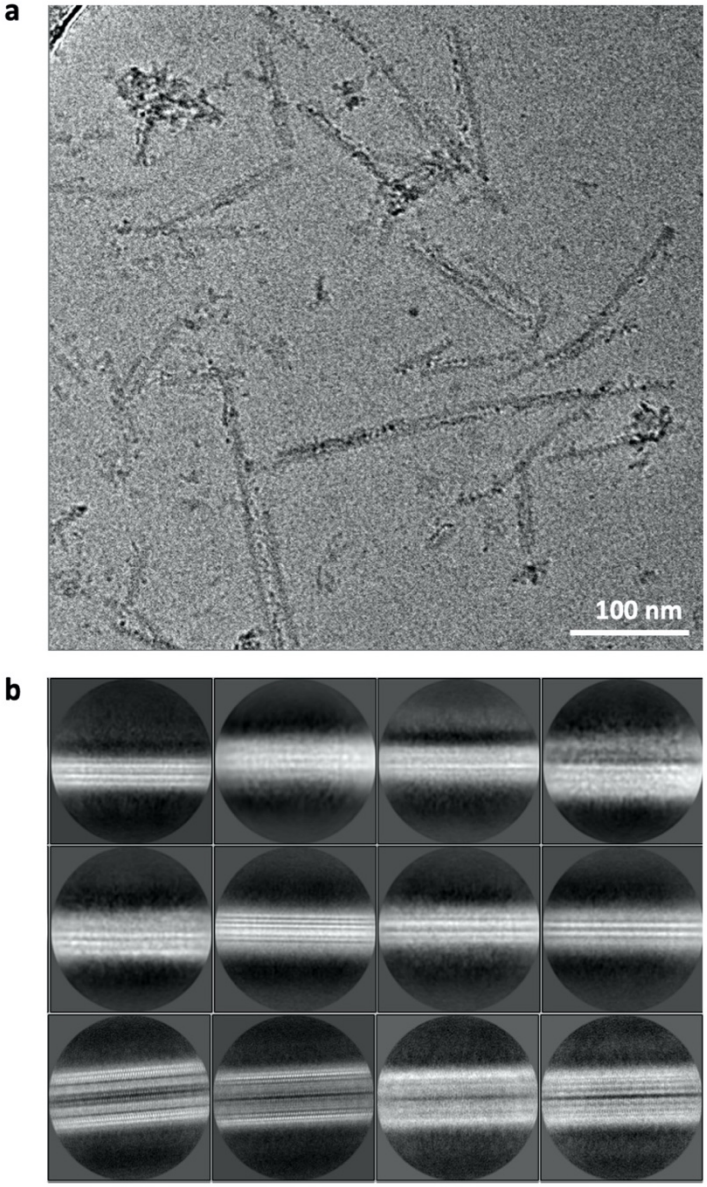

Fig. 5.1 Cryo-EM images **(a)** of and 2D classifications **(b)** of αSyn fibrils seeded by patient extracted aggregates.

One might argue that the difference in fibril growing condition may contribute to the contrasting fibril polymorphs (wildtype fibrils: 15 mM tetrabutyl-phosphonium bromide; brain seeded fibrils: 50 mM Tris-HCl pH 7.4, 750 mM NaCl, 10 mM NaF, 5 mM EDTA). Although no αSyn fibril structure determination was conducted using the exact same buffer condition, some experiments may provide some hints. Y. Li. et al.,'s fibril structure was solved in 50mM Tris-HCl 150mM KCl, with the structure almost identical to our rod polymorph. Another cryo-EM structure from Guerrero-Ferreira et al., also revealed a rod polymorph using high-salt (2.66 mM KCl, 1.47 mM KH2PO4, 137.93 mM NaCl, 8.06 mM Na2HPO4). Therefore, neither the Tris buffer nor high salt condition would contribute to the all ribbon polymorphs found in the brain seeded fibrils.

Brain extracted αSyn fibrils

Pathological αSyn fibrils were extracted from the brain tissue of PD patients provided by Virginia Lee Lab at UPenn and CNDR brain bank. In order to improve the fibril quality, rounds of optimizations in each step were performed to reach the highest possible extraction turnover (Fig. 2). Handling brain extracted fibrils were tricky comparing recombinant fibrils. The brain extracted fibrils were unstable. High pulse of probe sonication was essential to break the inclusion aggregates in

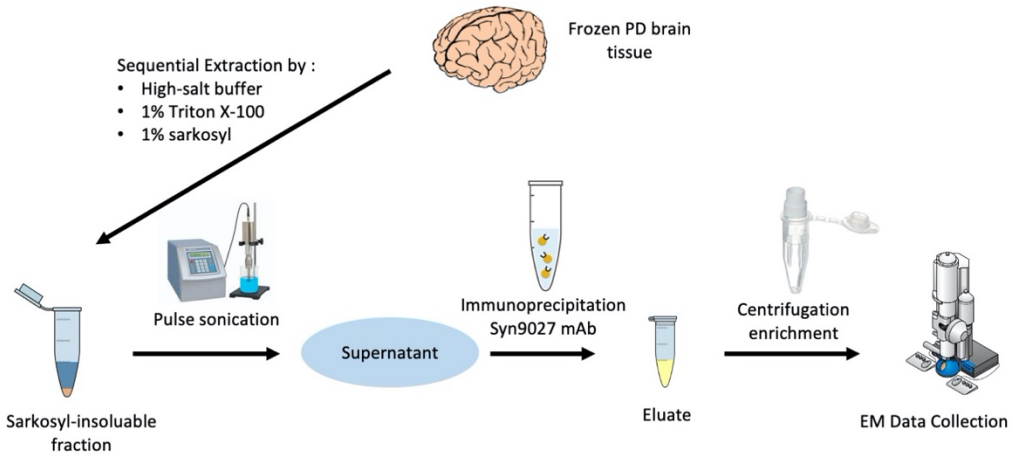

Fig. 5.2 Protocol of αSyn fibril extraction from PD brain

order to release fibrils, but long duration of sonication could break the fibrils into unworkable smaller pieces. Proteinase K treatment was less controllable and cannot replace the sonication. Unlike the recombinant fibrils, the brain extracted fibrils could disintegrate at room temperature, so the sample was always kept on ice and stored in freezer.

Brain extracted fibrils are 10 nm wide and 80 nm long on average (Fig. 3ab). The 2D classification resulted in non-twisting ribbon polymorphs (Fig. 3c), which is comparable with the brain seeded fibrils (Fig. 1b). On the 2D classes with structural details, the aSyn repeats relate by a perfect 2_1 screw symmetry with a typical 2.4 Å rise of amyloid fibril.

Preferred Orientation Problem

All the previous aSyn structures determined by cryo-EM have helical pitch ranging from ~400 Å to ~900 Å, which is relative to the box size of the 2D classification. This helicity provides sufficient information of protein unit in every orientation, necessary to guide the 3D reconstruction. Lack of helicity poses a challenge for structural reconstruction of amyloid fibril. To circumvent the inherent problem, we collected another

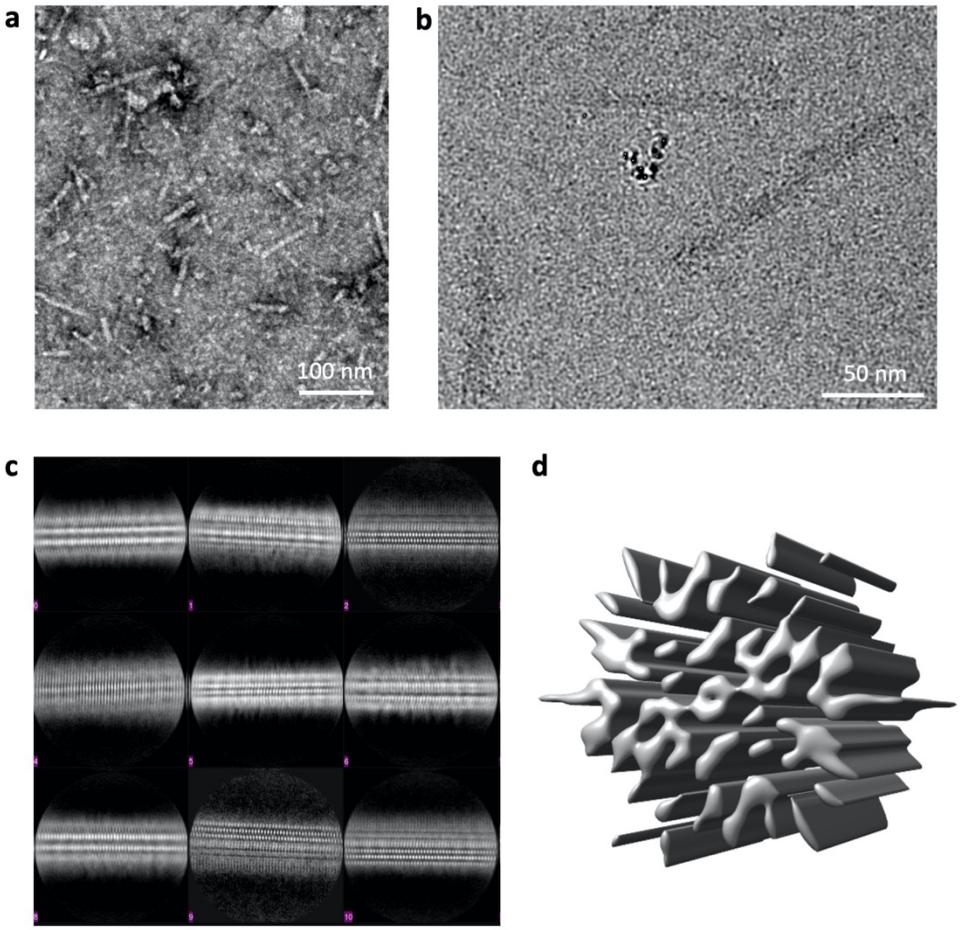

Fig. 5.3 Cryo-EM data of αSyn fibrils extracted from PD patients. Negative-stained **(a)** and cryo-EM **(b)** images**. (c)** 2D classification of non-twisting ribbon polymorph. **(d)** Preferred-orientation problem of the ribbon polymorph hinders a reasonable reconstruction.

cryo-EM dataset with a 40° tilt. The idea is to combine the tilt dataset with the untilt dataset in reconstruction, hoping to gain more information with the angle. However, this attempt was not able to produce a reasonable 3D map (Fig 4d).

Due to the limitation of current cryo-EM methodology, solving the structure of amyloid fibril with non-twisting ribbon polymorph remains challenging. Here to suggest a few possible solutions that can be explored in the future. Seuring et al., demonstrated the presence of salt may induce the flat ribbon species while absence of salt would produce twisted fibrils. Despite of different morphologies, the monomer structure remains the same in both conditions[1]. If the extracted fibrils could be turned into a twisting polymorph with the same protofilament structure, it would solve the problem. However, the buffer condition was tested during *in vitro* fibril growth, which may or may not apply to the extraction of preexisted brain fibrils. Another possibility is to process current dataset with the guidance of cryo-electron tomography (cryo-ET). The advancement in cryo-ET has pushed the resolution to 12 Å in biological application[2]. Obtaining a fibril structure in similar range would serve as an initial model to guide the 3D reconstruction of the cryo-EM data, possibly revealing the high-resolution structure of non-twisting ribbon.

1. Seuring, C. *et al.* Amyloid Fibril Polymorphism: Almost Identical on the Atomic Level, Mesoscopically Very Different. *J. Phys. Chem. B* (2017). doi:10.1021/acs.jpcb.6b10624
2. Guo, Q. *et al.* In Situ Structure of Neuronal C9orf72 Poly-GA Aggregates Reveals Proteasome Recruitment. *Cell* (2018). doi:10.1016/j.cell.2017.12.030